UNIVERSITY OF SYDNEY

SCHOOL OF AEROSPACE, MECHANICAL AND MECHATRONIC ENGINEERING

A THESIS SUBMITTED IN PARTIAL FULFILMENT OF THE REQUIREMENTS FOR THE DEGREE OF BACHELOR OF ENGINEERING IN MECHANICAL ENGINEERING (HONOURS)

Using high speed control to mitigate instabilities in effervescent atomiser nozzles

Author:
Aryonn RAWOL

Supervisor:
AGISILAOS KOURMATZIS

20th June, 2024

Abstract

Effervescent atomisers, known for their energy efficiency and superior spray quality, face significant challenges due to inherent instabilities caused by complex two-phase dynamics within the nozzle. This thesis explores the implementation of high-speed control to mitigate these instabilities, focusing specifically on the effects of pulsation in the gas and liquid inlet lines. The literature review covers the fundamentals of atomisation, mechanisms of instability, and the principles of effervescent atomisation. The research investigates how varying pulsation rates influence flow stability within the atomiser. Experimental findings demonstrate that lower pulsing rates increase flow instability by producing larger, irregular gas slugs, whereas higher pulsing rates enhance stability. These results align with theoretical insights, suggesting that a more homogenized gas-liquid mixture leads to reduced instability. The practical implications of this research extend to projects like the Reef Restoration and Adaptation Program's Marine Cloud Brightening initiative, highlighting the broader environmental significance of improving effervescent atomiser performance.

Statement of contribution

I hereby declare that the work within this thesis is solely my own, and the figures, tables, and statements throughout this report are my own, unless otherwise indicated by the references. I would like to express my profound gratitude to my supervisor, Agisilaos Kourmatzis, whose expert guidance, insightful feedback, and unwavering support were instrumental throughout the research and writing process. His extensive knowledge and experience in the field provided a solid foundation for this work.

Additionally, I extend my sincere thanks to Joel Harper-Harris for his invaluable assistance in setting up and running the experiments. Joel's technical expertise and practical insights were crucial in overcoming the numerous challenges encountered during the experimental phase of this project. His contributions were essential to the successful execution and analysis of the experiments.

This research would not have been possible without the collective efforts and support of my mentors and collaborators. Their contributions have significantly enriched the quality and depth of this thesis.

Aryonn Rawol	12 June 2024
Student	Date

Contents

1 Introduction **1**

2 Literature Review **2**

2.1 Atomisation Overview 2

2.1.1 Primary Atomisation 2

2.1.2 Secondary Atomisation 7

2.2 Atomisation Mechanisms 10

2.3 Effervescent Atomisation Overview 12

2.4 Flow Regimes within Effervescent Atomisers 13

2.5 Spray characteristics of Effervescent Atomisers 15

2.6 Unsteadiness in Effervescent Atomisation 16

2.6.1 Instability Mechanisms 16

2.7 Gas-liquid Mixing 20

2.8 Optical Diagnostics and Measurements of Sprays 22

2.8.1 Particle Imaging Velocimetry 24

2.8.2 Phase Doppler Anemometry 25

2.9 Image Processing 28

2.9.1 Proper Orthogonal Decomposition 31

2.10 High Speed Control (Feedback Control) 32

2.10.1 PID Control 32

2.11 Pulsed Atomisation 34

2.12 Motivation 35

3 Experimental Setup **36**

3.1 Method 36

3.2 Preliminary solenoid testing 37

3.3 Finalised solenoid setup 39

4 Data Processing and Results **41**

4.1 Preliminary image processing 41

4.2 High speed imaging 44

4.3 Binarisation 46

4.3.1 MATLAB Implementation 46

4.3.2 Optimisation 48

4.4 Proper orthogonal decomposition 49

4.4.1 MATLAB Implementation 50

4.5 Image processing flow 51

4.6 Results and analysis 52

4.6.1 Spatial variation within the nozzle 52

4.6.2 Effect of GLR on stability within the nozzle 56

4.6.3 Effect of pulsing on stability within the nozzle 59

4.7 Future work 63

4.7.1 Reproducibility of results 63

4.7.2 Improvements to the experimental method 64

5 Conclusion **66**

A Rayleigh Instability Derivation **71**

List of Figures

2.1 Illustration of jet breakup regimes. Adapted from [2]. 3

2.2 Growth rate of a jet disturbance as a function of diameter 4

2.3 Comparison of (a) Theoretical jet breakup vs (b) Experimentally confirmed jet breakup from high speed photographs. Adapted from [6]. 5

2.4 Atomisation modes in liquid jets. a) and b) are bulk modes, c) is a surface mode, and d) is a mixed mode. Adapted from [2]. 10

2.5 Schematic of a typical effervescent atomiser. Adapted from [15]. 12

2.6 Flow regimes within an effervescent atomiser. Adapted from [15]. 13

2.7 Flow regimes for air-water mixtures in horizontal flow. Adapted from [17]. 13

2.8 Breakup modes for effervescent nozzles. Adapted from [18]. 14

2.9 Range of operation for different break-up mechanisms. Adapted using data from [22]. 14

2.10 Effect of GLR and injection pressure on SMD of spray. Adapted from [15]. 15

2.11 Spray cone angle of an atomised spray. Adapted from [21]. 16

2.12 Unsteadiness in two phase mixture at nozzle exit. Adapted from [25]. 16

2.13 Gas void fraction as a function of time under various flow regimes. Adapted from [21]. 17

2.14 Average and fluctuation characteristics vs Bubble Number Density. Adapted from [21]. 18

2.15 Slug passage frequency vs speed of sound in flow. Adapted from [27]. 19

2.16 Effect of GLR on the Stokes Number. Adapted from [33]. 20

2.17 Regions of a spray. Adapted from [36]. 22

2.18 Examples of shadowgraphy and schlieren techniques. Adapted from [41]. 23

2.19 Experimental arrangement for PIV measurements. Adapted from [43]. 24

2.20 1 dimensional Phase Doppler setup. Adapted from [46]. 25

2.21 Comparison of beam intensity profiles. Adapted from [46]. 26

2.22 High speed image of shrimp producing cavitation bubble. Adapted from [48]. 28

2.23 Effect of binarisation threshold on 12bit grayscale image 29

2.24 Effect of pulsation frequency on spray structure. Adapted from [57]. 34

2.25 Effect of pulsation frequency on spray characteristics as a function of radial distance. Adapted from [57]. 34

3.1 Experimental Setup 36
3.2 Solenoid setup circuit diagram 37
3.3 Experimental Setup 38
3.4 Schematic of finalised experimental setup 39
3.5 Finalised experimental setup 40

4.1 Sample of internal flow within nozzle 41
4.2 Intensity plot 42
4.3 Single sided spectrum 42
4.4 Second processing method 43
4.5 Single sided spectrum - method 2 43
4.6 Regions of interest - testing round 1 44
4.7 Single sided spectra - testing round 1 44
4.8 Regions of interest - testing round 1 reanalysis 45
4.9 Single sided spectra - testing round 2 45
4.10 Binarisation spectra example 49
4.11 POD spectra example 49
4.12 Image processing flow 51
4.13 Selected regions of interest 52
4.14 Spatial variation of instabilities - GLR = 0.06 53
4.15 Spatial variation of instabilities - GLR = 0.10 54
4.16 Spatial variation of instabilities - GLR = 0.40 54
4.17 Effect of GLR on stability 56
4.18 Effect of GLR on spectral energy 57
4.19 GLR = 0.10 , Long chamber 59
4.20 Pulsing rate vs banded spectral energy 59
4.21 GLR = 0.40 , Air water junction 60
4.22 Pulsing rate vs banded spectral energy 61
4.23 GLR = 0.10 , Long chamber 61
4.24 Pulsing rate vs banded spectral energy 62
4.25 GLR = 0.10 , Pulsing rate = 10Hz 63
4.26 GLR = 0.40 , Pulsing rate = 20Hz 63

A.1 Stable vs perturbed state for a liquid jet 71

Nomenclature

ε	Infinitesimal perturbation
γ	Coefficient of surface tension
λ	Wavelength
μ	Dynamic viscosity
ω	Temporal growth rate
Φ	Phase difference
ϕ	Scattering angle
Φ_g	Gas volume fraction
Ψ	Elevation angle
ρ	Density
ρ_b	Bubble number density
σ	Surface tension
τ	Friction pressure
Θ	Beam intersection angle
$\tilde{p}$	Instantaneous pressure
ξ	$\exp^{\omega t+ikz}$: Oscillating component of a function
ζ	Ratio of binarisation threshold to maximum pixel intensity
a_E	Effective wave velocity
C_D	Coefficient of drag
D	Droplet diameter
d_0	Jet diameter
f_s	Slug passage frequency

GLR	Gas to liquid mass flow ratio
k	Wavenumber
m	Refractive index
Oh	$\frac{\mu}{\sqrt{\rho\sigma D}}$: Ohnesorge Number
R	Viscosity Ratio
R_0	Jet radius
R_0	Unperturbed jet radius
St	Stokes number
U	Jet exit velocity
u_R	Radial velocity
u_Z	Axial velocity
We	$\frac{\rho v^2 D}{\sigma}$: Weber number
m_D	Critical droplet mass

Chapter 1

Introduction

Atomisers are crucial for transforming bulk liquids into finely dispersed sprays. Their applications range from medical substance delivery to agricultural spraying, energy production, and industrial processes. Despite their widespread use, the ongoing quest for optimizing atomisation processes while minimizing energy consumption remains a significant focus.

A notable innovation in atomisation technology is the effervescent atomiser, which offers improved energy efficiency and spray quality for a given set of operational conditions, as compared to other atomiser types. However, it faces a key challenge—the inherent instability in the sprays it generates, stemming from complex two-phase dynamics within the atomiser's nozzle. This thesis seeks to address this challenge through a practical approach: implementing high-speed control on the gas and liquid inlet lines of effervescent atomisers. Specifically, the focus is on the effects of pulsation in these inlet lines, aiming to enhance spray stability and contribute to advancements in atomisation technology.

The literature review highlights the critical factors influencing atomisation, including the gas-to-liquid mass flow ratio, injection pressure, and the nature of flow regimes. Previous studies have identified that large gas bubbles within the nozzle disrupt the homogeneity of the spray and lead to instability. This research builds on these findings by exploring how varying pulsation rates can mitigate these instabilities, thus improving the overall performance of effervescent atomisers.

The experimental work conducted in this thesis demonstrated that pulsation rates significantly affect flow stability within the atomiser. Lower pulsing rates led to larger, more irregularly distributed gas slugs, increasing flow instability. In contrast, higher pulsing rates resulted in enhanced flow stability. This aligns with theoretical insights from the literature, suggesting that a more homogenized gas-liquid mixture reduces instability.

Importantly, this research has real-world implications beyond academia, particularly in the Reef Restoration and Adaptation Program's (RRAP) Marine Cloud Brightening project. This initiative aims to engineer high albedo clouds above coral reefs to mitigate rising sea surface temperatures and preserve ecosystems. The effervescent atomiser, a cornerstone of this project, plays a crucial role in addressing pressing global environmental challenges.

Chapter 2

Literature Review

2.1 Atomisation Overview

Atomisation is the process of converting a bulk liquid into a fine spray, or other similarly small dispersion of particles. This process can occur through a variety of methods: by the kinetic energy present within the fluid, through contact with another high velocity gas or liquid, or through the use of a mechanical device (such as a rotating drum or a vibrating chamber), as described by [1]. The devices used to produce atomisation are generally known as atomising nozzles.

The atomising process within nozzles is broadly split into two main types of atomisation: primary and secondary atomisation. As the liquid exits a nozzle, it breaks up into small droplets due to perturbations in the liquid interface. This step is referred to as primary atomisation [1]. These drops tend to further disintegrate into smaller droplets due to various breakup modes, which is thus known as secondary atomisation.

2.1.1 Primary Atomisation

Atomisation mechanisms are generally classified according to the fluid geometry, being broadly broken into the jet, sheet, and film classes, along with prompt atomisation [2]. A quasi-static hanging drop case is also given here, as a basis for understanding some of the mechanisms.

Hanging Drop

The hanging drop case can be demonstrated by the dripping discharge of liquid from a faucet. The main forces in play here are gravity - pulling the drop down; and surface tension - keeping the drop connected. These can be equated to find critical drop mass for breakup - assuming it is ejected from a long, narrow tube with diameter d_o - as follows:

$$m_D = \frac{\pi d_o \sigma}{g} \tag{2.1.1.1}$$

Here, m_D is the mass of the ejected drop, and σ is the surface tension of the fluid. The size of a spherical drop with this mass can also be calculated as follows:

$$D = \left(\frac{6 d_o \sigma}{\rho_L g} \right)^{1/3} \tag{2.1.1.2}$$

Note here that the diameter of the drop scales by a cube root as the tube diameter is decreased. From this, it is clear that gravity is not sufficient for fine atomisation, and additional mechanisms must be utilised.

Liquid Jet

The simplest class to consider is the liquid jet class. A liquid jet is usually considered to have a circular cross-section, but ellipsoid or others can be considered, provided the setup has a single characteristic dimension (a 'diameter'). If the jet is deformed in such a way that multiple dimensions are required for even a rough estimate, a sheet should be considered instead.

Jets exiting into ambient atmosphere are classically separated into four main regimes: Rayleigh type breakup, first wind-induced/wind assisted Rayleigh breakup, second wind-induced/wind stress breakup, and prompt atomisation [2]. This is also referred in Ohnesorge's original thesis, shown below at Table 2.1. Breakup within a jet tends to occur due to surface waves changing the local geometry of the jet. The amplification of these surface waves into oscillations separates the liquid body into drops [1]. Some properties of interest for liquid jets are the intact length: a measure of the growth rate of the fastest growing disturbance, and the drop size: a measure of the frequency of the most unstable disturbance. Initial research by [3] suggests that both jet velocity and diameter are directly proportional to the intact length of the jet. A diagram of jet conditions under the various regimes is shown here, along with the corresponding relative intact length of the jet:

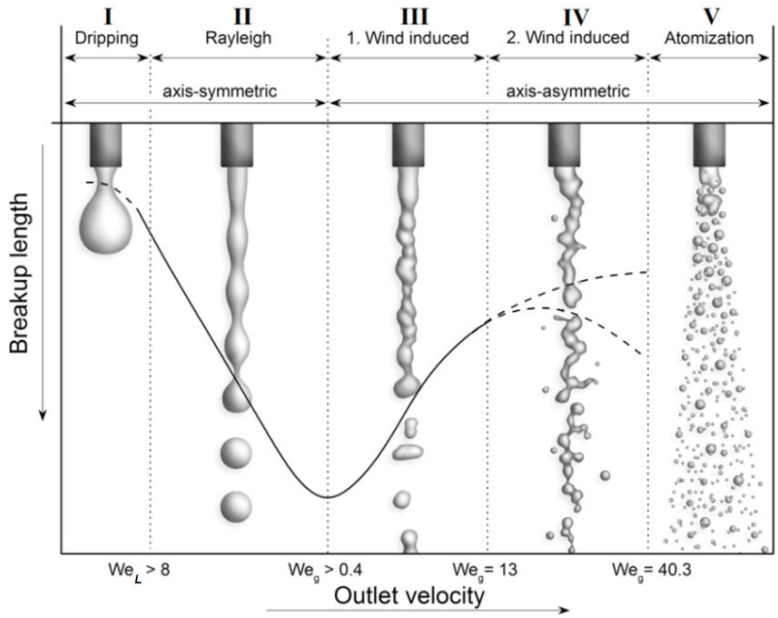

Figure 2.1: Illustration of jet breakup regimes. Adapted from [2].

Rayleigh breakup is the simplest case of jet breakup. Consider a low velocity liquid jet into a gaseous medium (a water jet in air). Ignoring viscosity and compressibility, the breakup of this jet will be dominated by small disturbances amplifying into necking regions. If the growth rate of any disturbance is dependent on the wavelength of that disturbance, then after some initial growth period, a small selection of disturbances will come to dominate the breakup, posited by [4]. Thus, finding the growth rate of the disturbance in relation to some intrinsic property of that disturbance is crucial. A full derivation of this process is shown in Appendix A.

Following the derivation gives an expression for the temporal growth rate (ω) without an explicit reliance on the oscillation (ξ) and the perturbation size (ε), as follows:

$$\omega^2 = \frac{\gamma}{\rho R_0^3}\frac{I_1(kR_0)}{I_0(kR_0)}\left(1-k^2R_0^2\right)(kR_0) \tag{2.1.1.3}$$

Here, R_0 is the jet radius, and k is the spatial growth rate. From this, it can be seen that ω is only real-valued (i.e. positive growth rate) when $kR_0 < 1$. Furthermore, the maximum value of this growth rate is obtained when $k_{opt}R_0 \approx 0.697$, as shown from this plot below:

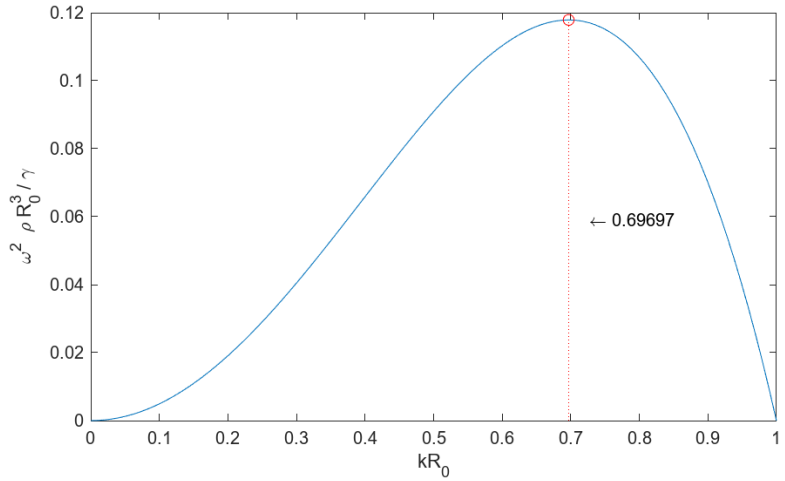

Figure 2.2: Growth rate of a jet disturbance as a function of diameter

Thus, most unstable wavelength can be calculated, as the wave number is related to the wavelength by the following expression:

$$k = \frac{2\pi}{\lambda} \implies \lambda_{opt} = \frac{2\pi}{0.697}R_0 = 9.014R_0 \tag{2.1.1.4}$$

Hence, the fastest growing wavelength is 9.01 times the radius of the jet [1]. After this breakup, the most common drop size will correspond to the column of jet with a height $9.01R_0$, giving the drop size as follows:

$$9.014R_0 \cdot \pi R_0^2 = \frac{4}{3}\pi r_D^3 \implies r_D = 1.89R_0 \tag{2.1.1.5}$$

Thus, the radius of the formed droplet will be more than 1.89 times that of the undisturbed jet. The effects of viscosity, as well as the relative co-flowing air velocity (parallel to the jet) - on the resultant droplet diameter - were examined by Weber in [5]. He found that viscosity had the effect of increasing the optimum wavelength (the fastest growing wavelength) according to the following relation:

$$\lambda_{opt} = 2\sqrt{2}\pi R_0\left(1+\frac{3\mu_L}{\sqrt{2\rho_L\sigma R_0}}\right)^{0.5} \tag{2.1.1.6}$$

This leads to a modified average droplet size relation, as shown here:

$$r_D = (0.75\lambda_{opt}R_0^2)^{1/3} \tag{2.1.1.7}$$

However, as shown by the comparison of idealised vs actual breakup of liquid jets below, actual jets do not break into evenly spaced and sized droplets, with the existence of satellite drops much more prevalent. Reitz showed in [6] that the existence of these satellite drops can be sufficiently predicted by including higher order terms in the stability analysis.

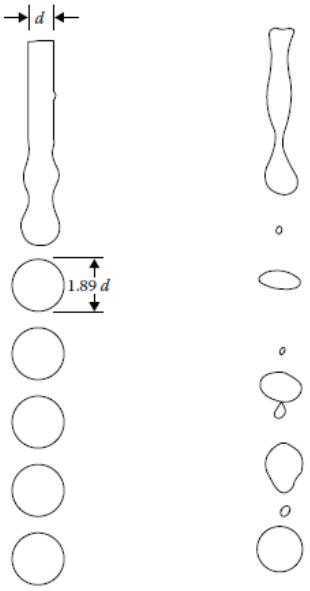

Figure 2.3: Comparison of (a) Theoretical jet breakup vs (b) Experimentally confirmed jet breakup from high speed photographs. Adapted from [6].

Weber also suggested that relative velocity has the effect of shortening the optimum wavelength, leading to smaller formed droplets. He studied the effect of air on droplet formation, leading to the second regime: first wind-induced breakup (wind assisted Rayleigh Breakup). Here, the aerodynamic forces present within the ambient atmosphere are no longer negligible. Instead, they promote the Rayleigh type waves formed, reducing the droplet size [1]. To quantify this relation, consider the dispersion equation given above in Eq 2.1.1.3. Weber expanded this relation to include stress due to aerodynamic effects, giving the following updated dispersion equation (note that this does not account for liquid viscosity):

$$\omega^2 + 3u_R k^2 \omega = k^2 R_0^2 \left(\frac{\sigma}{2\rho R_0^3}(1 - k^2 R_0^2) + \frac{\rho_A}{\rho_L} \frac{U^2}{2R_0} \frac{I_0(kR_0)}{I_1(kR_0)} \right) \tag{2.1.1.8}$$

Here, U is the velocity of jet at exit. Assuming discharge into ambient atmosphere, this is a suitable replacement for relative air velocity. Although the effect of this velocity on the maximum wave growth rate is not as easily visible, note that an increase in U leads to an increase in ω. This corresponds to higher velocities leading to faster wave growth, and thus shorter breakup lengths. In this regime, droplet diameters are still on the order of jet diameter, and breakup occurs many diameters downstream of nozzle [6].

Reitz introduces the separation of intact length L into the intact-surface length L_1 and intact-core length L_2 in [6] to help seperate breakup regimes. In Rayleigh type breakup, and first wind induced breakup, these two values coincide, as the entire jet breaks simultaneously. However, for second wind induced breakup, L_1 is shorter than L_2. Similarly, for prompt atomisation, L_1 goes to 0 in the limit, with the surface stripping immediately after nozzle exit.

As liquid velocity is further increased, Reitz in [6] suggests that Eq 2.1.1.8 shows progressively shorter optimum wavelengths (larger wavenumbers). In comparison to the Rayleigh breakup case, instabilities with $kR_0 > 1$ dominate the breakup. In this case, the surface tension force serves to oppose the breakup process, and the jet breakup is now dominated by short wavelength surface waves which are induced by instabilities at the jet surface. A simplified version of this relation for short wavelength surface waves ($kR_0 >> 1$) is given by [7], shown here:

$$\omega^2 = \frac{(\rho^2 k^2 U^2 - \sigma k^3)}{\rho_1} \tag{2.1.1.9}$$

This implies that surface waves are unstable when $k < \rho_A U^2/\sigma$. Furthermore, the maximum growth can be given by:

$$\omega_{opt} \approx 0.4 \frac{U^3}{\sigma} \sqrt{\frac{\rho_A^3}{\rho_L}} \tag{2.1.1.10}$$

Another important consideration, highlighted by these expressions above, is that at high velocities the dispersion relation - and thus the optimum wavelength - is independent of the jet radius. This suggests that jet curvature effects, and consequently surface tension, become negligible.

The atomisation regime is of most interest for this thesis, as this is the regime effervescent atomisers operate under. Here, surface stripping begins at nozzle exit, and the intact core length tends towards zero [6]. The shape of the spray is a cone, with the vertex internal to the nozzle. No single atomisation process is able to fit all the trends produced by experimental work, as described by Reitz. Instead, he proposes a combination of theories, namely: liquid turbulence within the nozzle and aerodynamic surface wave growth.

Liquid turbulence attributes atomisation to velocity profile relaxation in turbulent flows, leading to a larger spread from the jet when nozzle exit is reached. However, this would imply turbulent jets as the most unstable phenomenon, which is contrary to current experimental work [6]. The other theory suggests that atomisation is primarily a surface driven phenomenon, with the main atomisation process being contributed to the stripping of ligaments from the surface of the jet [8].

Assuming that $ka \rightarrow \infty$, as with the second wind induced regime, the spray angle can be predicted by combining the radial velocity (u_R) of the fastest unstable surface wave and the injection velocity

$$\tan(\theta/2) = \frac{u_R}{U} = \frac{2\pi\omega}{AkU} \tag{2.1.1.11}$$

Here, A is an experimentally derived proportionality constant. This equation suggests that spray angle increases with an increase in gas density, and decreases with an increase in liquid viscosity and injection velocity, which aligns with experimental work [8]. Reitz further suggests that as injection velocity is increased, this equation asymptotically depends only on the gas-liquid density ratio [6].

2.1.2 Secondary Atomisation

Secondary atomisation is the process of further breakup of a droplet of fluid which has already separated from the bulk flow. It is of notable importance here as secondary atomisation is one of the main mechanisms by which extremely fine droplets are produced, as shown by [9]. In flowing air, the stability of the droplet can be examined by considering the various pressures present on its surface, shown here:

$$p_I = p_A + p_\sigma \tag{2.1.2.1}$$

Here, p_I is the internal pressure at a point on the surface, and p_A and p_σ are the external aerodynamic pressure and the surface tension pressure respectively. From this, Lefebvre et al in [1] suggests that the droplet will remain stable as long as a change in aerodynamic pressure (p_A) can be balanced by a change in surface tension pressure (p_σ) - eg. by deforming - such that the internal pressure (p_I) remains constant. Instead, if p_A is large enough, the drop may deform enough to further reduce p_σ, which will lead to droplet disruption. The smaller drops formed will have a higher surface tension pressure, as shown by the relation here (for spherical droplets):

$$p_\sigma = \frac{4\sigma}{D} \tag{2.1.2.2}$$

Here, D is the diameter of the droplet. If the new droplet still does not have sufficient surface tension, it will undergo further breakup, with subdivision occurring until p_σ is sufficient to counteract the aerodynamic pressure. The shape of the droplet deformation is unlikely to be spherical in real testing, and depends on the airflow patterns after nozzle exit.

The breakup of a droplet in a flowing stream is an interplay of dynamic pressure, surface tension, and viscosity. As described in [3], at low viscosities, the deformation can be represented by the ratio of aerodynamic forces to surface tension forces. This produces the Weber number, defined as follows [10]:

$$We = \frac{\rho_A U_R^2 D}{\sigma} \tag{2.1.2.3}$$

Here, ρ_A is the density of ambient gas surrounding the droplet, and U_R is the relative air velocity. Consider further that the main aerodynamic force experienced here is drag, allowing for the formulation of an initial condition for breakup, when drag is equal to the surface tension force, as follows:

$$0.5 \cdot C_D \rho_A U_R^2 \frac{\pi}{4} D^2 = \pi D \sigma \tag{2.1.2.4}$$

This can be related via the coefficient of drag (C_D) to the Weber number formulation given above to calculate a 'critical' Weber number required for droplet breakup, shown by [1] here:

$$We_{crit} = \left(\frac{\rho_A U_R^2 D}{\sigma} \right)_{crit} = \frac{8}{C_D} \tag{2.1.2.5}$$

Similarly, for a given relative velocity U_R, the maximum stable drop size can be calculated as:

$$D_{max} = \frac{8\sigma}{C_D \rho_A U_R^2} \tag{2.1.2.6}$$

The droplet breakup mechanism also depends on the relative conditions of the gas stream it is released into. As Lefebvre et al. describes in [1], for a droplet exposed to ambient conditions - with a steady acceleration - the droplet flattens into a disc. This disc is then blown out into a bag shape, presenting concave to the direction of motion. This bag then disintegrates into fine droplets in the centre of the disk, with larger droplets forming from the rim.

Liquid viscosity also plays a role in droplet breakup, as demonstrated in Ohnesorge in [11]. As spray velocity is increased, Ohnesorge suggests that the relative effects of various forces on a droplet change, according to the table shown here, adapted from [11]:

Table 2.1: Relative effect of forces within a droplet as spray velocity is increased

Breakup Case	Inertial Forces	Gravitational Forces	Viscosity (Direct)	Viscosity (Indirect)
Case 1	$\rightarrow 0$	Significant	$\rightarrow 0$	0
Case 2	Moderate	Low	Low	$\rightarrow 0$
Case 3	Strong	~ 0	Significant	Moderate
Case 4	Very strong	$\rightarrow 0$	Strong	Very strong

Here, the indirect effect of viscosity is defined to be vortex shedding (described further in Section 2.2) by internal viscosity. Spray velocity is increased going down the table. The breakup cases in [11] are classified similarly to the mechanism for jet breakup described above by [1], as follows:

1. Slow dripping from nozzle - no jet formation
2. Breakup of jet through axisymmetric breakup - dilational wave breakup
3. Breakup of jet through screw symmetric breakup - sinusoidal wave breakup
4. Prompt atomisation of jet

As visible above, with an increase in spray velocity, inertial and viscous forces dominate over gravitational forces. The effect of viscosity is two-fold, as described by [12] and [13]. At low viscosity, the deformation of the droplet is impeded by the viscous forces, with an increase in mean drop diameter as viscosity increases. However, with an increase in viscosity past a critical value (which is dependent on the surrounding conditions of the nozzle, as well as spray velocity), viscosity acts to accentuate the effects of aerodynamic forces. The high viscosity impedes the deformation of the droplet to such an extent that a shattering phenomenon is observed [12], causing a reduction in mean droplet diameter with further increase in viscosity.

The breakup of a real droplet is not inviscid, and as such, the relative effects of viscosity to the aerodynamic forces is an important metric. The importance of this ratio can be expressed by considering the strengths of these forces. Consider the droplet as a vibrating body, assuming the first mode is dominant, and evaluate the pressures on the surface of the droplet. The surface tension force per unit area (surface tension pressure) can be described as:

$$P_\sigma = \frac{\sigma}{D} \tag{2.1.2.7}$$

Lefebvre et al. in [1] then describes the friction force per unit area (friction pressure) on the droplet surface as the product of the liquid viscosity and the velocity gradient within the droplet. Assuming that the droplet is vibrating at its natural frequency (ω), this can further be simplified as shown here:

$$\tau = \mu_L \frac{\partial U}{\partial x} \sim \mu_L \omega \tag{2.1.2.8}$$

The mass of the droplet can be expressed as follows:

$$M = \rho \frac{1}{6} \pi D^3 \tag{2.1.2.9}$$

To connect the friction expression to the surface tension pressure, consider the expression for the natural frequency of a droplet, from [14] as shown here:

$$\omega^2 = \frac{n(n-1)(n+2)\sigma}{3\pi M} = \frac{2n(n-1)(n+2)\sigma}{\rho_L \pi^2 D^3} \tag{2.1.2.10}$$

As the dominant mode of vibration is the first mode, when $n = 2$, this further simplifies as follows:

$$\omega^2 \approx \frac{16\sigma}{\rho_L \pi^2 D^3} \tag{2.1.2.11}$$

Now, substituting this into the friction pressure expression gives the following:

$$\tau \sim \mu_L \omega \approx \frac{4\mu_L}{\pi D} \sqrt{\frac{\sigma}{\rho_L D}} \tag{2.1.2.12}$$

Then, the expression for the ratio of friction force to surface tension force is thus:

$$\frac{\tau D}{\sigma} \approx \frac{4}{\pi} \frac{\mu_L}{\sqrt{\rho_L \sigma D}} \tag{2.1.2.13}$$

Ignoring the scaling parameters, the Ohnesorge number is therefore defined as:

$$Oh = \frac{\sqrt{We}}{Re} = \frac{\mu}{\sqrt{\rho \sigma D}} \tag{2.1.2.14}$$

The Ohnesorge number represents the relative effects of the internal viscosity force compared to the surface tension force within the droplet [11].

2.2 Atomisation Mechanisms

Atomisation mechanisms can be broadly split into two classes: bulk atomisation, and surface atomisation [2]. The bulk mode acts on the entirety of liquid core exiting the nozzle, as exemplified by the Rayleigh breakup type dripping, where the whole core separates into a droplet. In contrast, surface mode involves stripping of liquid from the surface of the jet, with part of the core staying intact. Repeating this stripping process on the same liquid core results in depletion of this core, and thus atomisation. The distinguishing feature between modes is the relative size of the disturbance compared to the size of the liquid jet. A visual example of this is given here:

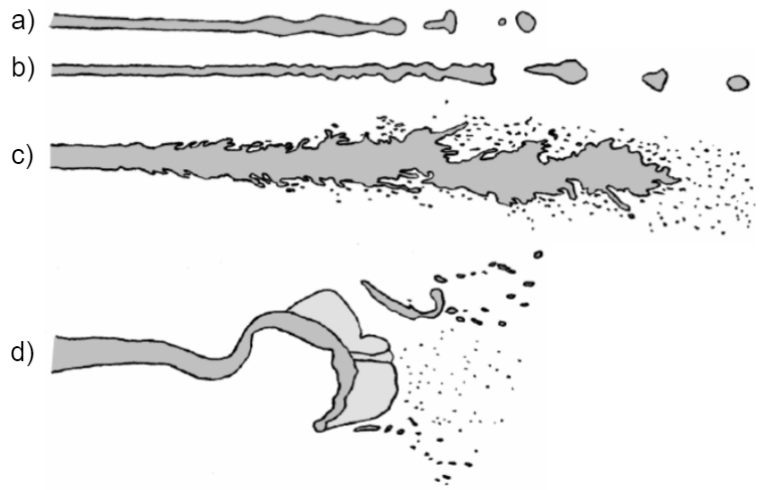

Figure 2.4: Atomisation modes in liquid jets. a) and b) are bulk modes, c) is a surface mode, and d) is a mixed mode. Adapted from [2].

Within these categories, the atomisation can further be broken into two processes, disturbance formation, and disturbance breakdown. The main disturbances formed within atomisation processes are waves, ligaments, bubbles and perforations [2]. Ligaments are liquid projections that protrude from the core, tending to be much longer than their width, while waves are much wider than their length. Waves can also be either part of the bulk mode, or stripping mode, depending on their relative size to the jet. Bubbles are pockets of gas within the liquid, and perforations are holes or breaks in the liquid.

The formation of disturbances can occur through a variety of mechanisms, and some of these will be explored here. The presence of liquid structures within the flow can lead to atomisation, through either the proliferation of recirculating zones/vortices, or the existence of turbulent eddies. Liquid turbulence is a common atomisation mechanism, causing disturbances by altering the surface of the bulk, leading to the formation of ligaments [2].

Hydrodynamic instabilities are the most common disturbance formation mechanism. Rayleigh-plataeu instability was explored above, but Kelvin-Heimholtz, and Tollmein-Schlicting instabilities are also common. They lead to the creation of surface waves, and may be driven by aerodynamic forces, surface tension, or turbulence. Existence of gas structures is also a factor in atomisation, either directly by stripping liquid from the surface, or indirectly, by affecting the instabilities present in the liquid [1]. However, as these are most relevant for low velocity flows, and in sheet and film flows, they will not be explored in detail.

The main atomisation mechanism within effervescent atomiser nozzles is bubble formation. These bubbles are introduced within the nozzle, leading to a two phase mixture being sprayed into the atmosphere. To understand how the presence of these bubbles leads to atomisation, it is worthwhile to explore some modes of disturbance breakdown.

The most obvious mechanism for breakdown is the growth of instabilities, for example the axisymmetric waves considered in Rayleigh-Plateau breakup. These instabilities cause breakdown when some part of the disturbance contacts itself or an interface. These are also partially responsible for secondary atomisation, through breakdown of ligaments [2].

Surface stripping, due to either lift or drag forces, is also a common breakdown mode. This separated section may be the tip of a wave or ligament, but can also be a large section of fluid from the downstream edge of an intact core. This would be classified under bulk fluid mode [2]. In all cases, the aerodynamic forces must overcome the viscous and surface tension forces extant in the bulk fluid. This force balance can be altered through wave formation, or the presence of hydrodynamic instabilities. Bag breakup, described above in the secondary atomisation section, is a breakdown mechanism under this category, characterised by the further entrainment of air into a separated ligament.

Bubble formation leads to atomisation within effervescent atomisers through the fragile shattering mechanism. Bubble rupture is the main method for fragile shattering within effervescent atomisers, and is driven by a change in pressure or interface interactions. In fragile shattering, the bulk fluid is unable to deform fast enough to react to the surrounding unsteady flow (i.e. the required rate of deformation exceeds the speed of liquid molecule relaxation) [2]. As a result, the fluid acts similarly to a solid, fragmenting rapidly. This shattering can be either bulk or surface based, with surface shattering leading to perforations. These form unstable ligaments which further break into smaller droplets.

2.3 Effervescent Atomisation Overview

Effervescent atomisers work on the principle of gas expansion. A schematic of the atomiser is shown in Figure 2.5. This image was adapted from [15].

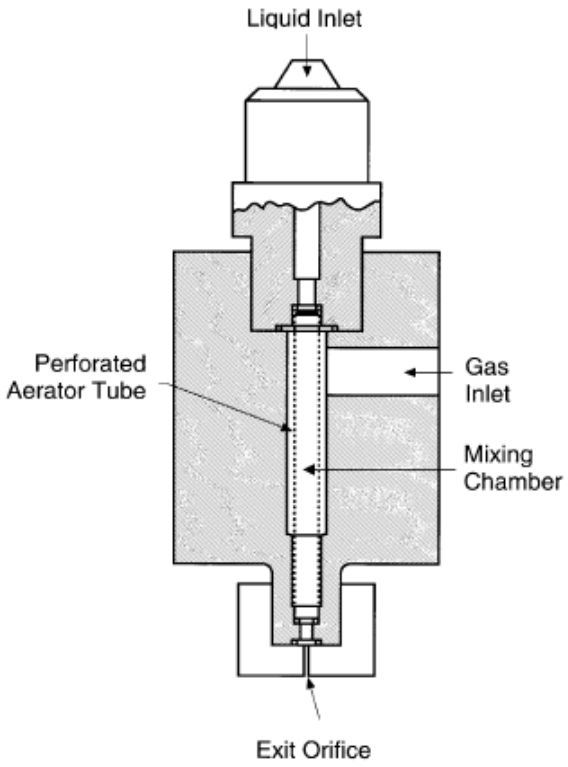

Figure 2.5: Schematic of a typical effervescent atomiser. Adapted from [15].

As seen above, the atomiser has a liquid and gas inlet. There are two main types of effervescent atomisers, outside-in gas injection - where the liquid is piped on the inside of the aerator tube, and inside-out gas injection - where instead the gas is piped through the inside of the aerator tube. However, these both work on the same principle. The gas is pumped at a higher pressure than the liquid, causing it to perfuse into the liquid stream, and create a two-phase flow. When this two phase flow exits the nozzle, it experiences a large pressure drop, causing the gas to expand rapidly, and shatter the liquid. This method provides significantly improved spray quality for a set of given operating conditions compared to other gas-assisted atomisers. Inside-out designs tend to be better suited for low liquid flow rates, and vice versa for for outside-in designs [15].

Effervescent atomisers require significantly lower injection pressures to provide the same quality of atomisation when compared to other types of atomisers, as mentioned by [1]. Lefebvre et al. in [16] also suggests that gas flow-rates are significantly smaller for effervescent atomisers when compared to other types of atomisers. These allow the atomiser to be used in more cost and space sensitive areas. Exit orifice diameters are much larger than those for other types of atomisers when evaluated at a comparable flow rate, described in [15], which reduces the chances of nozzle clogging, and allows for better manufacturability. The flow velocities encountered at the exit orifice of effervescent atomisers are lower than those within other types of atomisers due to the much lower wave speed of two phase flows. This is especially important here to reduce corrosion due to contact with seawater for this nozzle.

2.4 Flow Regimes within Effervescent Atomisers

Flow inside an effervescent atomiser tends to be of four main types. These are shown in Figure 2.6, as suggested by [15]. The flow regime is highly dependent on the ratio of gas to liquid flow rates (GLR).

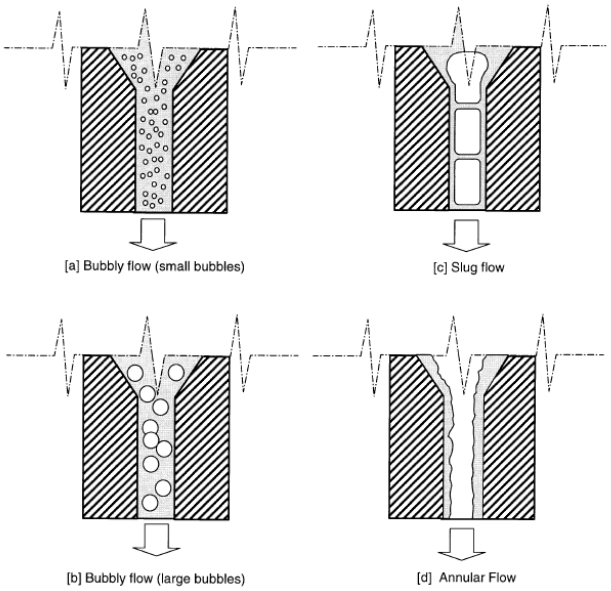

Figure 2.6: Flow regimes within an effervescent atomiser. Adapted from [15].

The exact conditions for specific flow regimes are difficult to quantify, as the internal flow depends on the internal geometry, the operating conditions, as well as the properties of the gas and liquid used. Here, the flow regimes are identified in terms of GLR, but specific transition points between the regimes are somewhat dependent on internal geometry and operating conditions. Shown below in Figure 2.7, adapted from [17], is a flow regime chart for two phase flow within a pipe, which can be used as a demonstration of the flow regimes.

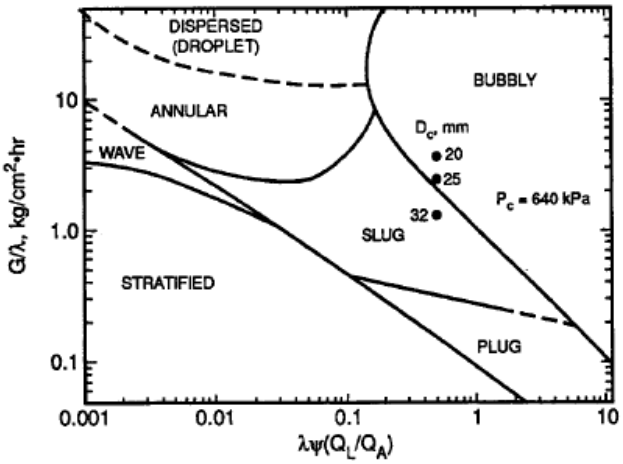

Figure 2.7: Flow regimes for air-water mixtures in horizontal flow. Adapted from [17].

Here, λ and ψ are both ratios in relation to water and air, and can thus be simplified to 1. G is the air mass flow flux, Q_L is the liquid volume flow rate, and Q_A is the air volume flow rate. Note that GLR can be related to the Q_L/Q_A ratio shown above via the following relation.

$$GLR = \frac{\dot{m}_A}{\dot{m}_L} = \frac{\rho_A}{\rho_L}\frac{Q_A}{Q_L} \tag{2.4.0.1}$$

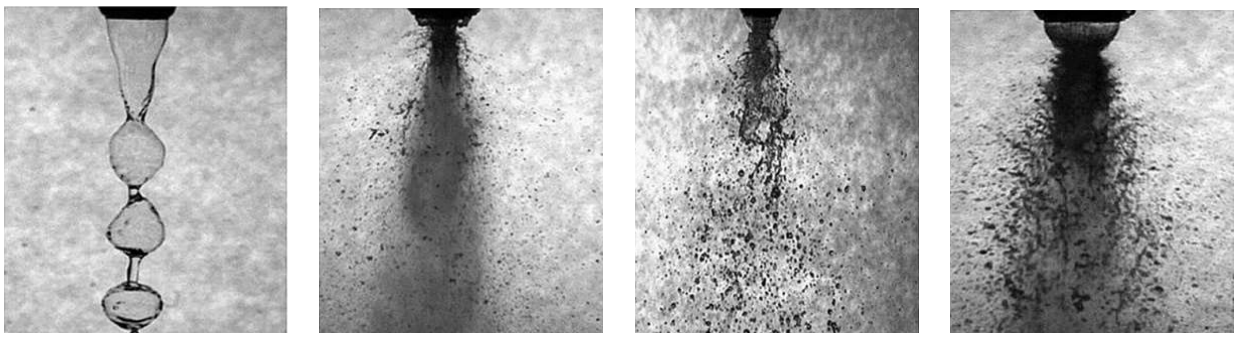

(a) Bubble type breakup (b) Ligament disintegration breakup (c) Annular sheet disintegration breakup (d) Tree mode breakup

Figure 2.8: Breakup modes for effervescent nozzles. Adapted from [18].

At the lowest GLR ranges, described as occurring at a GLR of up to 0.07 by [19] and [20], exhibit a bubbly flow. The bubble size decreases with an increase in GLR within this flow regime, as shown by [21]. The spray morphology in this regime is characterised by bubble explosions within the two phase flow ejected from the nozzle exit. Other processes, such as Kelvin-Heimholtz instability, also play a role in the secondary atomisation of the spray after dispersal. The low sonic velocity of two phase flows, as described by [22], also causes shock-waves which impart shear forces on the inter-phases, causing further breakup.

Annular flow, on the other hand, operates under a tree mode of breakup, which is highlighted in [23]. Annular flow occurs at relatively high GLR values of above 0.15, as described by [9]. The gas core of the annular flow regime squeezes the liquid within the nozzle into a thin sheet on the sides of the wall, which then breaks up due to liquid sheet instabilities. The air core also has an expanding effect, breaking the liquid up into ligaments, which are then affected by KH instabilities.

Slug flow is a transitional flow regime between bubbly and annular flow, and thus exhibits characteristics of both flow morphologies. The spray can be described in two distinct phases - slug phase, and fluid phase. Within the slug phase, the flow behaves like annular flow, with sheet instabilities dominating. On the other hand, in the liquid phase, the gas void fraction at the atomiser exit is very low, and bubble explosion as the primary form of atomisation dominates [23]. A diagram of the breakup mode regimes within air-assisted nozzles is shown here in Figure 2.9.

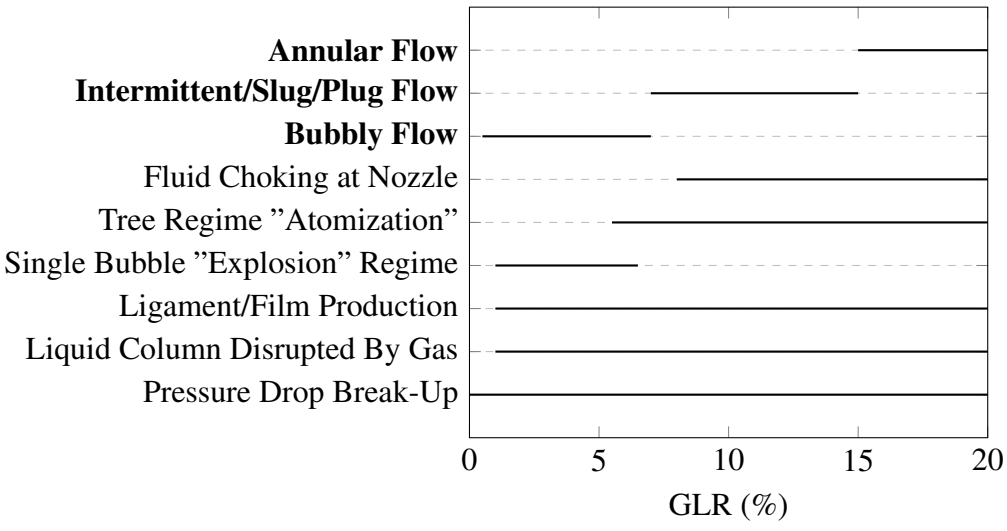

Figure 2.9: Range of operation for different break-up mechanisms. Adapted using data from [22].

Comparing Figure 2.9 with 2.7, the x axis is inverted, with Figure 2.7 plotting $Q_L/Q_A \propto 1/GLR$.

2.5 Spray characteristics of Effervescent Atomisers

The spray characteristics of flow from the atomiser are dependent on a multitude of different factors. These include the operating conditions of the atomiser, the liquid and gas intensive properties, and the internal geometry of the nozzle. The dependent variable studied here is the spray drop size, as well as the pattern. The spray drop size statistic used is the Sauter Mean Diameter (SMD). SMD is defined as the diameter of a sphere with the same volume to surface area ratio as the entire spray [24].

The most obvious influence on the spray pattern is the operating conditions of the atomiser. This includes the injection pressures and flow rates of both supply lines (and as a result, the GLR), as well as the ambient air density and temperature. The main operating parameter considered is the GLR, or gas to liquid mass ratio. Previous literature shows that as the GLR increases, the SMD decreases non-linearly, with the most pronounced effects at low GLR's. Similarly, an increase in injection pressure also decreases the SMD of the spray, likely due to the larger pressure drop, and thus bubble explosion, encountered at the nozzle exit. This correlation is shown here in Figure 2.10.

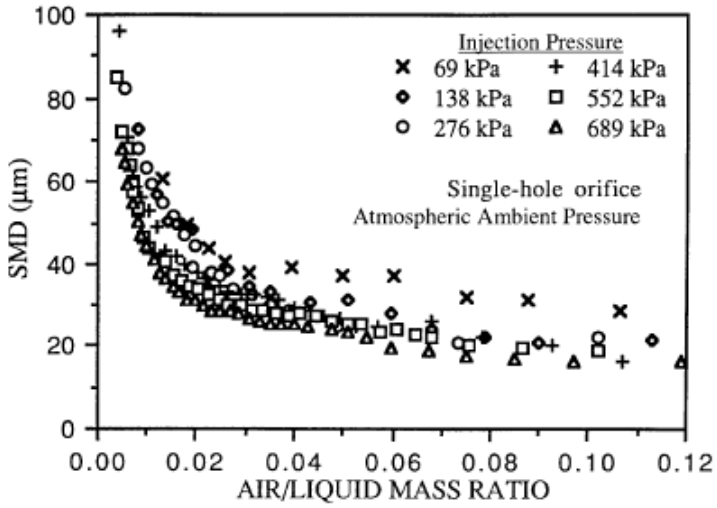

Figure 2.10: Effect of GLR and injection pressure on SMD of spray. Adapted from [15].

The internal geometry influences the atomisation of the nozzle as well. The main controlled parameters used here are the exit orifice diameter, the orifice length, and the aerator pore size/geometry. Previous literature, such as [9, 16, 17, 20] all show that the SMD is largely independent of nozzle exit diameter. This is a key advantage of effervescent atomisers, as described above, as it prevents clogging and reduces wear on nozzle components. The orifice length is nondimensionalised as the l/d ratio. Comparing this, Sovani et al. [15] shows that the SMD decreases as the l/d ratio is decreased - which is suggested to be because of reduced frictional losses. Sun et al. [19] proposes that an important influence on the SMD and spray patternation of the drop is the ratio of aerator area to exit orifice area (A_o/A_h), specifically that lower values of this ratio promote a finer spray. This may be due to the more homogeneous mixing of phases produced by smaller aeration holes. Sovani et al. [15] also suggests that the SMD decreases as distance between aerator holes and exit orifice, attributing this to the better development of the flow within the atomising nozzle.

The properties of the liquid (and gas, to a lower extent) also affect the spray produced. These most pertinently include the viscosity, surface tension, although density of the atomising gas also has an effect. These will not be tested here, and thus have not been expanded on in detail.

2.6 Unsteadiness in Effervescent Atomisation

Thus far in the literature review, time averaged characteristics of atomisers have been considered. However, fluctuation characteristics are more pertinent to the content of this thesis, and this instability analysis is what will allow us to produce better nozzles. Although effervescent atomisers perform better in regards to most of the metrics shown above compared against other types of atomisers, they do suffer from flow instabilities in operation. These instabilities arise due to the complex two-phase flow nature within the nozzle, and manifest typically as variations in the spray cone angle of a nozzle, as shown in Figure 2.11.

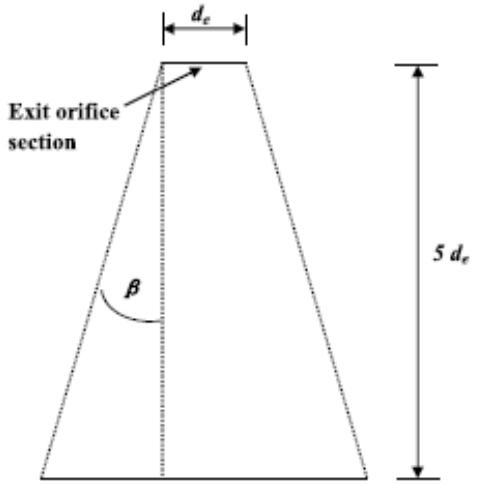

Figure 2.11: Spray cone angle of an atomised spray. Adapted from [21].

2.6.1 Instability Mechanisms

Instability within the spray ejected from effervescent nozzles is an avenue of research within current applications of this technology. The main instability generating mechanism, especially within the bubbly and slug regime, is the heterogeneity of the two phase mixture exiting the nozzle, as described by [25]. Within slug flow, the mixture immediately preceding the nozzle exit can be broadly split into two regimes: predominantly liquid - with a low gas void fraction: and predominantly gas - with a high gas void fraction. This is also further described in Figure 2.13.

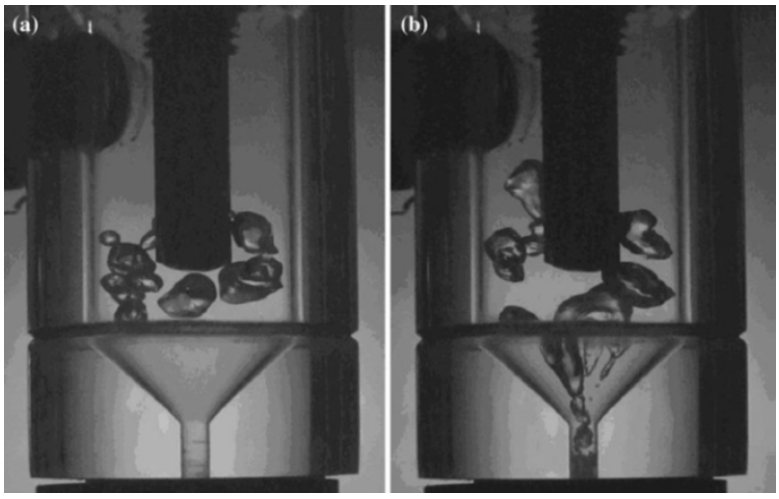

Figure 2.12: Unsteadiness in two phase mixture at nozzle exit. Adapted from [25].

In the predominantly liquid regime, which is shown in Figure 2.12a above, the mixture deforms gradually from nozzle to ambient, with minimal choking. This regime is akin to the round jet discussed at the beginning, and has a low half cone spray angle correspondingly. In comparison, under the predominantly gas regime - shown above in Figure 2.12b - the two phase flow chokes at a much lower velocity, and thus experiences a steep pressure drop at the nozzle exit. Thus, for the same mixture pressure, the nozzle exit pressure is higher. A higher pressure drop correlates with a wider spray cone angle, as tested by [26]. This effect is further compounded with the larger density of bubble explosions experienced by a packet of predominantly gas mixture exiting the nozzle.

The specific spray instabilities depend on the flow regime within the nozzle, which are outlined above. In order of increasing GLR, these are as follows. Within a bubbly flow, at low GLR, the spray cone angle fluctuates rapidly within a range of $4-18°$. This fluctuation occurs due to the effects of large pressure gradients at the nozzle exit, which cause the bubbles to stretch and coalesce in this region. This periodic bubble 'explosion' changes the local void fraction (a measure of the gas distribution within a two-phase flow), and thus affects the resultant instantaneous spray morphology, as described by [27]. As the GLR is increased, these bubble explosions occur more frequently, increasing the rate of spray cone angle variation. However, as the gas void fraction varies smoothly, so does the angle. In contrast with this, when slug flow is reached, the presence of distinct gas slugs significantly discretises the gas void fraction as a function of time, shown by [21]. As a result, the spray cone angle polarises, fluctuating between $12-18°$ when a gas slug passes through the orifice exit, and alternating to $2-6°$ when the liquid phase is dominant. Upon further increase to GLR, with the flow transitioning to an annular regime, the void fraction of the flow stays relatively constant at 0.8-1, signifying a large gas core with an interfacial film of liquid. In this regime, the effervescent atomiser behaves similarly to other air-assisted atomisers, and is thus relatively stable. These previous results highlight the importance of the local exit orifice void fraction in determining the spray cone angle, and thus the fluctuation characteristics, as shown in Figure 2.13.

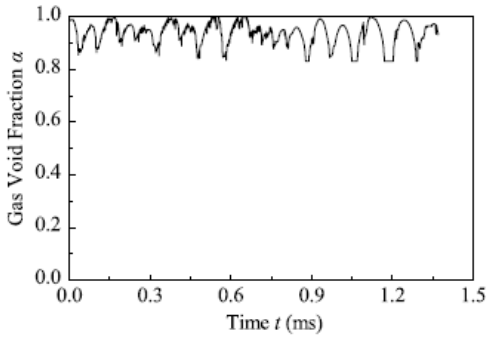

(a) Annular Flow

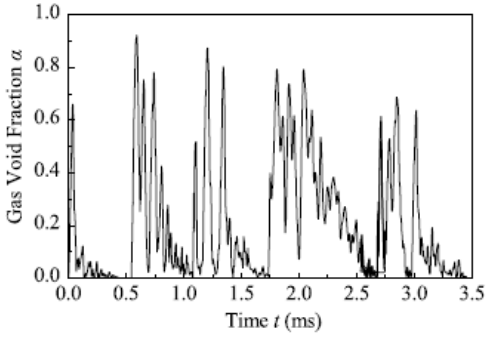

(b) Bubbly Flow

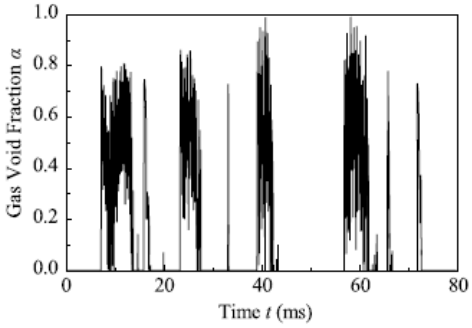

(c) Slug Flow

Figure 2.13: Gas void fraction as a function of time under various flow regimes. Adapted from [21].

In literature to date, this problem of analysing and reducing flow instabilities has been approached from a few different directions. [21] and [28] study the unsteadiness within the spatial and temporal domain, utilising statistical techniques. On the other hand [29] and [27] consider the spectral domain. A statistics based approach is useful in identifying underlying parameters affecting the fluctuations. To this end, [21] suggests the use of the following parameters for evaluating the unsteadiness within the nozzle. The first parameter is the bubble number density (ρ_b), defined as such:

$$\rho_b = \frac{6}{\pi \sum_{i=1}^{n} (d_{bi}{}^3 \cdot X_i)} \cdot \frac{GLR \cdot \frac{\rho_l}{\rho_g}}{GLR \cdot \frac{\rho_l}{\rho_g} + 1} \tag{2.6.1.1}$$

Here, d_{bi} is the measured bubble diameter, which is observed from image processing the nozzle exit, and X_i is the percentage of bubbles with a diameter d_{bi}. All other parameters are defined previously. As bubble number density increases within a nozzle, the time averaged spray cone angle also increases, nonlinearly. However, the fluctuation statistics show a different view. Achieving a maximum fluctuation at 500 cm^{-1}, the mean variation within the flow decreases as the density increases past this peak. This may be due to the higher homogenisation of the two phase mixture in the presence of a large density of small bubbles, compared to smaller, more distinct phases - as experienced within the slug flow regime. The mean variation coefficient is defined as follows:

$$CV_\beta = \frac{\sigma_\beta}{\bar{\beta}} \tag{2.6.1.2}$$

Here, σ_β is the standard deviation of the spray cone angle, and $\bar{\beta}$ is the mean spray cone angle. Both of these values will be measured experimentally. As demonstrated by [21], an increase in this variation coefficient corresponds to a large fluctuation in the spray cone angle, encompassing the instabilities within the flow. The time averaged and fluctuation characteristics of the bubble number density variation are shown in Figure 2.14.

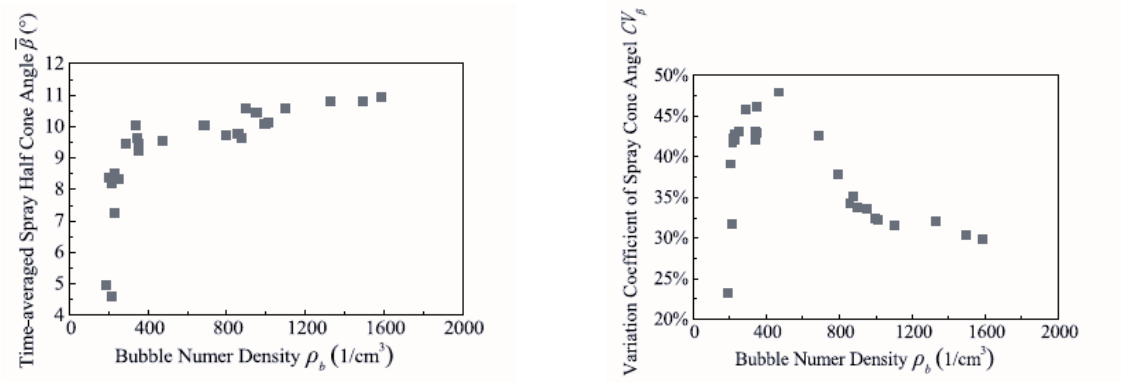

(a) Average spray cone angle vs rho_β (b) CV_β vs ρ_β

Figure 2.14: Average and fluctuation characteristics vs Bubble Number Density. Adapted from [21].

While the statistical approach employed above is useful in determining the pertinent factors for cone angle fluctuation, to provide high speed control, a frequency analysis is also necessary. The method used for this is similar to the one proposed by [27]. Their results show that the fluctuation frequency of the nozzle is closely correlated to the slug passage frequency within the nozzle, which is a function of the GLR, as well as the speed of sound within the two phase mixture. The speed of sound within the composite mixture can be approximated as follows:

$$a_{m,p} = \frac{a_{E,L} a_{E,G}}{(1-\alpha) a_{E,G} + \alpha a_{E,L}} \tag{2.6.1.3}$$

Here, α is the gas void fraction, and $a_{E,L}$ and $a_{E,G}$ are the effective wave velocities for the liquid and gas, respectively, within a two phase flow. They are calculated as follows:

$$a_{E,L} = 1/\sqrt{\frac{1-\alpha}{a_L^2} + \frac{\alpha\rho_l}{\rho_g a_G^2}}, a_{E,G} = 1/\sqrt{\frac{\alpha}{a_G^2} + \frac{(1-\alpha)\rho_g}{\rho t a_L^2}} \tag{2.6.1.4}$$

From this, the slug passage frequency, f_s is shown to be correlated to the liquid velocity, U_L as such: $f_s \sim U_L^{1.2}$. The correlation between the slug passage frequency, and the speed of sound within the flow, is shown here in Figure 2.15:

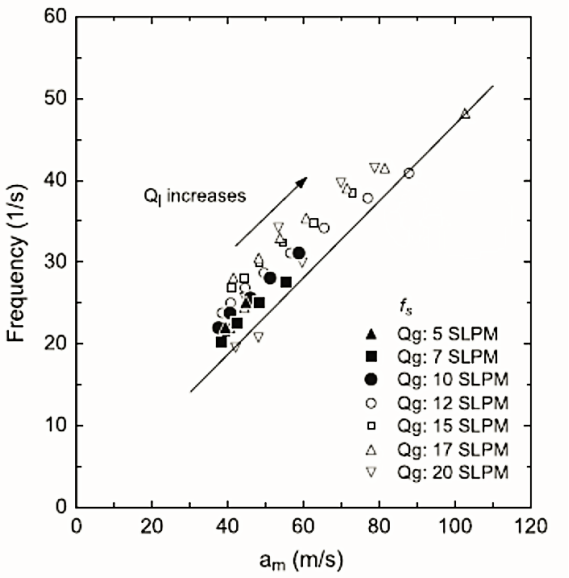

Figure 2.15: Slug passage frequency vs speed of sound in flow. Adapted from [27].

2.7 Gas-liquid Mixing

Understanding how two-phase mixtures interact will yield insight into the nature of instability within an effervescent nozzle. As such, a knowledge base on the theory of gas-liquid mixing is valuable. Gas liquid mixing is an important part of process engineering, used primarily for gas absorption, chemical reactions, or humidification [30].

Although a primary component of the atomisation mechanism in effervescent nozzles, two-phase gas-liquid mixing has primarily been studied in the context of industrial processes. As such, applying the same criteria to nozzles, which have substantially different flow characteristics, may not be suitable. Nevertheless, this allows for a good starting point. Here, both working fluids are considered low viscosity, and the system is kinetically limited [31].

Mixing processes are generally controlled by the power dissipated in the fluids, as well as the gas volume fraction Φ_g. This influences the produced bubble size [32]. The bubbles are produced in a high-shear zone (in the case of the atomiser, the aerator tube outlets). The power dissipated can also come from the use of impeller systems, as is common in industrial processes, however, for effervescent atomisers, this is unfeasible. As a result, the power dissipation here is a function of the gas flow rate, as well as internal pressures, and geometry. Mixing literature also highlights the importance of the Stokes number [33]. Stokes number characterises the response of the dispersed phase (bubbles) to velocity changes in the continuous phase (water), and is defined as follows:

$$St = \frac{\rho_d d_d^2 v_c}{18 \mu_c D} \tag{2.7.0.1}$$

Here, d is the particle diameter, and v_c is the continuous velocity. For $St << 1$, which is the case for effervescent atomisers, the particles track the flow well, and performance decreases with an increase in the Stokes number. An increase in GLR tends to lead to lower Stokes numbers [33]. The gradient of the Stokes number distribution also offers some information. Particularly, it may indicate the ratio of drop breakup to coalescence, and suggests that coalescence dominates at the edges of the spray, as shown here:

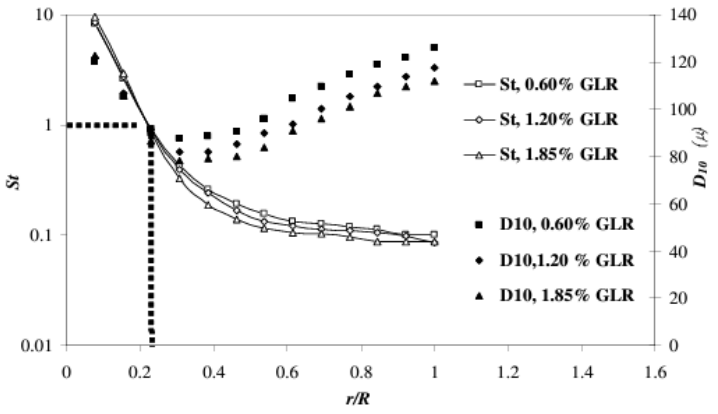

Figure 2.16: Effect of GLR on the Stokes Number. Adapted from [33].

Emulsion processes are also useful for analysing the effect of the two-phase nature of the flow. Consider the mixture here an immiscible two phase mixture, within a fluid of low viscosity. Studies on the theory of emulsion also highlight the importance of the shear rate of the flow on the produced droplet size [34]. An important parameter is the viscosity ratio, defined as:

$$R = \frac{\mu_{drop}}{\mu_{cont}} \tag{2.7.0.2}$$

This ratio plays a role in the deformation pattern of the droplet, with a critical range of magnitudes ($R \sim 0.01 - 1$) where droplet breakup is much more prominent, highlighting the complex role of viscosity in breakup, which can both help and hinder droplet formation [30]. Similarly, an increase in surface tension also destabilises the system. Mixing processes highlight the importance of mixing time to improve the dispersion qualities of the two-phase system [31]. Flows that are allowed to mix for longer, applicable to nozzles where the diffusion occurs well before nozzle exit, have more uniform dispersion, and thus may lead to more stable sprays.

The data gleaned from two phase mixing can be used to design better nozzles for fluid mixing. However, as the improvement is aimed to be retrofittable onto existing nozzles, this avenue will not be pursued further. An analysis of producing an optimum nozzle contour for a given set of operating conditions is shown in [35].

2.8 Optical Diagnostics and Measurements of Sprays

Sprays are an inherently stochastic process, and thus spray imaging relies on repeated measurement to understand time averaged and instability characteristics. Spray modelling is also insufficiently accurate and predictive for complex phenomena such as atomisation, and thus experimental testing is necessary to verify theoretical results [36].

There are three principle spray areas highlighted in existing research. Moving from upstream to downstream, these are as follows: internal nozzle flow, near nozzle spray formation region, and far field developed spray region, as shown here:

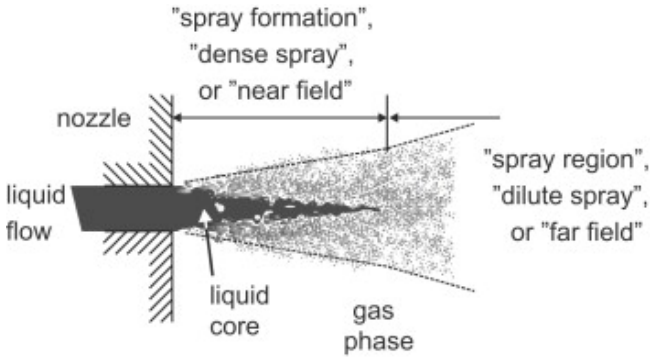

Figure 2.17: Regions of a spray. Adapted from [36].

The flow within the nozzle governs the mass flow rate, as well as initial atomisation properties, within the spray. It is sensitive to local temperature, pressure fluctuations, and the physical properties of the fluid [36]. Current techniques such has LDV and PIV yield useful information about the effects of internal flow phenomena on the external spray. However, due to the idealisation of nozzle geometry (e.g. 2D geometry), as well as simplification of internal passages and curvatures necessarily implies that such methods are limited in quantitative accuracy, and better modelling is needed for predictive simulation [37].

The gas void fraction within a nozzle as a function of time can be measured using techniques such as time-integrated focused synchrotron x-ray absorption [36]. Though this method has been used to measure gas production due to cavitation, a similar technique may be leveraged to provide gas bubble density in effervescent atomisers [38]. This method works by using x-ray diffraction. The liquid phase scatters the x-rays weakly and absorbs most of them, while the gas phase leads to an increase in transmitted beam intensity, as there are fewer absorbers in the path of the beam. To ensure a temporally and spatially accurate measurement, the incoming x-rays need to have high coherence and resolution, requiring the need for a focused synchrotron [38].

Measurements immediately downstream of the nozzle in the spray-formation region are just as important. The techniques used in this area are usually optical in nature, however the density of the spray in this region poses some challenges [36]. For effervescent nozzles, which tend to have almost no intact length, on the order of a nozzle diameter at maximum, this area is difficult to probe. Techniques using both electrical and optical connectivity are used. For the optical approach, the liquid entering the nozzle is seeded with a fluorescent tracer, and a laser beam is shined upon the nozzle spray core. This has the benefit of being simple and relatively noninvasive, and also provides more structural information as the data is produced as an image [39].

For dense spray regions, such as the near nozzle region, multiple scattering can have an adverse effect on the quality of measurements produced. While most optical systems work on the principle of light scattering (e.g. PDA and PIV), the coherence of the light signal at the optics must be preserved to glean information about the spray. Multiple scattering events within the spray thus lead to a decrease in coherence, contributing to background noise, or producing misleading results [36]. The amount of multiply scattered light is dependent on the average optical depth (a measure of the average ratio of spray diameter a photon penetrates) and the number density (the average number of droplets per volume) [39]. This effect can be mitigated by either using multiple illumination angles and composing them, as is done for PIV, or by using the coherence to discriminate against multiple scattering in measurement principle, similarly to a PDA device.

The far field spray region has had the most detailed spray measurements to date, owing to its lower droplet density and thus better imaging quality characteristics [36]. Optical imaging can be used to some efficacy, however, computational and technical requirements usually favour other methods such as back-illumination/shadowgraph imaging, PTV or PDA.

The simplest optical diagnostics technique focuses on measurements of macroscopic properties, such as cone angle, spray penetration - both axial and radial, mass flow rate, momentum flux, and spray patternation [40]. These characteristics have been measured using volume illumination - used to visualise the entire spray volume, back illumination, shadowgraph and schlieren techniques.

Shadowgraphy imaging technique works on the principle of refraction. Changes in density lead to a change in the refractive index of a material, and more so in two phase flows. A light source is placed in front of the measurement object, with a recording plane behind. As light passes through the object, changes in refractive index lead to the light being deflected non-uniformly behind the object. This difference is picked up by the recording plane. The intensity of the image produced correlates to the second derivative of refractive index at the pixel measured [41].

Schlieren also works in a similar manner. Changes in the angle of refraction, again, are measured. However, schlieren setups tend to have a two lens setup: before, and after, the measurement volume. A knife edge, or similar, is placed at the foci of the lens. This knife edge is set up in such a fashion as to block all of the deflected rays, while allowing the undeflected light to pass through [41].

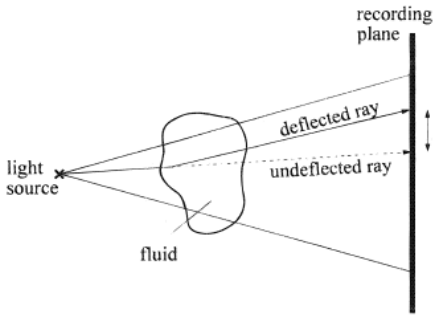

(a) Visualisation of Shadowgraphy

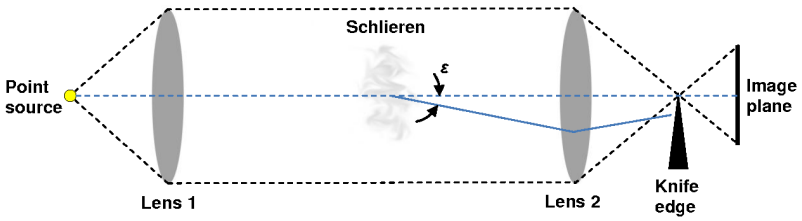

(b) Diagram of a typical schlieren setup

Figure 2.18: Examples of shadowgraphy and schlieren techniques. Adapted from [41].

While these techniques can, in cases, effectively measure macroscopic properties, the trend towards microscopic measurements, such as droplet size, velocity, temperature, and volume flux has necessitated the need for more quantitative measuring techniques. These include Phase Doppler anemometry (PDA), Particle Image velocimetry (PIV), Planar Laser-Induced Fluorescence (PLIF), as well as more digital techniques, such as high speed imaging and analysis [36].

2.8.1 Particle Imaging Velocimetry

The idea of using tracer particles to visualise flow fields was first implemented by Ludwig Prandtl [42]. Using crushed mica powder as the tracer particles, Prandtl was able to visualise the flow around a wing by manually pushing water through a tunnel. This allowed him to study fluid structures such as separation points and recirculation zones. This is the same principle upon which PIV operates. The setup of a PIV system consists of several subsystems: a flow seeded with tracer particles, a laser illumination system, and imaging optics. Further image processing is usually also required for quantitative measurements [43]. A diagram of the setup is shown here:

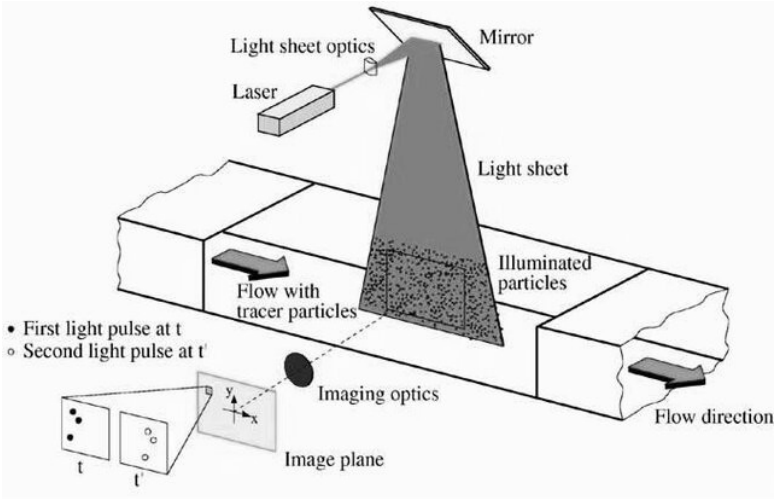

Figure 2.19: Experimental arrangement for PIV measurements. Adapted from [43].

The laser illuminates a continuously moving flow seeded with tracer particles to track instantaneous movement within the fluid in a single plane. The imaging optics receive the light reflected off the tracer particles. This light is recorded either as a frame, or a series of frames. The velocity of the particles is calculated by taking a sequence of images separated by short time intervals, and tracking the movements of the tracers [44].

The measurements from the PIV recording are broken into smaller evaluation units named *interrogation areas*, ideally with $\sim$ 10-20 droplets each. The local displacement vector between two subsequent images is determined using auto- and cross-correlation, assuming all particles in the interrogation area move locally homogeneously [44]. Using knowledge of the time delay between images, this reconstructs the velocity field within the flow at the instance of the image recording. By tiling the interrogation areas together, a visualisation of the flow field is possible for the entire plane. For sufficiently dilute sprays, where individual tracer particles can be traced between flows, Particle Tracking Velocimetry (PTV) is also a sufficient alternative [36].

For two-phase flows, PIV can be used to monitor the difference between the gas and liquid phases with some modifications. The gas is usually seeded with tracer particles sufficiently different enough to the liquid phase and liquid tracers to be easily distinguishable. This is based on the assumption that the gas particles, and thus the tracers, are much smaller than the droplets [36]. Another approach is to distinguish the phases based on the variation in wavelength of fluorescent vs scattered light. For example, the liquid phase may be doped with a fluorescent dye, with scattering detected from particles in the gas phase (or, vice versa).

In contrast to other techniques such as Hot wire Anemometry (HWA) and pressure tubes, PIV is much less obtrusive in nature. The tracer particles are specifically chosen to not impede flow movement, and being an optical technique, the rest of the setup is non-intrusive [43]. The large area of analysis,

especially after tiling, is also a valuable advantage, allowing for visualisation of a flow field in a range of scales, and with accurate physical models. The spatial resolution of PIV is large, while the temporal resolution is somewhat limited by the optics' frame rate.

Though this is an absolute technique, measurement calibration is still required. The tracer particles must be checked to ensure they follow the flow field faithfully [44], as smaller particles follow the flow better. A high power light source is necessary to provide sufficient reflected light for the optics to pick up. This is especially important to improve temporal resolution, as the interplay between particle size, light reflection, and maximum frame speed must be carefully optimised to better measurement accuracy.

The timing and coordination of the imaging setup is also necessary. The pulsation frequency of the laser optic must follow the frame speed, while ensuring that each pulse is short enough to 'freeze' the motion of the particles, as *streaking* blurs the image and reduces accuracy.

2.8.2 Phase Doppler Anemometry

Phase Doppler anemometry was developed in the 1980's to measure droplet size and velocity simultaneously. PDA has superseded some of the limitations with PIV, allowing for measurement of both position and velocity simultaneously. However, PIV is much more accessible, and thus is still used widely [44]. Similarly to Laser Doppler anemometry (LDA), PDA uses light scattering from two intersecting laser beams. The light interferes at three detectors precisely placed to produce Doppler burst signals. The frequency from these signals is proportional to the velocity of the particles, and the phase is related to the droplet diameter through Mie scattering theory. This theory shows that the intensity of scattering is a function of the wavelength of incident light as well as the diameter of the particle [45].

The parameters important in PDA configuration are the beam intersection angle (2Θ), the scattering angle (ϕ) and the elevation angle (Ψ). These are shown below in Figure 2.20. The polarisation of the laser beams, the focal length of the detector, and the shape of the detector aperture also affect the measurement.

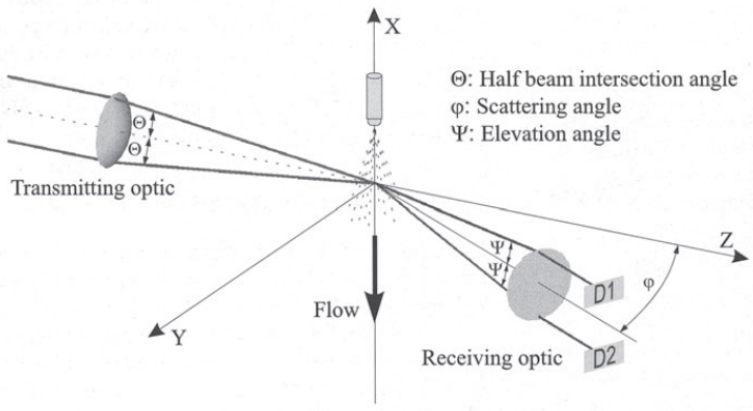

Figure 2.20: 1 dimensional Phase Doppler setup. Adapted from [46].

When a particle moves through the measurement area, it scatters light from the two incoming beams to different directions. When these scatter bursts intersect, as they are phase shifted, they create a Doppler burst [46]. This burst is detected by two photo detectors. This phase difference between the detectors is linearly proportional to particle diameter. Note here that the light incident on the particle is both reflected off, or refracted within the particle. However, this linear dependence holds for both cases [46]. The relationship between the phase difference (Φ) and the diameter is shown here.

For reflection:

$$\Phi = \frac{2\pi D}{\lambda} \frac{\sin\Theta \sin\Psi}{\sqrt{2(1-q)}}; \qquad \sin\Theta\sin\Psi << q \tag{2.8.2.1}$$

And for first order refraction (laser beam internally refracts once):

$$\Phi = \frac{-2\pi D}{\lambda} \frac{m\sin\Theta\sin\Psi}{\sqrt{2(1+q)\left(1+m^2-m\sqrt{2(1+q)}\right)}}; \quad m > 1 \tag{2.8.2.2}$$

Here, m is the refractive index of the droplet, and q is a grouping of cosine's as follows:

$$q = \cos\Theta\cos\Psi\cos\phi \tag{2.8.2.3}$$

In PDA, Φ is measured, while all angles, wavelength, and refractive index is known. This thus allows for calculation of D. However, as seen by the above two equations, for a given setup, refraction and reflection cause opposing phase shifts (highlighted by the opposite signs in the formula's above). Thus, a predominant scattering mode is needed. This relativity is dependent on the scattering angle (ϕ), as well as the polarisation of the beams. For example, at low scattering angles, first order refraction is much more dominant than reflection, independent of polarisation. Usually, angle of incidence is set at *Brewster's Angle*, which is the angle at which light of a specific polarisation is fully refracted, with no reflection. This gives first order refraction as the dominant mode, allowing for the phase diameter relationship to be calculated. For a water droplet of $10\mu m$ in air with parallel polarisation, this angle is approximately 74° [46].

As the measured phase shift between two detectors must lie between 0° and 360°, diameter values which give phase shifts higher than this range may cause measurement problems (i.e. a large particle with a phase shift of over 360° may get misinterpreted as a small particle with a phase shift in the measurable range). To remove this ambiguity, a third detector is usually used. This third detector is placed preferentially closer to one of the other two detectors, and thus provides a different Φ relationship, removing the ambiguity [46].

Measurement accuracy is the main improvement of PDA systems over earlier analysis techniques. However, measurement errors still require minimisation. Measurement accuracy increases with the quality of analysed signals. A higher quality signal is produced by reducing the signal to noise ratio. This can be done by increasing the light intensity, or improving the quality of the laser intersection area [46]. Improvements to measurement accuracy can be analysed by considering the phase-diameter relation. This relation is effected by non-homogeneities in the liquid, as well as non-sphericity of the droplets. Mie scattering theory requires spherical droplets for accurate observation, and any deviation from this will reduce prediction accuracy [36].

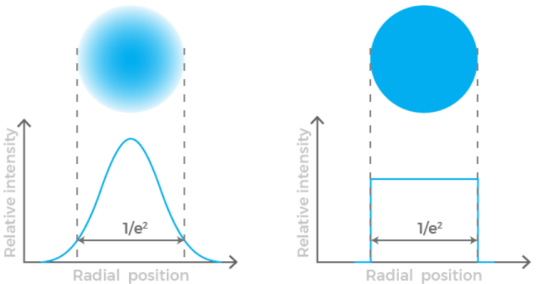

Figure 2.21: Comparison of beam intensity profiles. Adapted from [46].

More mechanically, the position of droplets within the measurement volume can also cause inaccuracies. The first possible measurement error is called the *Gaussian beam intensity effect*. For most conventional lasers, the intensity profile at their focusing point is a Gaussian function (compared to a 'flat-top' laser in the image above). For a particle large enough, this variation in the intensity profile can change the dominant mode of scattering, from refraction to reflection, dependent on the position of the particle within the measurement volume, thus causing inaccuracies [47]. Particles partially within the volume can also scatter light asymmetrically, reducing the quality of the measurements. This is called the *Slit effect*.

2.9 Image Processing

Improving the quality of data extracted from testing images is an important aspect of correctly characterising the factors affecting spray performance, as well as ascertaining whether control methods are effective in mitigating the given spray instability. The camera used for this experiment is the LaVision *HighSpeedStar* 6 CMOS camera, which is capable of imaging at up to 40 kfps (40000 frames per second). Using the Nyquist sampling theorem, this gives an ideal max frequency of the instability that is able to be accurately imaged at up to 4 kfps, and if necessary, up to 20 kfps. The driving frequency in the instability mechanism is estimated at 1000 Hz, which should be adequately sampled by the camera.

An increase in the imaging frame rate also affects the exposure timing. Correct exposure is necessary to accurately capture the nature of the flow. If the exposure time is too long, the motion is smeared out, leading to blurry and streaked images. If too short, not enough light is captured to accurately resolve the image [48]. Furthermore, the exposure time is not necessarily the time between two frames (known as the interframe time). For example, consider this image taken of a pistol shrimp.

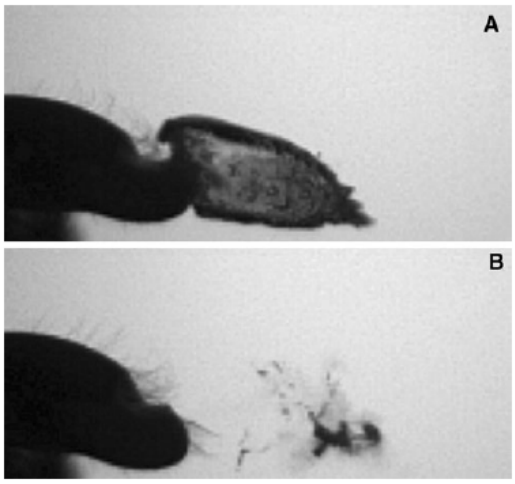

Figure 2.22: High speed image of shrimp producing cavitation bubble. Adapted from [48].

The cavitation bubble visible in image a only lasts for $\sim$ 300 µs. These images were taken at 2 kfps, which gives an interframe time of 500 µs. Thus, a much shorter exposure time is needed to capture small details within the bubble. To resolve further details, however, the exposure and interframe times should be on the same timescale.

Next, the data from these images must be extracted in means of producing inter-image analysis. Improving the processing speed and the memory requirements needed for this is necessary. *Binarisation* is used for this data compaction, as well as to separate foreground - fluid flow - from the background - internals of the nozzle, or far field background. Binarisation is the process of reducing a grayscale image into two levels - black and white. The output from a camera is considered a native image - representing the amount of light extinction at a certain pixel. For binarisation, if this intensity is above a certain threshold, the intensity of that pixel is set to 1. Else, it is set to 0.

The choice of threshold for splitting the image is an important one, and various values will be tested for optimacy. The threshold can be applied locally or globally, and other filter based methods are also used for this [49]. However, for the case of internal flow being studied here, these are unnecessary, as the entire imaging plane will be relatively uniform. The two competing interactions in choosing an appropriate binarisation criterion are as follows. First, for the preservation of as much image information, the threshold should be set low. This will allow the inclusion of the density information even at points where light intensity is relatively low. However, this also leads to pixel saturation

within the image. Pixel saturation, in this case, represents regions of the image where the entire local area is above the threshold, being set to 1. As the flow morphology here is relatively turbulent, the likelihood of a region with uniform density is extremely low, and thus should not be represented in the binarised images [50]. Shown here is an example of the same spray image under multiple thresholds to highlight this effect:

(a) $b_{thresh} = 1000$ (b) $b_{thresh} = 1200$ (c) $b_{thresh} = 1400$ (d) Original Image

Figure 2.23: Effect of binarisation threshold on 12bit grayscale image

As expected, the optimal threshold is somewhere between the extremes described above. Creating a function which can appropriately combine the two interactions will help with identification of the optimal threshold. First, consider ζ as the threshold relative to the maximum intensity of any pixel within the image considered. This will act as a normalising variable, and the binarisation optimisation function will be considered will be evaluated in terms of this.

To suitably calculate the optimum binarisation threshold, a large sample of images should be considered. As such, the change between pixel intensity between images is an important consideration. For a given pixel, let p denote the probability that the pixel is illuminated across all images in a sample. For example, $n_{p=50}$ denotes the number of pixels in a *Region of Interest* (ROI) such that the pixel is illuminated in half the images in a sample.

To account for the influence of trying to minimise saturation, consider the first function as follows:

$$f_1(\zeta) = n_{p=100} \tag{2.9.0.1}$$

As explained above, here $n_{p=100}$ is the number of pixels in the ROI such that the pixel is illuminated in every image in a sample. This is an appropriate extension of saturation, as pixels that fall into this category are much more likely to be saturated under a given binarisation threshold [49].

Next, to maximise the amount of data retention, let the second function be as follows:

$$f_2(\zeta) = \frac{1}{n_{p>0} - n_{p=100}} \tag{2.9.0.2}$$

Minimising this function must involve maximising the number of pixels that are included in the binarisation, but not saturated. These functions are normalised and combined to form the binarisation optimisation function used later in this thesis, as follows:

$$F(\zeta) = \frac{n_{p=100}}{(n_{p=100})_{max}} + \frac{(n_{p>0} - n_{p=100})_{max}}{n_{p>0} - n_{p=100}} \tag{2.9.0.3}$$

Here, the subscript max denotes the maximum of each respective set over the set of thresholds tested, and normalisation is undertaken to value both effects equally.

If the chosen ROI within the image is small enough as to only cover a single transient feature within the nozzle, this binarised image can be further ensemble averaged to produce a single point of data: the average light intensity in the region at imaging time. This data set produces a time series for the average light intensity. As light intensity is a direct function of the density of the flow - and thus gas void fraction in this region - this gives a measure of the average gas void fraction over time in the region of interest. A Fourier transform on this time series will produce a spectrogram of the dominant frequencies of void fraction changes, which should correspond to the slug/bubble passage frequency. Once the slug passage frequency is experimentally verified, the solenoids can be driven at these frequencies to mitigate the instabilities.

Another possible method of tracking the passage frequency is to utilise drop detection. Over a larger ROI, the tracking of multiple distinct bubbles simultaneously will produce information about the spatial spread of the bubbles throughout the nozzle. While this improves the accuracy of data in well defined bubble flows, droplet detection and tracking is much more difficult in churned and turbulent flows such as the one present in the nozzle.

Noise will have an important effect on the data collected here, as any sources of noise, especially periodic noise, will adversely change the output spectrogram from this analysis. The main sources of noise here include camera sensor noise, which impacts all images taken randomly, with no repetitive patterns, although it can still be considered high frequency [51]. Quantization noise will also affect the output signal received from the camera, and will be of the order of the frame rate, and thus high frequency. In most cases, these disturbances can be removed from the final image by passing the images through a low pass filter, and thus performing smoothing. However, in this case, as the instabilities are of a similar frequency, another method must be utilised. The ambient conditions also impose a noise upon the measurements, notably changes in the background illumination, as well as jittering in the camera setup. These can be appropriately removed through careful pre-processing of images, as well as intensity correction filters [52].

As highlighted above, choosing the correct ROI is key for producing usable data for analysis. The region should be small, covering only a section of the internals of the nozzle. This will allow for transient features to be tracked easily as they transition through the ROI. The ROI should also be placed close to the junction point of the air and water lines, as this will be the area of most turbulence, and thus should highlight the instabilities present. This will be explored experimentally in Chapter 4.

2.9.1 Proper Orthogonal Decomposition

Another technique explored in this thesis is *Proper orthogonal decomposition* (POD). POD is a numerical method, and is used to reduce the complexity of a set of data. It is a subset of a class of algorithms classified as *model order reduction* algorithms [53]. POD generalises the concept of an eigen-decomposition to non-square matrices. It decomposes a given scalar (or vector) field $\rho(x,t)$, in this case the spatial density field, into a set of deterministic spatial functions $\phi(x)$ that are regulated by a set of time coefficients $a(t)$, as shown here:

$$\rho(x,t) = \sum_{0}^{n} \phi_k(x) a_k(t) \tag{2.9.1.1}$$

Thus, the field can be broken into distinct spatial 'modes' which evolve over time to produce the entire scalar field. In other notation:

$$M_\rho = U(x) \times \sigma \times V(t)^T \tag{2.9.1.2}$$

Here, M_ρ is the matrix representation of the scalar field, U is the spatial mode matrix, σ is a diagonal matrix, with the entries encapsulating the relative dominance of the modes, and V is the temporal mode matrix, which denotes how each spatial mode evolves over the time period of the dataset. To create a matrix representation of ρ from image data, consider a set of n images of size $w \times h$, separated by some time Δt. Constructing a matrix from this data set will require encoding both the spatial and temporal data. Let p_k denote the k^{th} image in a data set. Then:

$$p_k = M_{l,w} \equiv M_{lw,1} \tag{2.9.1.3}$$

This is akin to flattening each image into a one dimensional vector. Then, the field matrix can be created by concatenating these image vectors, as shown here:

$$M_\rho = [p_1|p_2|p_3|...|p_n] \tag{2.9.1.4}$$

Giving a matrix of dimension $lw \times n$. Note that in this matrix, each row corresponds to a single pixel as it evolves over time.

Computing the POD is done through an iterative algorithm, and in this case, the *MATLAB* function 'svd' is used. Once computed, columns of the U matrix correlate to the various modes present in the data. The corresponding rows in the V matrix correlate to the evolution of each mode. The reduction of complexity comes in the fact that using the σ diagonal matrix, the POD can be truncated to the desired accuracy, resulting in computational efficiency. Using an FFT on the rows of V shows the dominant frequencies present in each oscillating mode.

2.10 High Speed Control (Feedback Control)

Mitigating the instabilities present in the nozzle requires the use of high speed, feedback control. The idea behind feedback control is to use the output of a system to influence the inputs into the system in the future. This leads to four main criteria for effectiveness of feedback control [54]. These are as follows:

1. The system must stay stable at all times.
2. The system output must track the command input given.
3. The system output should be insensitive to disturbing inputs.
4. The system should meet the goals even with a lack of completely accurate model, and under changing dynamics.

In the case of stability, two cases should be considered. The first being that the control should improve the instability inherent within the system - for example, mitigating the instability in spray nozzle angle. The control strategy should also not drive the system to instability - where the feedback signal worsens the stability of the system, instead of improving it. This depends on the choice of output measured, as well as the control strategy used [54].

For most cases, the output tracking of the command is an intuitively understood dynamic. For example, a lane correction system requires the car to stay within a lane, the command input given. In the case of this nozzle, the command input will be the instantaneous flow rate through the solenoids, and the nozzle should track this change internally, leading to a smooth variation in the gas void fraction. Success here depends on the physical geometry of the setup, the speed of the solenoids, and the hydrodynamic properties of both fluids.

Disturbance rejection is an essential property of feedback control. In addition to removing the instability inherent in the system, the controller chosen must also be able to handle local disturbances. For example, local changes in turbulence intensity, or instantaneous variations in supply rates, should minimally affect the output performance of the nozzle. However, this will not be the main focus, as the testing will be run in precisely controlled conditions for the initial implementation of this method.

Robustness is the final criteria. The system must be able to perform well under a variety of operating conditions, including different supply pressures and rates, as well as changes in ambient conditions. Adapting the system to work for various fluid combinations would be most promising goal. In addition to this, modelling the internal dynamics of the two phase flow within the nozzle is infeasible due to the nonlinearities involved, and the controller must be able to work with a simplified model. This will be affected mostly by the control strategy used for the system.

2.10.1 PID Control

PID control, short for Proportional-Integral-Derivative control, is a widely used feedback control technique in engineering and automation systems, and one of the simplest ones to implement. It plays a crucial role in regulating the behavior of dynamic systems by continuously adjusting control parameters to maintain desired performance criteria. The PID controller operates by comparing the system's actual output with a desired tracking signal and generating a control signal based on this error [54]. This control signal is then used to adjust the system's inputs or outputs, effectively steering it towards the desired state. PID control offers a versatile and effective solution for a wide range of applications, including but not limited to robotics, process control, and fluid systems.

Proportional Control (P): The first component of a PID controller, acts to reduce the current error between the desired and actual spray characteristics. This term adjusts the control action in direct proportion to the magnitude of the error signal. In the context of stabilizing the effervescent atomizer nozzle, the proportional term modulates parameters such as gas or liquid flow rates based on deviations in spray cone angle or other relevant parameters captured by sensors. By providing immediate corrective action proportional to the error, proportional control contributes to the overall stability of the spray system.

Integral Control (I): The second component of a PID controller, addresses any persistent steady-state errors that may exist between the desired and actual spray characteristics. This term accumulates the error over time and adjusts the control action accordingly. In the effervescent atomizer nozzle application, integral control continuously corrects for any residual errors in spray characteristics, ensuring precise and stable control. By integrating the error signal over time, integral control helps to eliminate long-term deviations from the desired setpoint, thereby enhancing the overall accuracy and consistency of the spray system.

Derivative Control (D): The third component of a PID controller, anticipates future trends in the error signal by considering its rate of change. This term acts to dampen oscillations and improve the transient response of the control system. In the context of stabilizing the effervescent atomizer nozzle, derivative control helps to preemptively counteract instabilities before they fully manifest. By adjusting the control action based on the rate of change of the error signal, derivative control enhances the stability and responsiveness of the spray system, contributing to smoother and more precise control of spray characteristics.

Similar control algorithms have been implemented in the past. Osuna-Orozco et al. in [55] used light attenuation measurements of the spray profile to control the inlet rates of their fluid flow. The control strategy used was to minimise the RMSE (Root mean square error) between the measured spray profile, compared to some set spray profile. A PID controller was used for this strategy, and produced promising results. Although applied to a coaxial swirl atomiser, a similar process should be successful in effervescent atomisers also.

Bothell et al. in [56] also use a PID controller to improve the characteristics of a swirl atomiser. The input signal used is the spray cone angle, which is measured using a high speed imaging setup. The control strategy is to maximise the spray cone angle, but this can be adopted to track a reference angle instead. The control inputs used are the ratio of swirling to non-swirling gas rates used, due to the effect of the *Swirl Ratio* on the cone angle.

2.11 Pulsed Atomisation

The concept of pulsing atomisation is not a new one. Pulsed atomisers have been used for various purposes, such as fuel injectors and spray driers, for years. As such, exploring the atomisation behaviour of nozzles under pulsed conditions may lead to insights on the instabilities present in such an atomising mode, and how to mitigate them.

Kim and Lai in [57] found that the atomisation structure under a variation in pulsation frequency depends significantly on the atomiser design, as well as the operating conditions of the nozzle. For airblast nozzles, which work similarly to the effervescent nozzles studied, an increase in the pulsation frequency leads to an increase in droplet density, as well as shorter breakup lengths. However, this is a non-linear process, and there exists a peak frequency, dependent on the operating conditions. In the conditions tested, this was found to be $\sim$ 19 Hz. Chang et al. in [58] also agree with this result. Some example sprays are shown here:

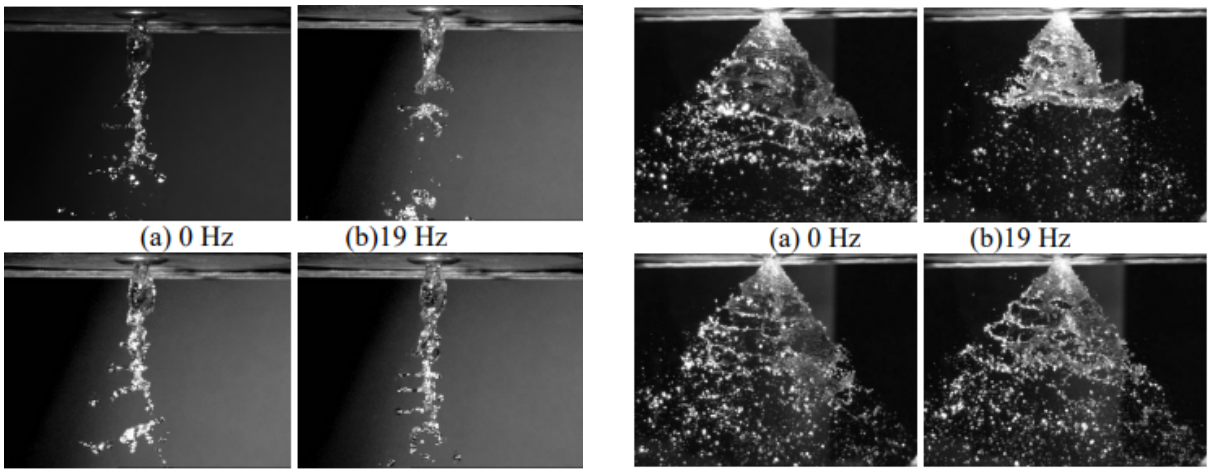

(a) Water flow rate: 0.3 GPM (b) Water flow rate: 1.2 GPM

Figure 2.24: Effect of pulsation frequency on spray structure. Adapted from [57].

An increase in frequency also tends towards a more uniform spray, with a wider distribution on the volume flux. However, the effects on the droplet size, measured as SMD, is minimal, showing $< 5\%$ variation over the range of frequencies tested [57]. Shown below here is the droplet density and volume flux as a function of radial distance, highlighting the variation in spread at different frequencies:

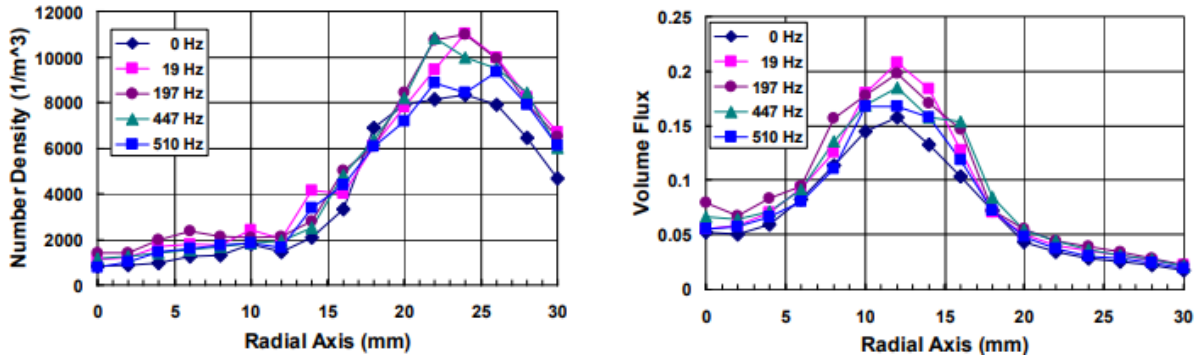

(a) Number density (b) Volume flux

Figure 2.25: Effect of pulsation frequency on spray characteristics as a function of radial distance. Adapted from [57].

2.12 Motivation

To allow the usage and proliferation of effervescent atomisers into more industries, and operating conditions, the instability characteristics of the atomisers should be improved upon. Previous work into this has detailed studying the characteristics of newly developed atomiser designs, as shown by [59–61]. For example, [60] proposes a new atomiser design which promotes annular flow even at very low GLR's, or [59], whose design utilises tangential fluid inlets to produce a better homogenisation of the two-phase flow. Multiple atomisation techniques have also been combined, as in [61], which combines the bubble-explosion breakup mode of effervescent atomisers, with the sheet disintegration breakup mode typified by airblast atomisers, as described by [62]. While these produce promising results, they require the use of specifically developed atomiser designs, and thus are not flexible for existing applications. In contrast, a high speed control system can be retroactively fitted to existing atomisers, and many applications already have fluid inlet control applied to the atomisers for other use cases. As such, improving stability characteristics of effervescent atomisers using high speed control, if successful, will improve the stability and spray quality of all effervescent atomisers in use, and is a promising avenue of further research.

Chapter 3

Experimental Setup

3.1 Method

The main method of testing used was high speed imaging. As mentioned in the review, the setup for this thesis uses an LaVision *HighSpeedStar* 6 CMOS camera, which can image at up to 5.4 kHz, with a sensor resolution of 1024 $\times$ 1024. The exposure time is dependent on imaging rate. The scene was backlit with a white LED panel. The nozzle itself is clamped into a steel testing rig designed to hold it securely for imaging. The testing rig has a rectangular cutout to allow for imaging of the internals of the nozzle. An example of the setup is shown here:

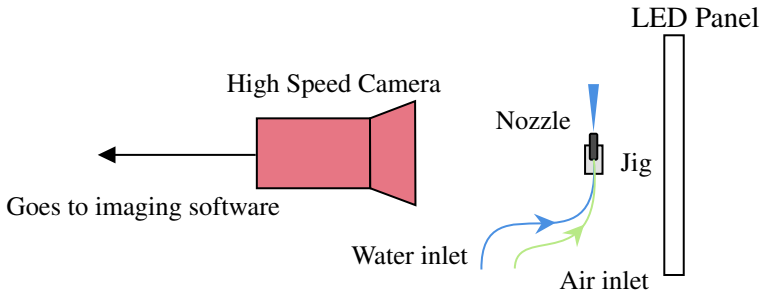

Figure 3.1: Experimental Setup

Air and water inlet lines are fed into the nozzle at a variety of flow rates and pressures. A wide range of testing conditions allows for comprehensive modelling of the inherent instabilities. A baseline for the nozzle was first established through high speed imaging under operation, without the usage of the solenoid.

3.2 Preliminary solenoid testing

In addition to testing the dominant frequencies within the atomiser nozzle, a test solenoid was also set up to explore the feasibility of high speed control. A circuit diagram of the setup is shown here:

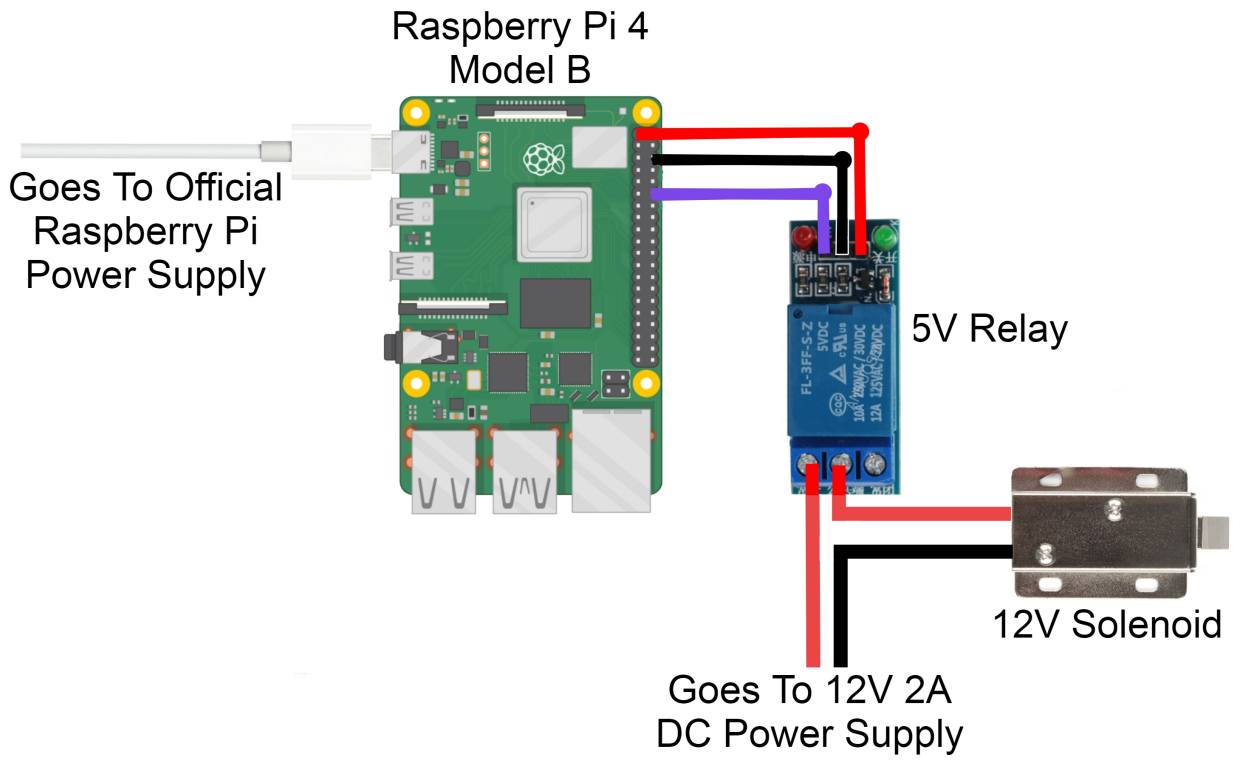

Figure 3.2: Solenoid setup circuit diagram

The components used here are as follows:

Table 3.1: Electrical component list

Item	Quantity
Raspberry Pi 4 Model B	1
RPi GPIO Breakout Board	1
12 V Solenoid	1
5 V Relay	1

The test solenoid used for this comparison is the '2W-025-08' normally closed 12V DC solenoid[1]. This solenoid has a response time of 40 ms, allowing control at up to 25 Hz. This solenoid is plumbed in directly into the water line, and will be controlled electronically over a SSH connection. For initial testing, the solenoid control is an open loop system, cycling at 20 Hz, although this will be further refined in future testing to incorporate closed loop feedback based on pressure and other measured characteristics. An image of the testing setup is shown here:

[1]Datasheet: https://naylampmechatronics.com/img/cms/Datasheets/2W-200-20%20AC220.pdf

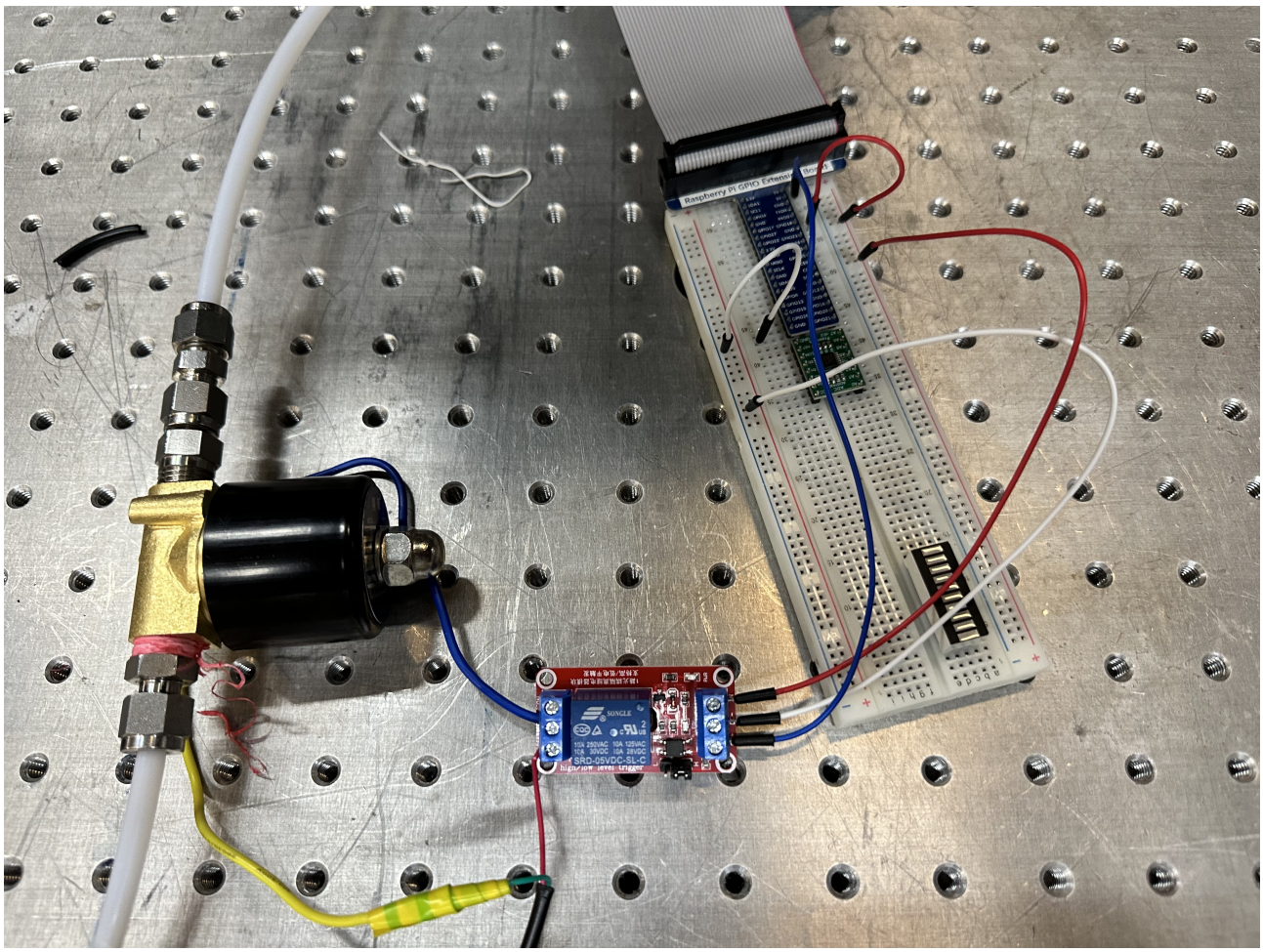

Figure 3.3: Experimental Setup

The final setup will replace this solenoid with a faster response time solenoid, or a voice coil actuator, for better control. The relay will also be replaced with a transistor for faster switching, as necessary.

3.3 Finalised solenoid setup

After confirmation of the experimental method (described in the sections below), the preliminary solenoid was replaced by a high speed springless poppet valve. Manufactured by Festo, the 'MHJ10-S-2,5-QS-4-MF' solenoid valve [2] has a switching frequency of up to 1000 Hz, and can operate at up to 6 bar. The valve comes with a trigger signal wire, removing the need for a relay, and as such, the solenoid will be directly connected to the GPIO pins from the Raspberry Pi. Power will be supplied by a variable voltage supply, providing at 24V and 2A of power. The code dictating the control setup of the Raspberry Pi is shown in **??**. A schematic of the final setup is shown here:

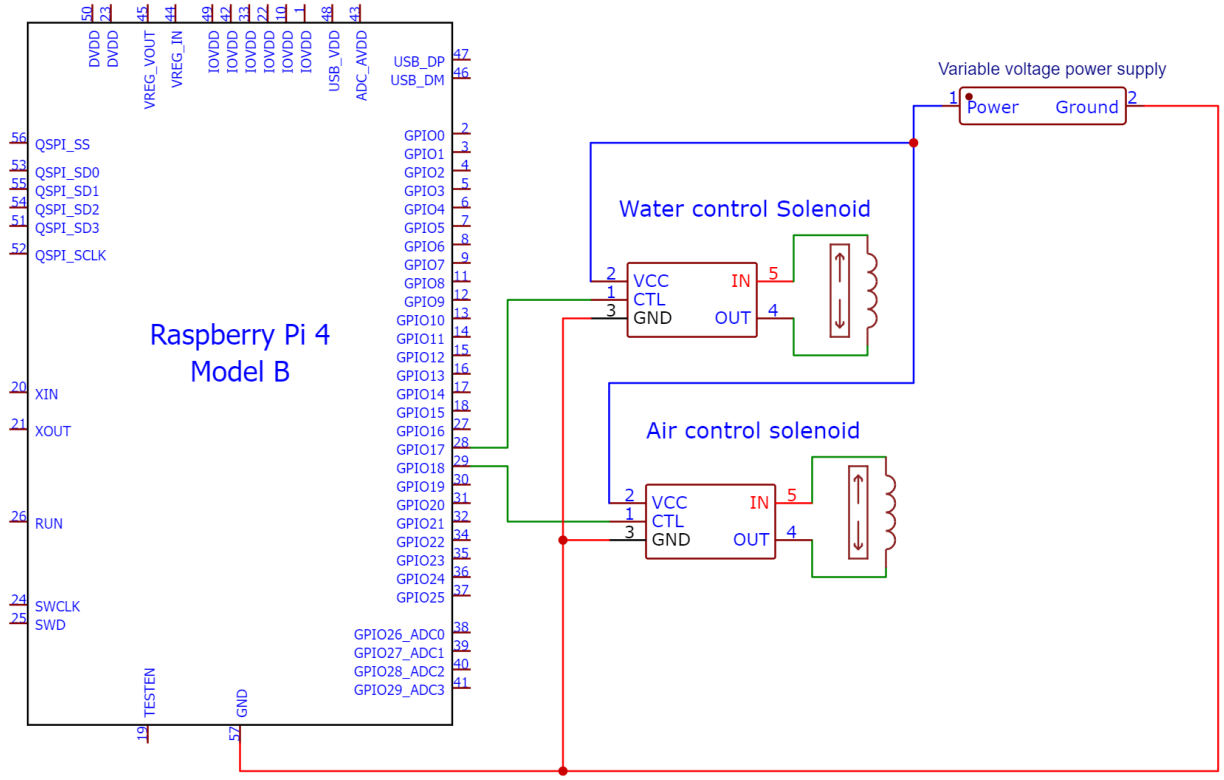

Figure 3.4: Schematic of finalised experimental setup

The components used are as follows:

Table 3.2: Finalised electrical component list

Item	Quantity
Raspberry Pi 4 Model B	1
RPi GPIO Breakout Board	1
Festo Solenoid	2
Variable power supply	1

[2] Datasheet: https://www.festo.com/tw/en/a/download-document/datasheet/565515

An image of the finalised setup is shown here:

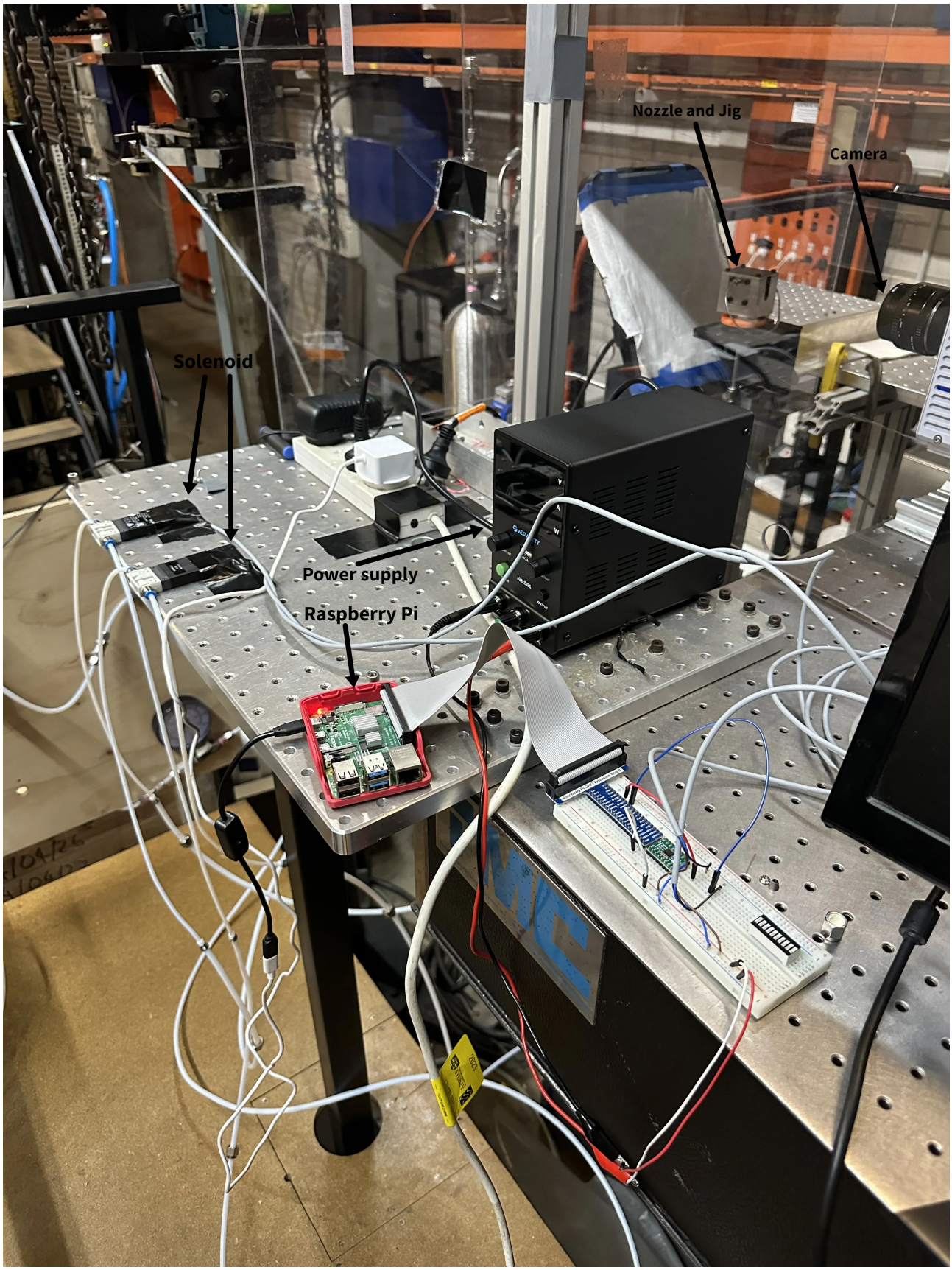

Figure 3.5: Finalised experimental setup

Chapter 4

Data Processing and Results

4.1 Preliminary image processing

Sample data was used to test the effectiveness of the image processing method and verify the control of instabilities. This sample data provided is also of an effervescent nozzle. However, it is an older design, and will only be used for method validation. High speed imaging of the internal flow within the atomiser was analysed to find the instability frequencies. A sample image from the set is shown in Figure 4.1:

(a) Sample full size image - rotated

(b) Sample cropped image

Figure 4.1: Sample of internal flow within nozzle

In this image, the nozzle outlet is towards the right, with gas being fed in from the left, and the liquid inlet being at the top. These images were then cropped to only consider the stepping chamber, which is the right hand portion. A sample of this is shown in the sub-figure (b) above.

To analyse the flow quality within the nozzle, the average intensity of this cropped image was calculated. As these are grey-scale images, this amounts to summing the brightness of each individual pixel, and dividing by the total number of pixels. A plot of this is shown in Figure 4.2

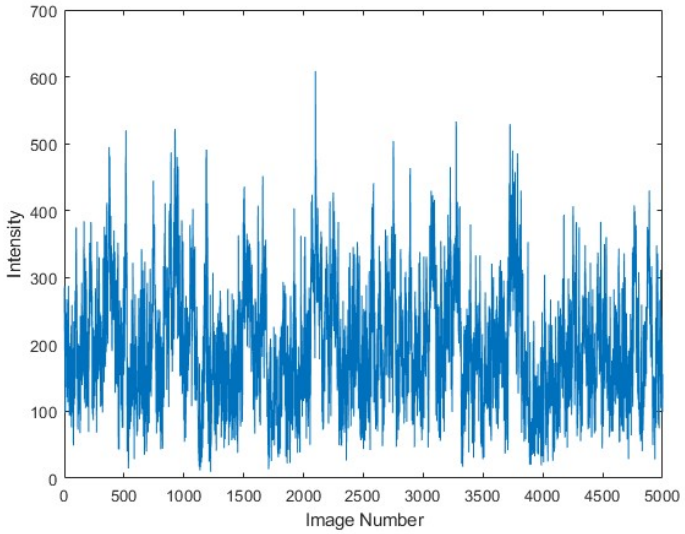

Figure 4.2: Intensity plot

To find the dominant frequencies of this instability, a Fourier analysis was carried out. These images are sampled at 10 000 Hz, which gives a period of 1×10^{-4} s. A discrete Fourier transform is applied to this sample in MATLAB, and the appropriate rescaling of axes implemented. This signal was then converted to a single sided spectrum for better readability. This gives the signal in the frequency domain as follows:

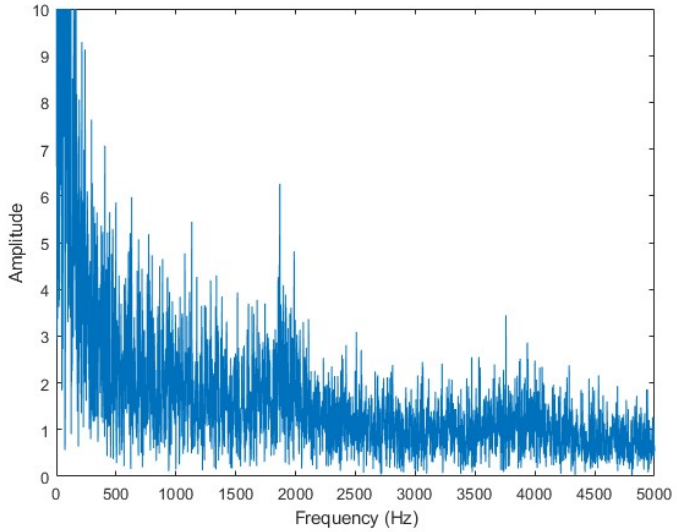

Figure 4.3: Single sided spectrum

As visible from this plot, the signal obtained is extremely noisy. Other methods, such as sliding window smoothing, were also tested to clean up this data, however none were successful. As such, the cropping rectangle was adjusted to look within the mixing chamber, instead of the exit orifice stepping chamber. In Figure 4.1, this is the bright area in the centre left. A different metric was also used for this analysis. Instead of calculating the mean intensity of an image, which is susceptible to

error with flow patterns, the image was instead binarised. The binarisation threshold selected was 500, but this will likely be refined better for better results. An example of the new process is shown here:

(a) Cropped sample - Section 2 (b) Binarised cropped sample

Figure 4.4: Second processing method

Once this image is binarised, the area fraction of light to dark pixels is then used as the mixing intensity metric. This produces significantly better results. Using the same Fourier Analysis technique as shown above supplies the following single sided spectrum.

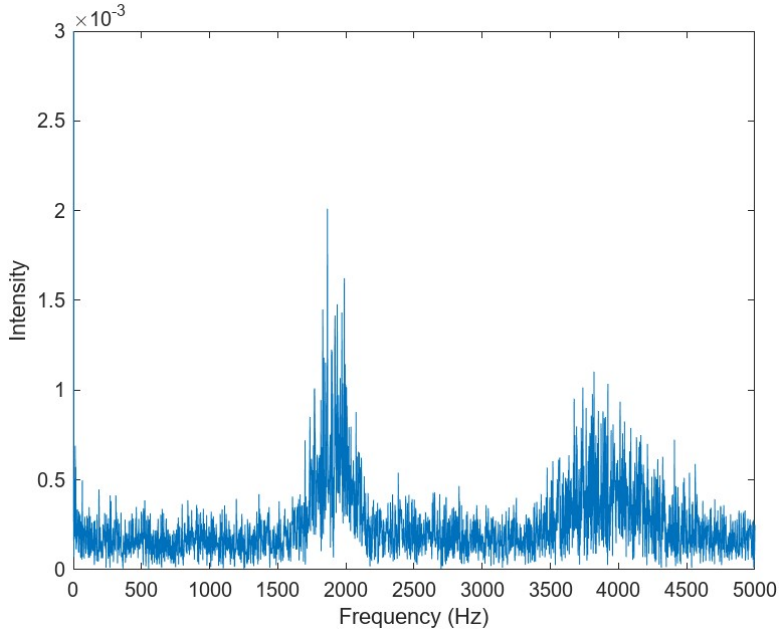

Figure 4.5: Single sided spectrum - method 2

As seen in Figure 4.5, the fluctuations tend towards a bimodal distribution, with the main peak at 1900-2000 Hz, as well as a lower, more spread peak at 3700-4100 Hz. This peak, however, may be a processing artefact due to noise in the signal. The signal was also smoothed to de-noise the resulting frequency-domain graph. This was done by convolving the transformed array with a constant function of the smoothing window size.

4.2 High speed imaging

With a working preliminary method for analysis of nozzle data, the nozzle can now be tested for dominant frequencies. A sample image is shown here, overlaid with the regions of interest analysed.

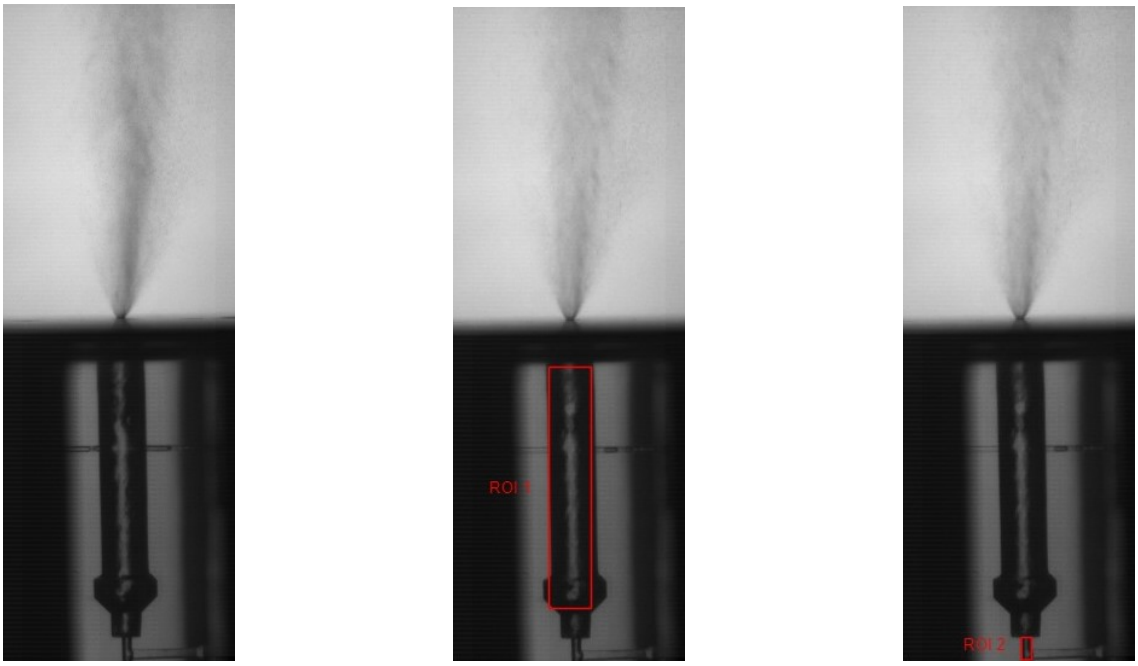

(a) Sample high speed image

(b) Sample high speed image - ROI 1 Highlighted

(c) Sample high speed image - ROI 2 Highlighted

Figure 4.6: Regions of interest - testing round 1

A sample analysis of these regions is shown here:

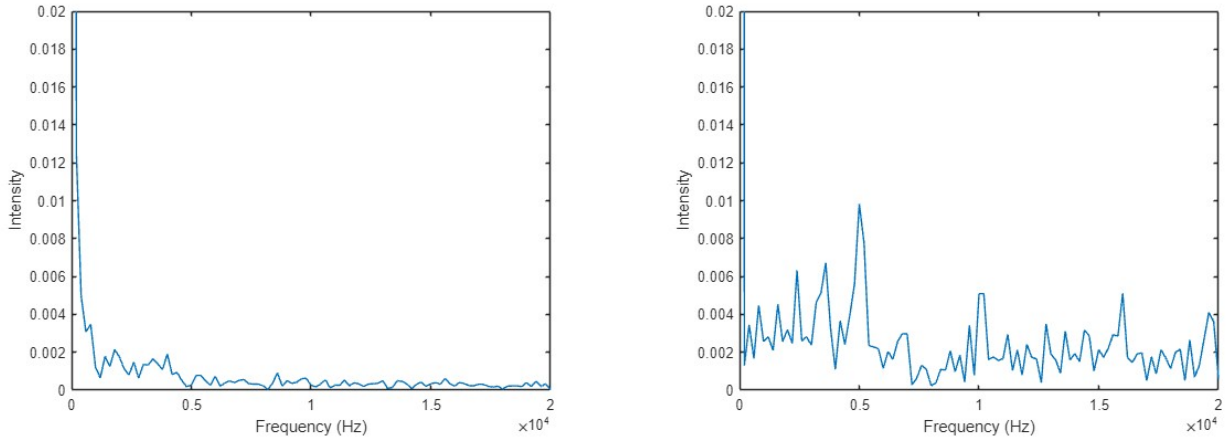

(a) Single Sided Spectrum - ROI 1

(b) Single Sided Spectrum - ROI 2

Figure 4.7: Single sided spectra - testing round 1

However, as shown here, neither of these regions of interest provided any dominant frequencies, though ROI 2 does show some peaking at 5000 Hz. This is likely due to the size of highlighted regions. As the only measure of intensity used is the amount of light within the regions of interest, having a large ROI is detrimental. This is due to the lack of spatial information available. For example, looking at ROI 1, if a bubble forms at the bottom of the region - the intersection area - the bubble

flow will increase the intensity of the surrounding area. But, as it passes through the mixing chamber, the overall intensity of the region does not change, thus losing information about the bubble passage frequency, a key indicator of instability modes. As a result, a selection of smaller ROI's was chosen, which are shown here.

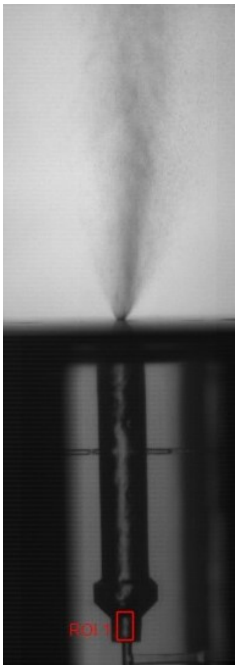

(a) Sample high speed image - new ROI 1 Highlighted

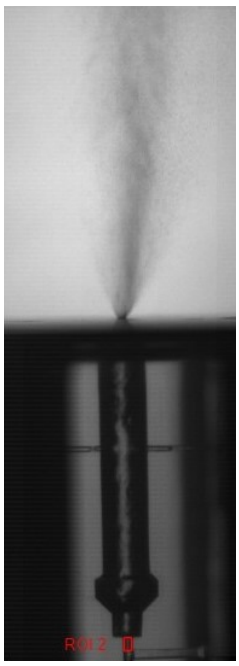

(b) Sample high speed image - new ROI 2 Highlighted

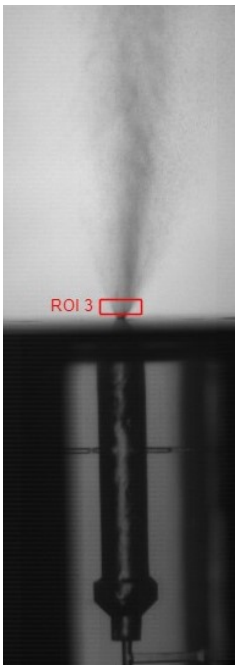

(c) Sample high speed image - new ROI 3 Highlighted

Figure 4.8: Regions of interest - testing round 1 reanalysis

ROI 1 was selected to contain a portion of the main mixing area before a converging section. This is due to the high degree of turbulent mixing in this area, which may lead to better approximation of the bubble frequency. ROI 2 was selected at the intersection of the air and water inlets, as this is the area where the instability begins. ROI 3 was selected just downstream of the nozzle exit to measure the instability in the spray as it exits to atmosphere. The results of image processing are shown here:

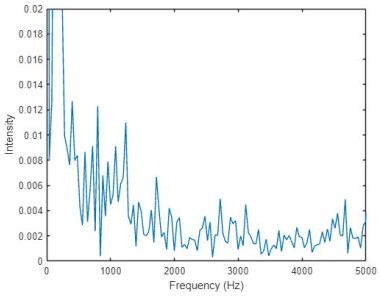

(a) Single Sided Spectrum - ROI 1

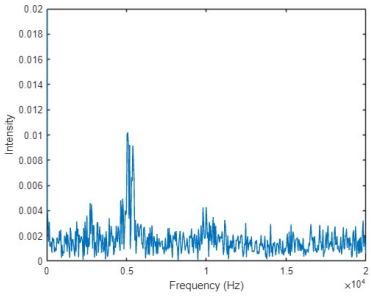

(b) Single Sided Spectrum - ROI 2

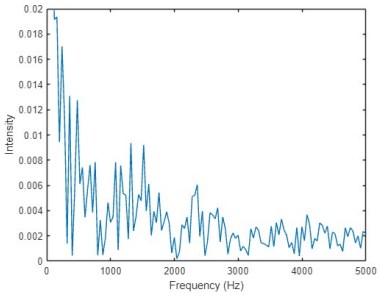

(c) Single Sided Spectrum - ROI 3

Figure 4.9: Single sided spectra - testing round 2

The results of this preliminary analysis show that ROI 2 is the most promising region to focus upon. Due to being close to the junction point, it has the most structure in the instabilities. This is further confirmed by the small nature of the region, allowing it to measure a single transient set of features within the flow.

4.3 Binarisation

4.3.1 MATLAB Implementation

The binarisation code is shown here. It was implemented in MATLAB, and utilises the inbuilt parallelisation available to improve performance.

```
...
%Initialisations
croprec = [83,504,6,40];  %Air water junction area - outlines the
    ROI
bthresh = 1400; %Binarisation threshold
fs=5000;   %Shooting frequency
imgfiles = dir(fullfile(readDir,'*.tif'));  %reads in all files
   from directory of TIF format
L = length(imgfiles);
...
%Filtering initialisation
sz = [croprec(4)+1,croprec(3)+1];
threshold_counter = zeros(sz);
se = strel('disk',50);  %Top hat filtering element
se2 = strel('disk',4); %Bottom hat filtering element
...
%Binarisation loop
parfor k = 1:L
    curImage = imread([readDir , imgfiles(k).name]);    %read in
       current image
    curImage_cropped = imcrop(curImage,croprec);    %Crop image

    %Filtering
    tophatcropped = curImage_cropped + imtophat(curImage_cropped,
       se);   %Adds top hat filter
    bothatcropped = tophatcropped - imbothat(curImage_cropped,se2
       ); %Subtracts bottom hat filter
    hmincropped = imhmin(bothatcropped,100);    %Applies h-minima
        filter
    hmaxcropped = imhmax(hmincropped,200);      %Applies h-maxima
        filter

    %Binarising
    imbi = zeros(size(hmaxcropped));    %iniatialise binarised
       matrix
    imbi(hmaxcropped>bthresh) = 1;     %binarise
    threshold_counter = threshold_counter + imbi;   %Cumulative
       threshold for optimsation

    intensityarray(k)=sum(imbi,'all')/numel(imbi);  %add up
       matrix (measure of image intensity)
end
```

As seen in the code above, various filters were applied to the input image to improve the quality of data acquired through binarisation. In order of application, these are described below:

Top Hat Filter: A top-hat filter is an advanced morphological image processing technique crucial for analyzing sprays in effervescent atomisation. It returns parts of the image larger than a defined structuring element and brighter than their surroundings. This is done through an opening operation, which involves two steps: erosion, which shrinks bright regions by removing pixels on their boundaries, followed by dilation, which expands the remaining regions. This process smooths the image and eliminates large, bright areas. The top-hat filter then subtracts this smoothed image from the original, leaving behind enhanced small, bright features like droplets.

This filter is used to remove large, roughly circular 'blobs' from the image. With the structuring element set to much larger than the average droplet size, this removes any ambient occlusions, or imaging artefacts.

Bottom Hat Filter: A bottom-hat filter is a morphological image processing technique essential for analyzing sprays in effervescent atomisation. It highlights small, dark features by returns parts of the image that are smaller than a defined structuring element and darker than their surroundings. This is achieved through a closing operation, which involves two steps: dilation, which expands dark regions by adding pixels to their boundaries, followed by erosion, which then shrinks these expanded regions. This process smooths the image and eliminates large, dark areas. The bottom-hat filter then subtracts the original image from this smoothed version, leaving behind enhanced small, dark features like voids or gaps within the spray. This results in clearer, more detailed images crucial for precise analysis of droplet characteristics, aiding in the optimization of atomisation processes.

In combination with the top hat filter, this filter produces an image with increased contrast, and elements between the sizes of the structuring elements of both filters.

H-minima Filter: The h-minima filter is a powerful tool used in image processing, particularly in the analysis of sprays in effervescent atomisation. It focuses on suppressing small local minima (valleys or depressions) in the image, making it invaluable for enhancing subtle features such as droplets in a spray.

This filter operates by suppressing any minima in the image that are shallower than a specified depth threshold, h. It achieves this by first identifying all the local minima in the image. Then, it compares the intensity of each minimum with its surrounding pixels. If the difference between the intensity of the minimum and its surroundings is less than h, the minimum is suppressed.

By selectively removing these shallow minima, the h-minima filter helps in enhancing the contrast and visibility of significant features like droplets while preserving the overall structure of the image. This enhanced image clarity facilitates accurate analysis of droplet size, distribution, and density, thus aiding in optimizing the efficiency of effervescent atomisation processes.

H-maxima Filter: The opposite of the h-minima filter. Removes shallow maxima.

The requirement of these filters for producing better quality data through binarisation was one of the motivations for the application of POD as an alternative analysis method.

The image is then binarised in line 28 by comparing each pixel to the threshold, setting to 1 if it exceeds, and 0 otherwise. Next, this binarised image is simply summed in line 30. As the size of each image within a dataset is consistent, this thus gives a measure of intensity in relation to the total image size.

4.3.2 Optimisation

The optimisation function described in Equation (2.9.0.3) was used for selecting the appropriate binarisation threshold for the images, as described above. The maximum intensity of any pixel in the region was found by comparing the maximum intensities in each image, and this was set as the max value to iterate up to.

A sample of the code used for optimisation is provided here.

```
1  ...
2  thresharray = 400:10:maxthresh;   %Set threshold range to iterate
       over
3
4  %Initialisations
5  satpix = zeros(size(thresharray));
6  hitpix = zeros(size(thresharray));
7  ...
8  for bthresh = thresharray
9      threshold_counter = zeros(sz);  %Counting matrix for number
           of times a pixel is binarised
10     ... %Binarisation loop is in here
11     satpix(count) = sum(threshold_counter == L,'all');  %Count
           number of saturated pixels
12     hitpix(count) = sum(threshold_counter < L & threshold_counter
           > 0,'all'); %Count number of hit but not saturated pixels
13 end
14 ...
15 %Clean satpix
16 satpix = satpix/max(satpix);     %Normalisation
17 satpix(isinf(satpix)) = 0;       %Clean edge cases
18
19 %Clean hitpix
20 hitpix = 1./hitpix;    % performs elementwise inverse
21 hitpix(isinf(hitpix)) = 0;  %Clean edge cases
22 hitpix = hitpix/max(hitpix);     %Normalisation
23
24 %Optimisation calculation and plotting
25 optfunc = satpix .* hitpix; %Elementwise product
26 optfunc(optfunc == 0) = max(optfunc);   %Clean edge cases
27 bar(thresharray,optfunc)     %Bar plot
28 ylim([0,1.5])
29 xlabel("Binarisation threshold")
30 ylabel("Optimisation funct value")
31 ...
```

The loop on lines 8-13 iterates over all the images in a given set at a range of threshold values, with each threshold value being tested in a loop hidden at line 10. Lines 11 and 12 populate *satpix* and *hitpix* respectively. The logical comparison operators are used for performance. Once appropriately populated, the data is normalised, and cleaned to produce reasonable results.

4.4 Proper orthogonal decomposition

Although producing results which were initially promising, the use of binarisation as an analytical method in the first rounds of testing highlighted a significant problem. The existence of multiple competing mechanisms within the nozzle - as described in Section 2.4 - has the effect of reducing the quality of the resultant Fourier spectra, due to the range in frequencies of these competing mechanisms. This is shown in spectra produced from the 8 April Test, displayed below:

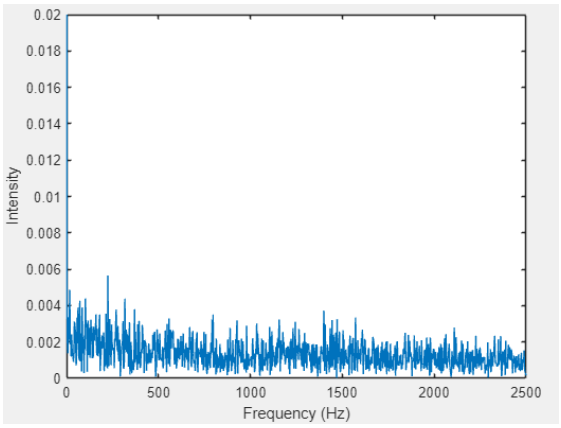

(a) 8 March test binarisation - ROI 1 Highlighted

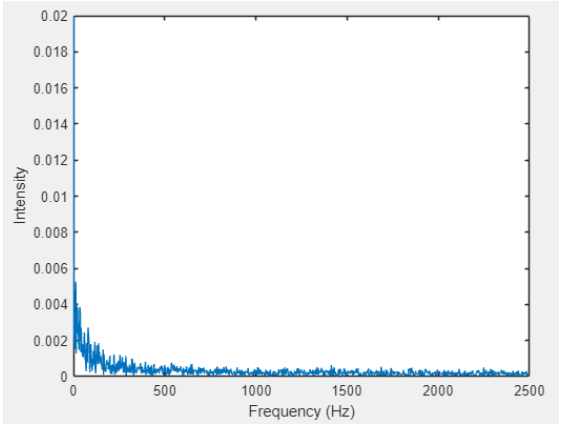

(b) 8 March test binarisation - ROI 2 Highlighted

Figure 4.10: Binarisation spectra example

As seen in Figure 4.10, the Fourier spectra produced from binarisation are not sufficient to provide any insights due to the inherent noise. Compare the variation between Figure 4.10b and Figure 4.9b - results produced under similar testing conditions - noting the large variation in spectra.

As a result of this, the technique of Proper Orthogonal Decomposition (described in further detail in Section 2.9.1) was used. In contrast with binarisation, POD allows the various mechanisms within the nozzle to be split into multiple 'dominant' modes. These modes can fluctuate independently, allowing for better characterisation of the instability within the nozzle. As a comparison, see below the POD results produced on the same datasets as Figure 4.10:

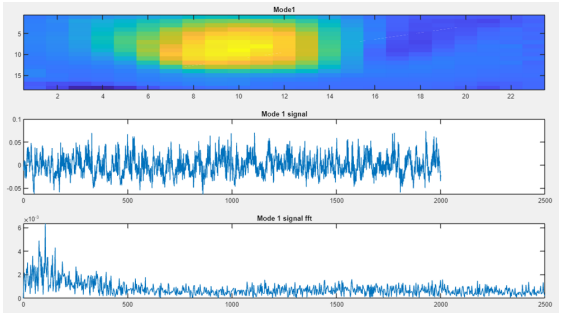

(a) 8 March test POD - ROI 1 Highlighted

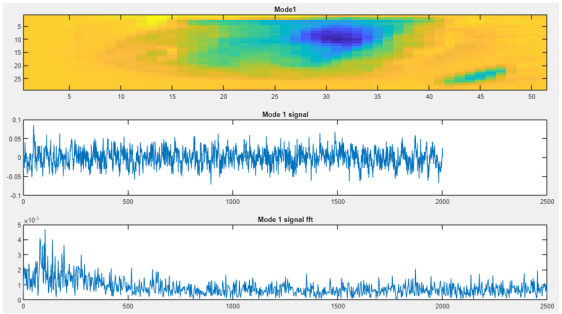

(b) 8 March test POD - ROI 2 Highlighted

Figure 4.11: POD spectra example

As seen above, the resulting spectra from the POD technique are much cleaner, with visible peaking in the 100-150 Hz range. Here, only the first mode is shown, as this mode captures $\sim 80\%$ of the energy available in the spectra. Higher order modes will also be analysed, as the interplay between internal mechanisms is of interest in characterising the instability within the nozzle.

4.4.1 MATLAB Implementation

An implementation of the above technique in MATLAB is shown here:

```
1  ...
2  %Initialisations
3  croprec = [83,504,6,40];  %Air water junction area - outlines the
       ROI
4  fs=5000;    %Shooting frequency
5  imgfiles = dir(fullfile(readDir,'*.tif'));  %reads in all files
       from directory of TIF format
6  L = length(imgfiles);
7  ...
8
9  Wmat = zeros(numel(cicrop),L);
10 parfor k = 1:L
11     %Read in image
12     curImage = imread([readDir , imgfiles(k).name]);     %read in
           current image
13     curImage_cropped = imcrop(curImage,croprec);     %Crop image
14     flatim = reshape(curImage_cropped,[],1);     %Flatten to one
           dimension
15     Wmat(:,k) = flatim; %Encode flattened image into correct
           column
16 end
17
18 horizmean = mean(Wmat,2);    %Calculates mean across each row -
       pixel mean in SVD
19 Wmat = Wmat - horizmean;     %Recenter using pixel mean - zero
       average
20
21 [U,S,V] = svd(Wmat,'econ','vector');     %SVD step
22
23 %Interpreting POD result
24 mode = 1 %Choose which POD mode to extract
25 modespace = reshape(U(:,mode),sz)';
26 modetime = V(:,mode);
27 [modefftP1,modefftfreq] = FFTsmooth(V(:,mode),1,fps);    %produce
       Fourier spectrogram
```

In the code above, lines 10-16 concatenate each input image in a dataset into a single matrix, as shown in Section 2.9.1. The decomposition step is done on line 21 using the inbuilt 'SVD' function in MATLAB. Interpreting the POD is then a matter of choosing the right column and row in the U and V matrices, respectively. The U matrix encodes the relative phase information within a mode, shown in the POD images displayed throughout this thesis as the top subplot. The V matrix encodes the time signal for modes throughout a dataset. By choosing the correct row, this can be analysed using an FFT in a similar way to the binarisation intensity output.

4.5 Image processing flow

Shown here is a flow chart of both image processing techniques used in this thesis. As visible, while easier to implement, binarisation is a more complex, and thus computationally inefficient, method. This, in conjunction with the output spectra quality, is why POD was chosen for analysis.

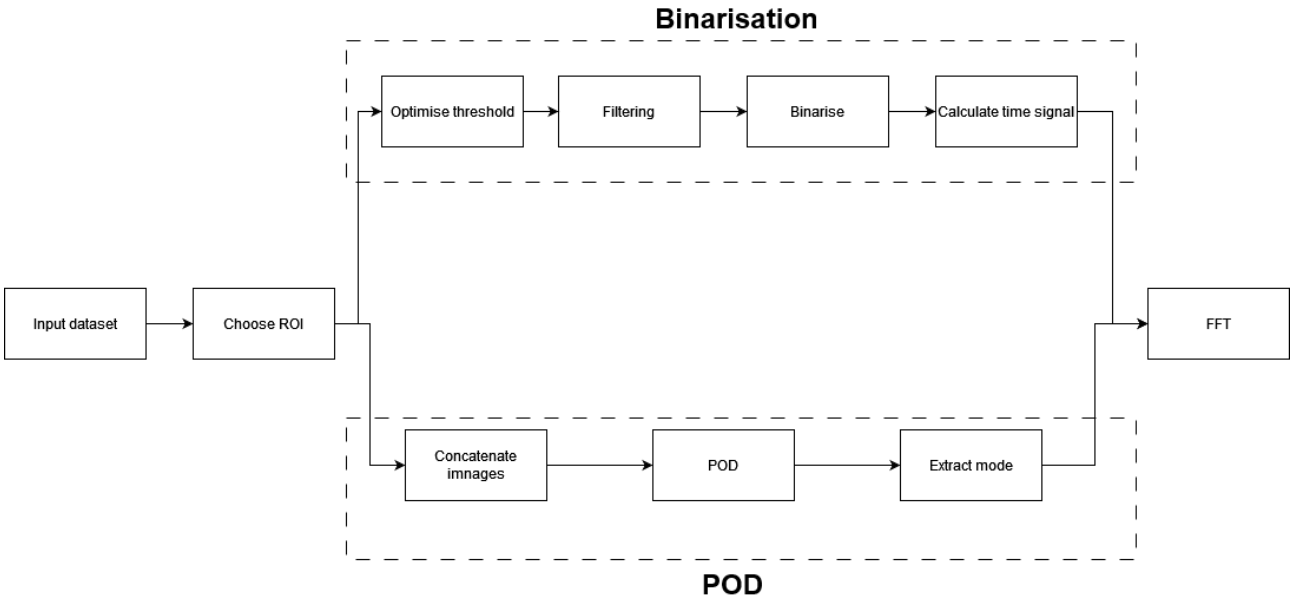

Figure 4.12: Image processing flow

4.6 Results and analysis

The aim of this section is to quantify the effects of high speed pulsing on the instability of the nozzle, with a view towards reducing the visible peaks in the 1500-2000 Hz range. The results given here show the potential for high speed control for improving the instability within effervescent nozzles, even at this preliminary stage. However, as will be shown by the analysis, significant further work remains to be done to fully mitigate these instabilities. As such, the results are quite varied, and the causes for some of these variations will be expanded upon in the below sections.

4.6.1 Spatial variation within the nozzle

The largest source of variation within the nozzle is spatial differences, as the flow moves from the inlet to the discharge orifice. For the final rounds of testing, four regions of interest were chosen. This will ensure a better characterisation of the flow as it moves through the nozzle. The ROI's coincide with the four main chambers within the nozzle. These are shown here:

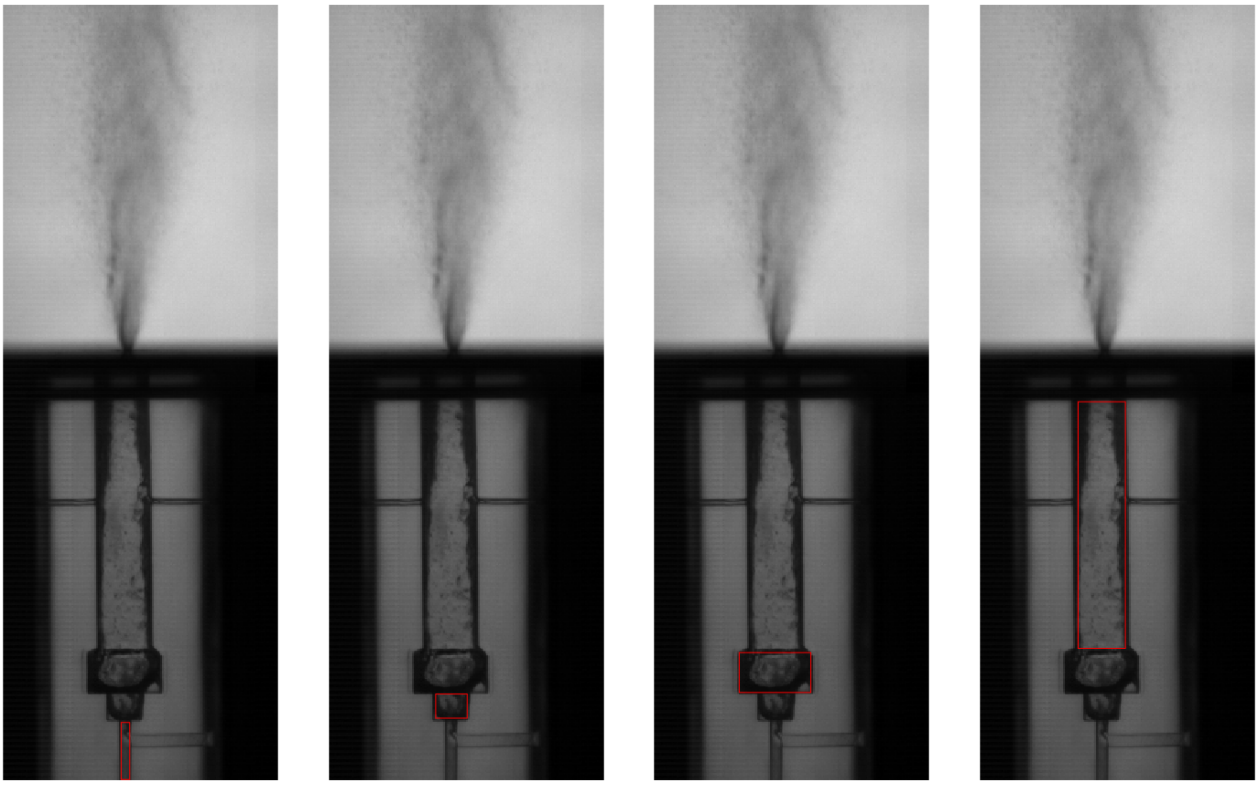

(a) ROI 1 - Air-Water Junction (b) ROI 2 - Mixing chamber (c) ROI 3 - Wide chamber (d) ROI 4 - Long chamber

Figure 4.13: Selected regions of interest

These regions were chosen to be able to better characterise how the instabilities vary as flow goes through a nozzle. As such, a short description of each chamber is shown here, in order from upstream to downstream.

Air-water Junction: This region focuses on the initial contact area where air and water mix, located at the entrance of the atomizer. Analyzing this area is crucial for characterizing the instability at the initial phase interaction point, where the primary mixing dynamics occur. Understanding how air and water mix initially can provide insights into the formation of instabilities that might affect the efficiency of atomisation.

Mixing chamber: This region, within the chamber where air and water continue to mix, is crucial for analyzing the development and evolution of instabilities within the nozzle. Observing how the phases interact and homogenize here helps in understanding the turbulence and flow patterns that contribute to instabilities, thereby providing essential data for optimizing the mixing chamber design to minimize these effects.

Wide chamber: Located in a wider section of the nozzle, this region is key for studying how instabilities propagate and stabilize before the flow reaches narrower sections. The flow behavior in this area can reveal important information about the mechanisms of droplet formation and the development of instabilities that influence the overall atomisation process.

Long chamber: This long section of the nozzle represents the final stage before the mixture is expelled as a spray. Analyzing this region is vital for understanding the culmination of instabilities that affect the final atomisation. It provides insights into how the spray characteristics, such as droplet size and distribution, are influenced by the instabilities within the nozzle, making it a critical area for optimizing nozzle design to achieve desired spray performance.

To better quantify these variations, shown below is the most dominant POD mode for each ROI. The solenoids were held open in these test cases, and thus no pulsing was utilised.

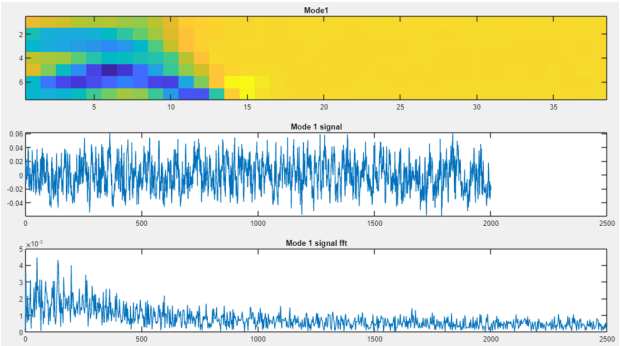

(a) ROI 1 - Air-Water Junction

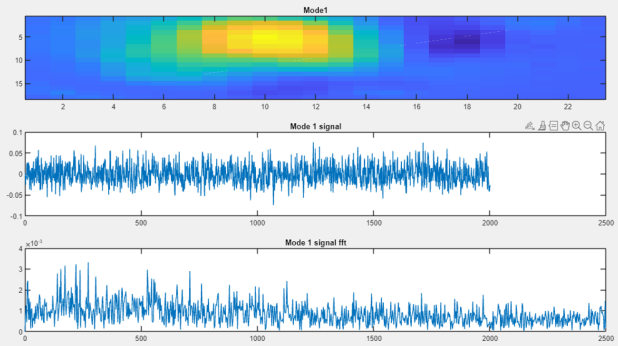

(b) ROI 2 - Mixing chamber

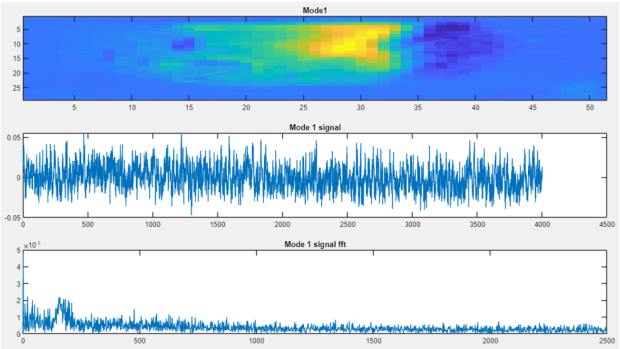

(c) ROI 3 - Wide chamber

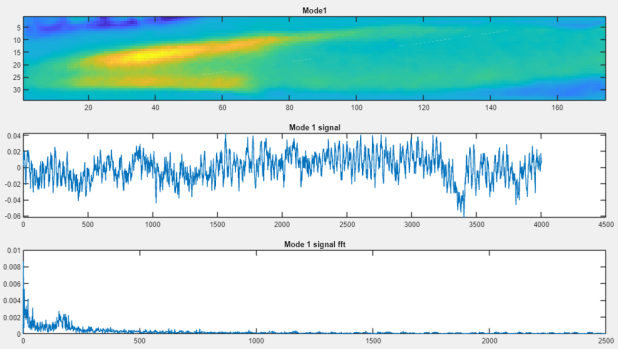

(d) ROI 4 - Long chamber

Figure 4.14: Spatial variation of instabilities - GLR = 0.06

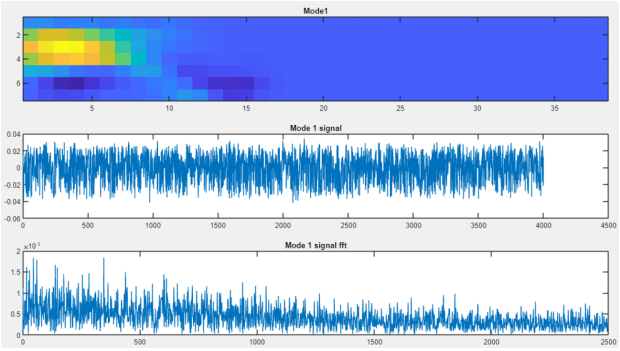

(a) ROI 1 - Air-Water Junction

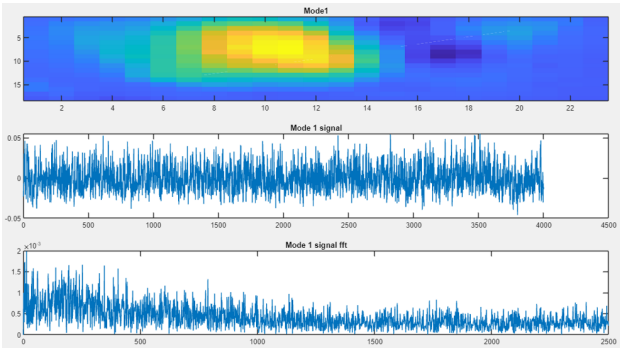

(b) ROI 2 - Mixing chamber

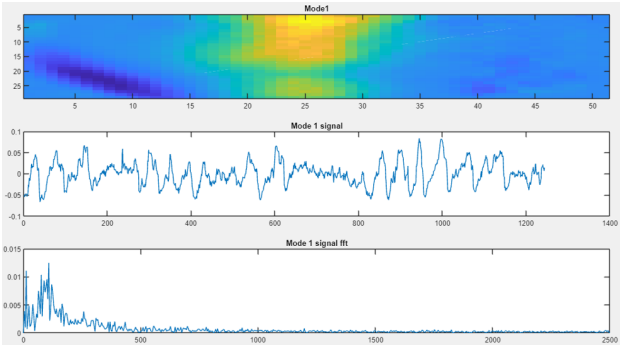

(c) ROI 3 - Wide chamber

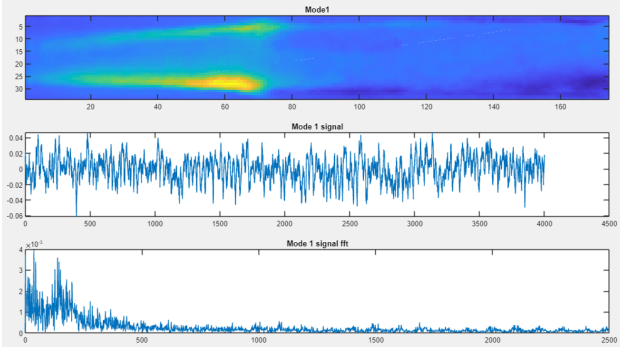

(d) ROI 4 - Long chamber

Figure 4.15: Spatial variation of instabilities - GLR = 0.10

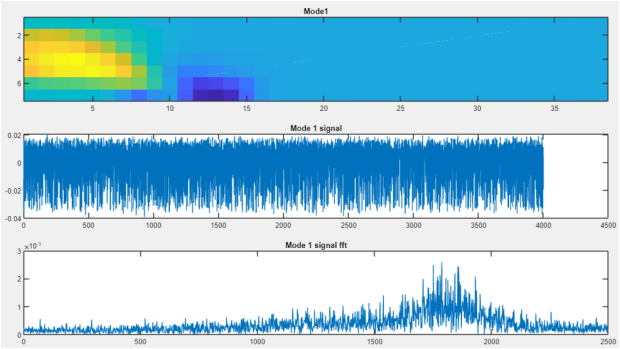

(a) ROI 1 - Air-Water Junction

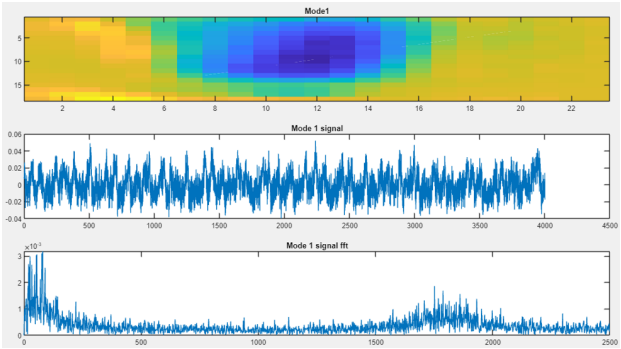

(b) ROI 2 - Mixing chamber

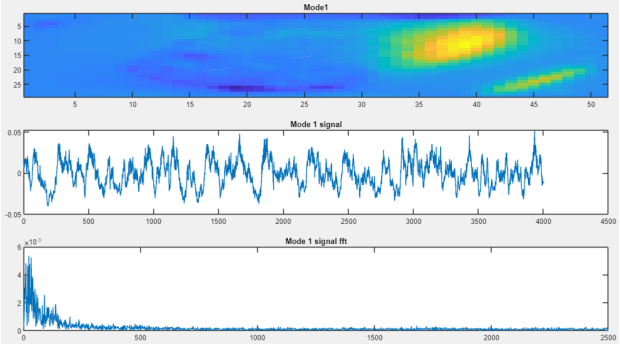

(c) ROI 3 - Wide chamber

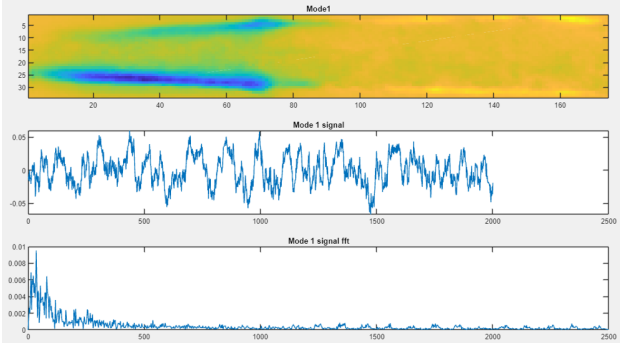

(d) ROI 4 - Long chamber

Figure 4.16: Spatial variation of instabilities - GLR = 0.40

The Fourier spectra across the different regions of interest within the nozzle provide critical insights into the behavior of instabilities and turbulence throughout the atomisation process. As seen by the decompositions above, ROI 1 and 2 consistently demonstrate higher frequency oscillations as compared to the further downstream regions - ROI 3 and 4.

In the air-water junction, the spectrogram reveals a broad range of frequencies with considerable intensity, indicating a high level of turbulence and complex mixing dynamics as air and water initially come into contact. This wide and intense frequency band is characteristic of significant turbulence and high-frequency fluctuations, underscoring the chaotic nature of the initial mixing phase. As the flow progresses to the mixing chamber, the spectrogram continues to display a broad frequency range. It is evident that while the intensity of the high-frequency fluctuations remains significant, there is an emergence of pronounced low-frequency components. This suggests that the mixing chamber experiences substantial turbulence and instability, similar to the initial air-water junction, but with a developing pattern of lower-frequency oscillations. These low-frequency peaks indicate that some of the initial high-frequency turbulence is transforming into more organized, lower-frequency flow structures. The presence of both high and low-frequency components signifies a complex interaction where the phases are mixing and stabilizing, yet still exhibiting significant instabilities.

In the wide chamber (ROI 3), the spectrogram begins to show a narrowing of the frequency band. Adjusted for scale, the intensity of high-frequency components remains significant, indicating that while some stabilization occurs, notable turbulence and instabilities persist. The presence of these high-frequency components, albeit in a narrower band, emphasizes the complexity of the flow dynamics. Additionally, this region may experience resonance effects, where specific frequencies are amplified due to the chamber's geometric dimensions, leading to sustained oscillations, while others are reduced. The wide chamber acts as a transitional zone where fluid inertia helps dampen some of the higher frequency instabilities, preparing the flow for further stabilization.

Finally, in the long chamber (ROI 4), the spectrogram shows a further narrowing of the frequency band, with significant energy still present but more confined to lower frequencies. This suggests a reduction in high-frequency instabilities, resulting in a more coherent flow. However, the persistence of lower-frequency turbulence indicates that the flow structures, while more stable, still exhibit notable instabilities. The more focused frequency band points to a shift towards more organized flow dynamics as the mixture prepares for final atomisation. Resonance within the long chamber can amplify certain lower-frequency oscillations, contributing to overall flow stability. Fluid inertia in this region also effectively damps higher frequency instabilities.

As such, the effects of instability across various GLR's and pulsing frequencies will be analysed at both ROI 1 and ROI 4, to better understand the instability throughout the course of the nozzle.

4.6.2 Effect of GLR on stability within the nozzle

As described in Section 2.6, GLR has a significant impact on the instability within a nozzle, with slug flow (GLR $\sim$ 0.1) expected to be the most unstable. To this effect, compare the decompositions for the Air-Water Junction and the Long chamber under different GLR's, as shown in Figure 4.14, Figure 4.15 and Figure 4.16, and collated here:

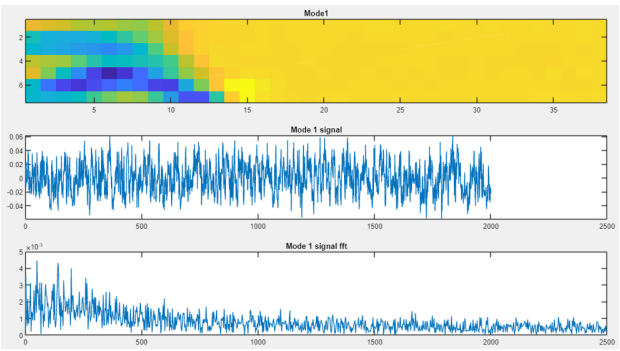

(a) Air-Water Junction - GLR = 0.06

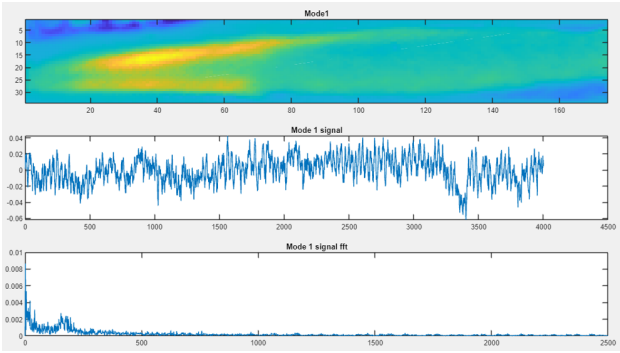

(b) Long chamber - GLR = 0.06

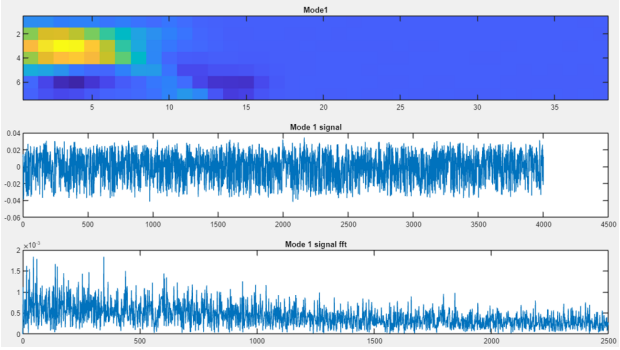

(c) Air-Water Junction - GLR = 0.10

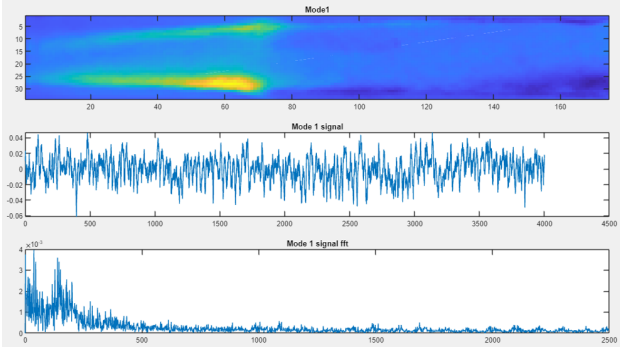

(d) Long chamber - GLR = 0.10

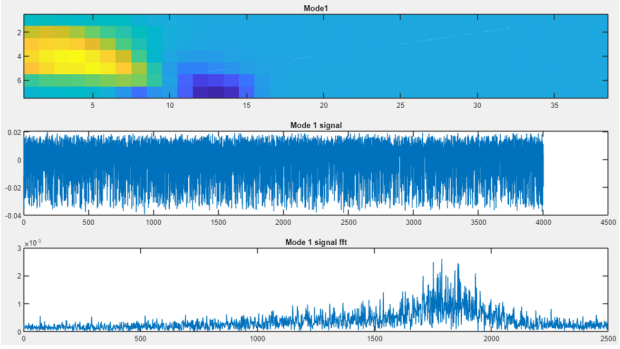

(e) Air-Water Junction - GLR = 0.40

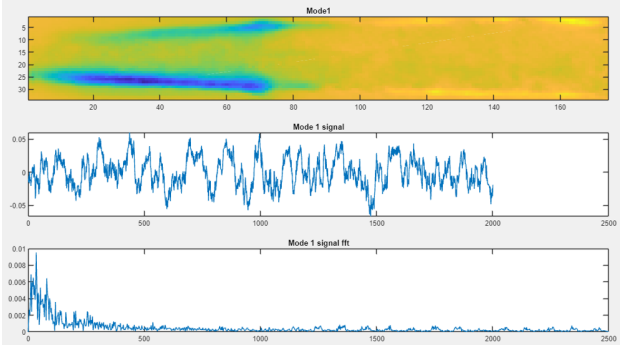

(f) Long chamber - GLR = 0.40

Figure 4.17: Effect of GLR on stability

As shown in Figure 4.17, the effect of Gas-Liquid Ratio (GLR) on the instability can be effectively seen through the Fourier spectra. Here, each row in the figure series corresponds to different GLRs, specifically 0.06, 0.10, and 0.40, for both the Air-Water Junction and the Long Chamber regions.

At a GLR of 0.06, the flow regime is typically characterized as bubbly flow. In this regime, the dispersed gas bubbles are relatively small and distributed within the liquid. The Fourier spectrum for the Air-Water Junction shows a broad range of frequencies with some low-frequency peaks, indicating instabilities due to interactions between the bubbles and the liquid. The Long Chamber region also corresponds with this, albeit with a slight increase in low-frequency components compared to the Air-Water Junction. This is indicative of the relatively stable nature of bubbly flow, where interactions -

while chaotic - have smaller overall effects due to the limits on bubble size.

As the GLR increases to 0.10, the flow regime transitions to slug flow. In this regime, larger gas slugs form and alternate with the liquid phase, leading to periodic oscillations. The Fourier spectrum for the Air-Water Junction at this GLR displays a broader range of frequencies, but with less pronounced low-frequency components, indicating a significant rise in instability due to the formation and collapse of these slugs. In contrast, the Long Chamber region shows a substantial increase in low-frequency components with pronounced peaks, indicative of the highest level of instability among the regions analyzed. The strong oscillations at specific frequencies highlight the pronounced instability characteristic of slug flow, where the periodic nature of gas and liquid slugs creates significant fluctuations in pressure and flow velocity. The existence of specific frequency peaks may also be related to the slug passage frequency, as described in Section 2.6.1.

At the highest GLR measured of 0.40, the flow regime has transitioned to annular flow. In this regime, the gas forms a continuous core surrounded by a liquid film. This leads to high levels of shear at the gas-liquid interface. Correspondingly, the spectrum for the Air-Water Junction reveals a significant increase in the range of frequencies, especially at higher frequencies, indicating a shift in the primary instability mechanism. This can be attributed to the high shear forces and the interactions at the gas-liquid interface, which create high speed turbulence within the flow. This region also displays strong low-frequency components, suggesting some persistence of bubble rupture driven instability. However, the intensity of these peaks is less than that observed at GLR 0.10, indicating a slight reduction in the level of instability this region at the highest GLR.

The intensity of the instabilities can also be quantified by analysing the spectral energy. In Figure 4.17, this amounts to the energy below the Fourier spectra in specific bands, as shown here:

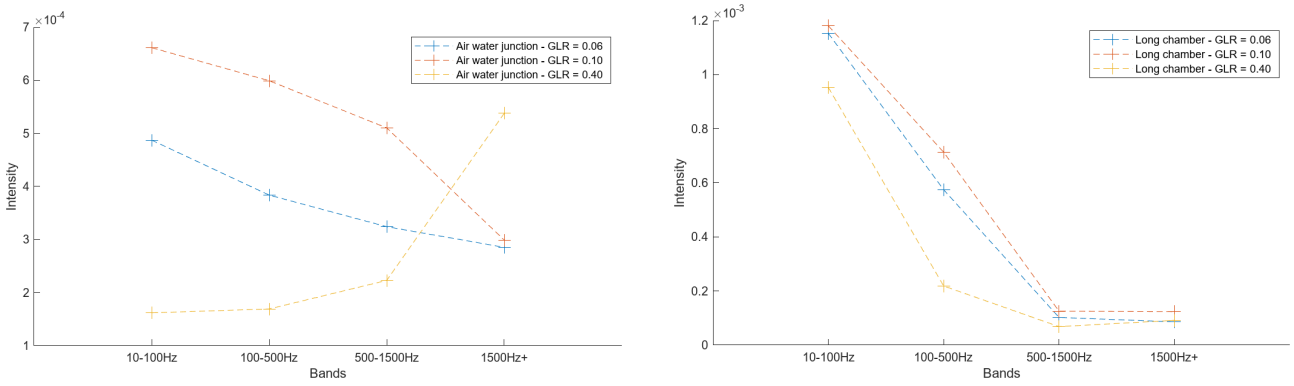

(a) ROI 1 - Air-Water Junction

(b) ROI 4 - Long chamber

Figure 4.18: Effect of GLR on spectral energy

For the above analysis, the spectra were split into four bands, as follows:

1. Low frequency: 10 - 100 Hz
2. Medium frequency: 100 - 500 Hz
3. High frequency: 500 - 1500 Hz
4. Very high frequency: 1500 Hz +

The spectral energy is then the integral of the Fourier spectra in these regions, normalised by the bandwidth to give consistent results. An intensity threshold was also chosen to reduce the impact of residual noise. This threshold was calculated as the maximum value of the spectra divided by e, giving a threshold approximately $\sim 36\%$ of the max intensity. The spectral energy data in various

bands further backs up the analysis provided above into the dynamic behavior of the nozzle under different flow regimes: bubbly, slug, and annular flows.

For the Air-Water Junction at a GLR of 0.06, the spectral energy is predominantly high in the 10-500 Hz band, as described above. This suggests that bubbly flow instabilities are mostly dominant at low-frequencies, due to the bubble rupture and coalescence. The higher energy in the 10-100 Hz band compared to higher frequencies indicates that the majority of the instability occurs at these lower frequencies, and here the bubble dynamics dominate.

At a GLR of 0.10, where the mixture transitions to slug flow, the spectral energy analysis reveals a significant rise in energy across all frequency bands, particularly in the 10-100 Hz and 100-500 Hz bands. This increase in energy likely corresponds to the formation and rupture of larger gas slugs, which induce strong local gas fraction variations. In contrast, at the highest GLR of 0.40, corresponding to annular flow, the spectral energy distribution shows a distinct shift. There is a notable increase in energy in the 1500 Hz+ band, indicating that the instabilities are now dominated by high-frequency oscillations. This shift can be attributed to the high shear forces and turbulence at the gas-liquid interface within the annular flow regime. The spectral energy in lower frequency bands (10-500 Hz) in turn diminishes, highlighting how bubble and slug interactions reduce their effects in this regime.

For the long chamber region, the spectral energy distribution follows a similar trend but with less distinct variation. At a GLR of 0.06, the spectral energy is highest in the 10-100 Hz band, agreeing with the characteristics of bubbly flow observed in the Air-Water Junction. As the GLR increases to 0.10, the spectral energy in the Long Chamber shows a substantial peak in the 10-100 Hz band, reflecting the heightened low-frequency instabilities due to slug flow. However, the energy in the 100-500 Hz band also remains significant, indicating that this region experiences a broader range of instabilities within this regime.

At GLR = 0.40, this region's spectral energy shows a marked decrease in the 100-500 Hz band compared to the Air-Water Junction, while the energy in 1500 Hz+ band increases slightly. This suggests that while annular flow instabilities are present, their manifestation in the Long Chamber is less intense compared to the Air-Water Junction, suggesting the flow becomes more stable nearer to the nozzle exit when at high GLR's. The distribution of energy across higher frequencies points to the dominance of shear-induced turbulence, though the overall instability is clearly somewhat dampened by the chamber's geometry and flow conditions. This collation of data also confirms that the slug regime (GLR = 0.10) is the most unstable, as this regime has the most energy under the instability analysis.

4.6.3 Effect of pulsing on stability within the nozzle

GLR = 0.10

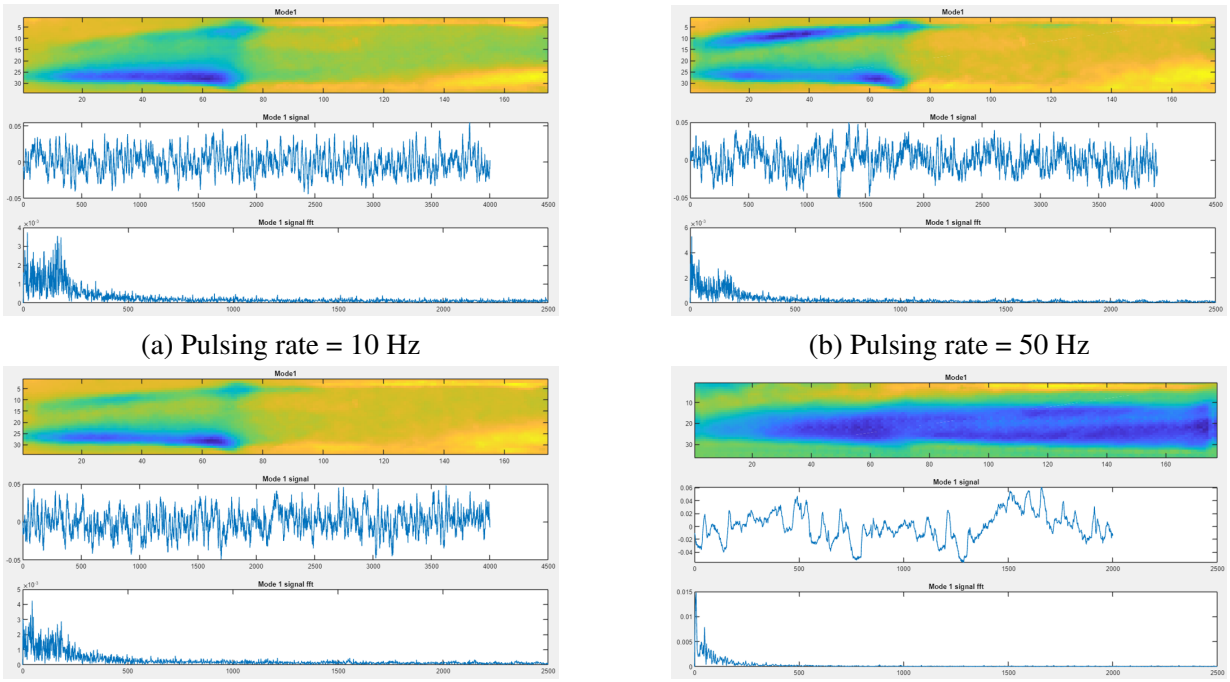

(a) Pulsing rate = 10 Hz

(b) Pulsing rate = 50 Hz

(c) Pulsing rate = 100 Hz

(d) Pulsing rate = 250 Hz

Figure 4.19: GLR = 0.10 , Long chamber

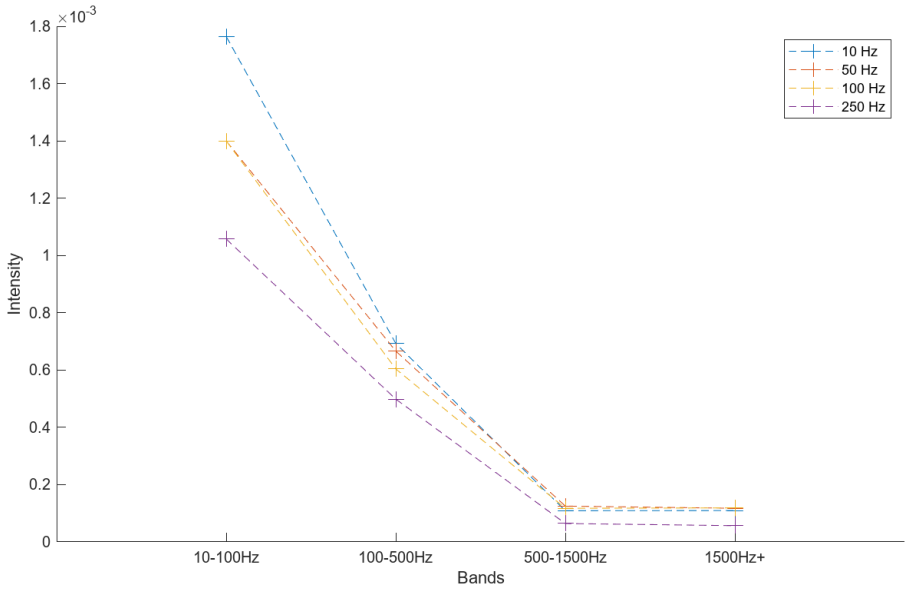

Figure 4.20: Pulsing rate vs banded spectral energy

The provided figures illustrate the impact of varying the pulsing rate on the instabilities within the effervescent nozzle. Figure 4.19 shows the Fourier spectra at different pulsing rates for a GLR of 0.10, while Figure 4.20 presents the collated spectral energy distribution across different frequency bands for each pulsing rate. Analyzing Figure 4.19, it is evident that the pulsing rate significantly affects the instability patterns within the nozzle. At a lower pulsing rate of 10 Hz (Figure 4.19a), the Fourier spectrum shows dominant peaks at lower frequencies, indicating a more unstable flow with

pronounced low-frequency oscillations. As the pulsing rate increases to 50 Hz (Figure 4.19b), the spectrum reveals a reduction in the intensity of lower frequency components.

When the pulsing rate is further increased to 100 Hz (Figure 4.19c), the spectrogram shows a further reduction in the prominence of lower frequency peaks, indicating a more stable flow regime. The highest pulsing rate of 250 Hz (Figure 4.19d) demonstrates the most significant shift, with the spectrum displaying minimal low-frequency oscillations, correlating with a much more stable flow.

Figure 4.20 quantifies these observations by plotting the spectral energy distribution across four frequency bands for each pulsing rate. The spectral energy is once again normalized by the bandwidth to provide a clear comparison. The plot demonstrates that as the pulsing rate increases, the spectral energy in the 10-100 Hz and 100-500 Hz bands decreases significantly, while the energy in the 500-1500 Hz and 1500 Hz+ bands remains relatively low and stable. This trend indicates that higher pulsing rates shift the instability characteristics towards a more stable flow regime, reducing the intensity of low-frequency oscillations. Specifically, at 10 Hz, the spectral energy is concentrated in the 10-100 Hz band, reflecting a more unstable flow. As the pulsing rate increases to 50 Hz and 100 Hz, the energy distribution shows a significant reduction in the 10-100 Hz band, indicating improved stability. At 250 Hz, the spectral energy in the lower frequency bands is much lower, highlighting the reduction of instabilities.

Relating these observations to the slug flow regime, the increase in pulsing rate may impact the behavior of the slugs within the nozzle. At lower pulsing rates, the slug passage frequency may be lower, resulting in larger and more pronounced slugs that contribute to significant low-frequency instabilities. As the pulsing rate increases, the slugs become smaller and more frequent, reducing the overall instability. Additionally, the stop-start action induced by the higher pulsing rate may increase internal turbulence within the nozzle, promoting better mixing and homogenization of the two-phase mixture. This enhanced turbulence disperses the phases more evenly, contributing to the observed stability at higher pulsing rates.

GLR = 0.40

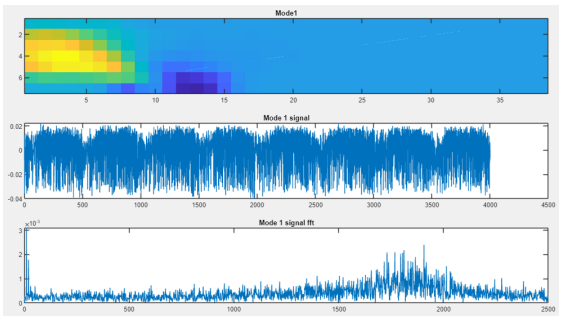

(a) Pulsing rate = 10 Hz

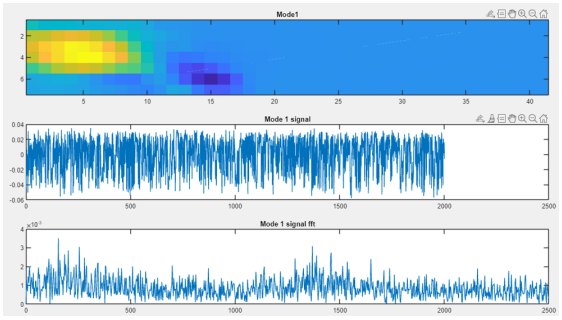

(b) Pulsing rate = 20 Hz

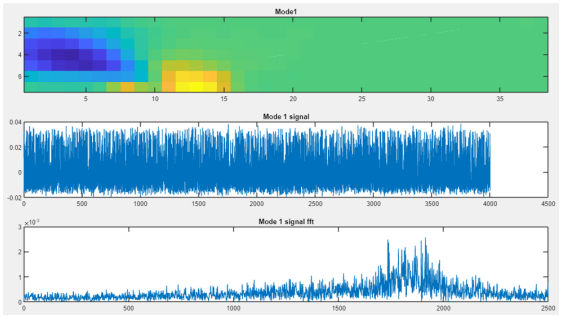

(c) Pulsing rate = 50 Hz

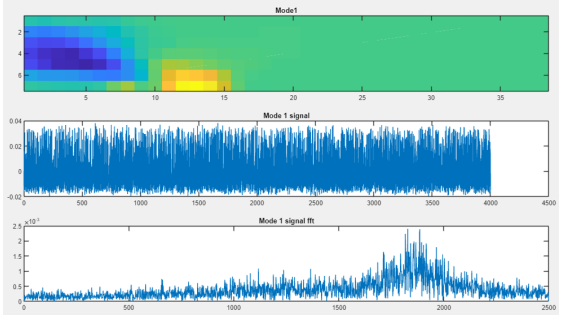

(d) Pulsing rate = 100 Hz

Figure 4.21: GLR = 0.40 , Air water junction

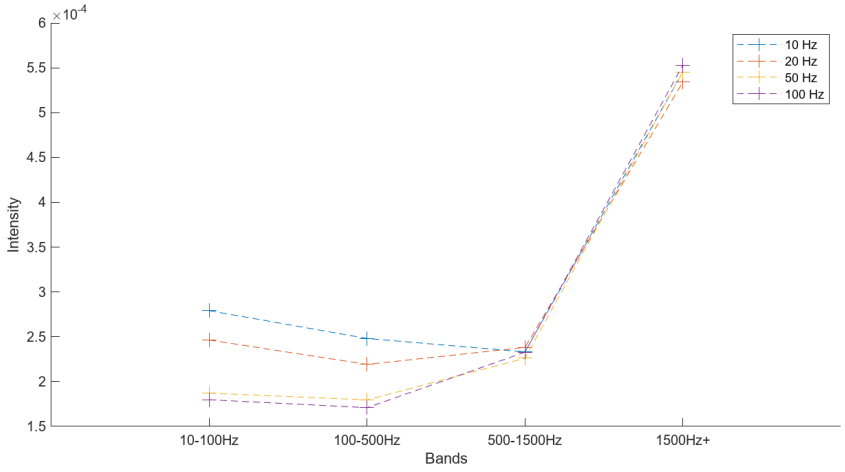

Figure 4.22: Pulsing rate vs banded spectral energy

In contrast with the effects in the slug regime, pulsation has insignificant impact on instabilities within the annular regime, as shown above. The spectral energy plot in Figure 4.22, shows that the majority of the energy is concentrated in the 1500+ Hz band, and is consistent across different pulsation frequencies. This concentration of energy in the high-frequency range suggests that the inherent instabilities in this regime predominantly occur at high frequencies. Despite varying the pulsing rates from 10 Hz to 100 Hz, the high-frequency instabilities remain largely unaffected, suggesting that the pulsing rates are insufficient in influencing the dominant frequencies.

The minimal effect of pulsing rates can be explained by the physical phenomena associated with two-phase mixtures in effervescent atomizers. The bubble rupture instability is mitigated somewhat, as shown by the reduction in spectral energy in the 10-100 Hz and 100-500 Hz bands , similar to the GLR = 0.10 case considered above. However, faster instabilities, such as those driven by the gas-liquid interface shear, are unreachable by the current solenoid, as described further in Section 4.7.2.

GLR = 0.06

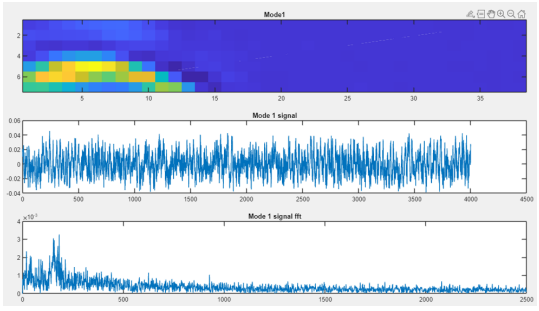

(a) Pulsing rate = 10 Hz

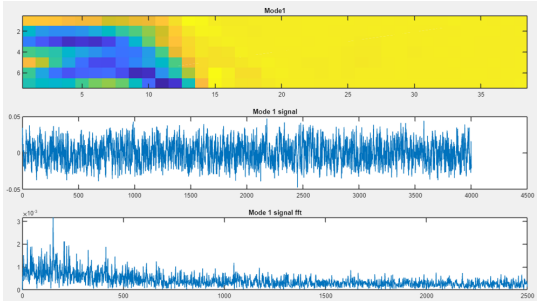

(b) Pulsing rate = 50 Hz

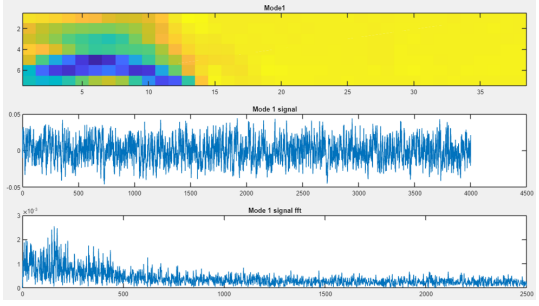

(c) Pulsing rate = 100 Hz

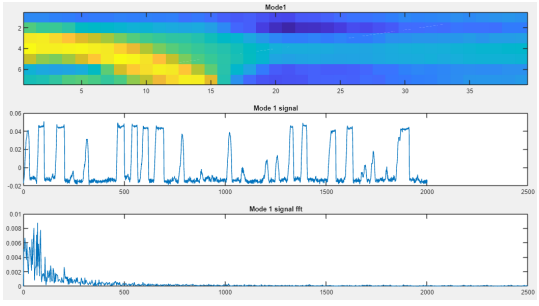

(d) Pulsing rate = 250 Hz

Figure 4.23: GLR = 0.10 , Long chamber

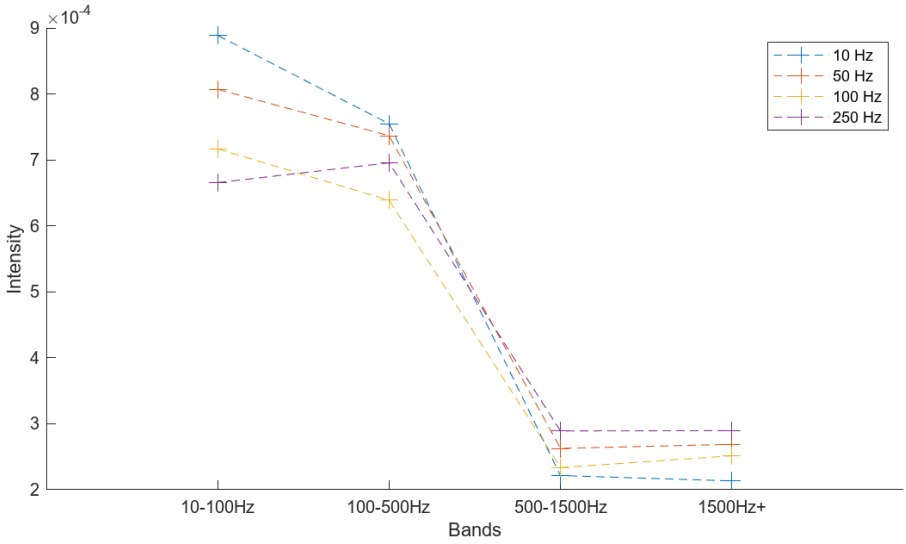

Figure 4.24: Pulsing rate vs banded spectral energy

The analysis of the GLR = 0.06 case, shown in the figure, reveals that the effect of pulsing rate on the stability of the nozzle is present but not as pronounced as in other flow regimes. At a GLR of 0.06, the flow regime is characterized by bubbly flow, where small gas bubbles are dispersed within the liquid. The Fourier spectra at the bottom of each subplot indicate that as the pulsing rate increases from 10 Hz to 250 Hz, the intensity of the low-frequency components decreases, suggesting a reduction in large-scale instabilities. The spectral energy vs. pulsing rate plot further supports this observation, showing a more gradual decline in intensity across the frequency bands with increasing pulsing rates.

This reduced sensitivity to pulsing rate can be attributed to the nature of the bubbly flow regime. In bubbly flow, the gas bubbles are smaller and more evenly distributed within the liquid, leading to inherently more stable flow characteristics. As the pulsing rate increases, the bubbles may break down into even smaller sizes, promoting further homogenization. However, the initial stability of the bubbly flow limits the extent of improvement achievable through increased pulsing.

The physical mechanism behind this can be understood by considering the interaction between the dispersed gas bubbles and the liquid. At lower pulsing rates, the bubbles form and coalesce more irregularly, leading to fluctuations and instabilities within the nozzle. As the pulsing rate increases, the formation of bubbles becomes more frequent, resulting in smaller and more uniformly distributed bubbles. This uniformity reduces the amplitude of fluctuations and enhances the stability of the flow.

4.7 Future work

4.7.1 Reproducibility of results

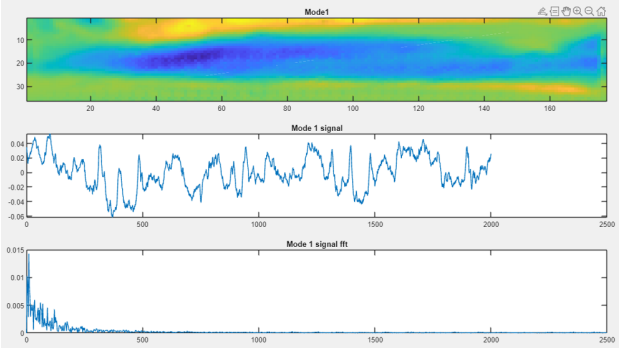

(a) 8 April

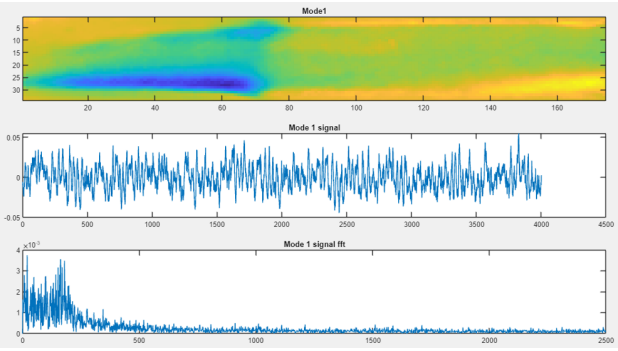

(b) 5 May

Figure 4.25: GLR = 0.10 , Pulsing rate = 10Hz

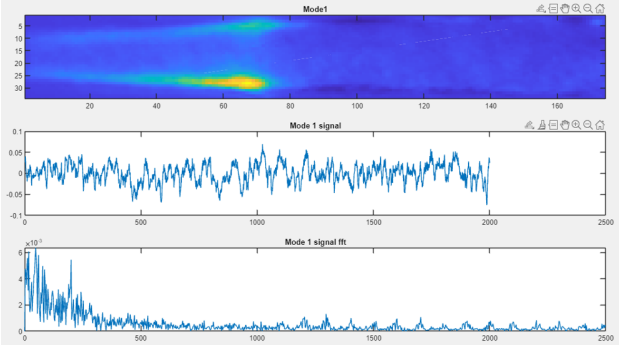

(a) 8 April

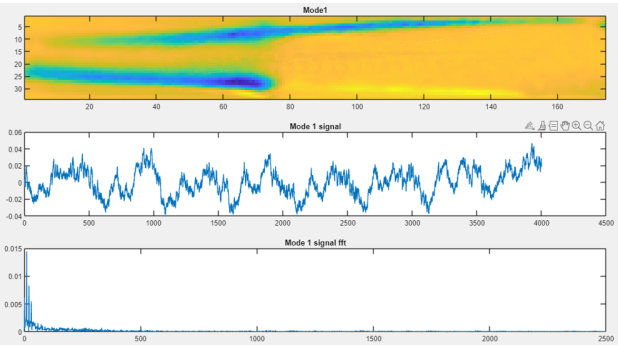

(b) 5 May

Figure 4.26: GLR = 0.40 , Pulsing rate = 20Hz

Figure 4.25 and Figure 4.26 illustrate a major setback encountered during testing: the reproducibility of results. Despite maintaining identical operating conditions across different testing days, significant variations were observed in the Fourier spectra, indicating changes in instability behavior within the effervescent nozzle. Each row in the images represents tests conducted under the same conditions but on different days.

The observed variations may be attributed to several factors. Firstly, fluctuations in ambient temperature, humidity, or pressure can significantly affect the behavior of the two phase flow within the nozzle. Even slight changes in these conditions can lead to variations in flow regimes and instability characteristics. As such, ensuring consistent experimental conditions is critical. Variations in the gas and liquid flow rates, nozzle geometry, and pulsing rate, even if minor, can influence the stability and performance of the nozzle. More stringent control and monitoring of these parameters are essential to minimize variability.

Measurement and instrumentation variability can also contribute to discrepancies in the recorded data. Differences in camera positioning, exposure timing, or even fluctuations of the brightness in panel lighting can all lead to variations. Additionally, the physical condition of the nozzle could impact flow dynamics. Wear and tear or slight alterations in the nozzle structure over time can affect performance. A notable problem was the existence of liquid droplets on the surface of the nozzle exit, which was solved by drying the nozzle periodically between each test run.

To address these reproducibility issues, several steps can be taken. Implementing controlled environments where temperature, humidity, and pressure are kept constant can reduce variability due to ambient conditions, although this is difficult to accomplish in the current testing environment. Developing and strictly adhering to standardized procedures for setting up and conducting experiments can minimize discrepancies in experimental conditions. Ensuring all measurement instruments are regularly calibrated and the nozzle is maintained in optimal condition will also reduce measurement variability and physical discrepancies. Recording all relevant environmental and operational parameters during each test could help identify and account for sources of variability, facilitating more accurate comparisons across different testing days if correctly accounted for.

4.7.2 Improvements to the experimental method

Another notable limitation encountered during the testing was the maximum switching frequency of the solenoid used in the effervescent nozzle setup. Although the *Festo* high speed solenoid was listed as being capable of switching at frequencies up to 500 Hz, in practice, it was only observed to operate reliably up to 250 Hz. This discrepancy between the specified and actual performance of the solenoid introduced constraints on the range of operating conditions that could be tested.

It was observed during testing that at high switching frequencies such as 250 Hz, due to the design and internals of this particular solenoid, the lines remained open for more time than they were closed. This biased open state certainly affected the flow dynamics, as the nozzle spends more time allowing fluid to pass through, which can influence the development and nature of instabilities within the nozzle. In addition, due to the biased state of the solenoid, any asynchronicity between the gas and liquid control solenoids could lead to aliasing, with the output pulsation frequency at the nozzle entrance potentially different to the control frequency sent to the solenoid.

Furthermore, the solenoid's inability to reach higher frequencies meant that certain high-frequency instabilities, which could be critical for understanding the full range of nozzle behavior, were not able to be tested for mitigation. The upper limit of 250 Hz for reliable switching restricted the investigation to lower frequency oscillations and may have skewed the characterization towards flow regimes that occur at these lower frequencies.

To mitigate these limitations and enhance the experimental setup, it would be beneficial to explore alternative solenoid options that can reliably achieve higher switching frequencies. Additionally, understanding the solenoid's operational characteristics in greater detail, such as its response time and duty cycle at different frequencies, could help in designing more accurate and reliable experiments.

Additionally, the current experimental setup operates under an open loop control system, where the gas and liquid flow rates are set manually and remain constant throughout the testing process. While this method is straightforward and allows for precise initial settings, it lacks the ability to adapt to real-time changes within the system. This limitation can lead to inconsistencies and reduced accuracy in capturing the complex dynamics of the effervescent nozzle, particularly under varying ambient conditions or fluctuations within the flow itself.

Implementing a closed loop control system could significantly enhance the performance and reliability of the experimental setup. Closed loop control involves continuously monitoring the system's output and making real-time adjustments to the input variables to maintain desired operating conditions. For the effervescent nozzle, this would mean dynamically adjusting the gas and liquid pulsation rates based on feedback from sensors that measure parameters such as pressure, flow rate, and droplet size distribution.

One potential method for implementing closed loop control is by utilizing high-speed imaging to gather real-time data on the nozzle's output. The high-speed camera used is able to capture detailed

images of the spray pattern and droplet formation at frame rates sufficient to observe rapid changes in the flow dynamics. This information can then be processed to identify key characteristics of the atomisation process, such as droplet size distribution, spray cone angle, and flow regime transitions. By analyzing this data, the control system can make precise adjustments to the gas and liquid flow rates to maintain optimal operating conditions.

To achieve effective closed loop control using high-speed imaging, the control electronics must be capable of processing data and making adjustments at extremely high speeds. The system would need to close the loop at frequencies between 1500-2000 Hz to keep up with the rapid changes in the flow dynamics observed in the high-speed images. This requires advanced control algorithms and high-performance hardware capable of real-time data processing and actuator response.

One of the primary benefits of a closed loop system is its ability to maintain stability and consistency in the face of disturbances. For example, variations in ambient temperature and pressure can affect the behavior of the gas-liquid mixture within the nozzle. With closed loop control, these variations can be detected and compensated for in real time, ensuring that the nozzle operates within optimal parameters regardless of external conditions. This adaptability would lead to more reproducible and reliable results, enhancing the overall quality of the experimental data.

Furthermore, closed loop control can optimize the atomisation process by continually fine-tuning the gas-to-liquid ratio (GLR) and pulsing frequency. By monitoring the nozzle's output, the system can identify the optimal operating points that minimize instabilities and promote uniform droplet formation. This would not only improve the efficiency and effectiveness of the atomisation process but also provide deeper insights into the underlying physics of two-phase flow within the nozzle. Advanced control algorithms could be employed to predict and respond to changes in the flow regime, such as the transition from bubbly to slug flow, further refining the control strategy.

Additionally, the integration of closed loop control could facilitate more complex experimental designs, such as controlled perturbations to study transient behaviors and dynamic responses of the nozzle. This capability would open new avenues for research, allowing for a more comprehensive understanding of the factors influencing nozzle performance and stability.

Chapter 5

Conclusion

The investigation into the effects of open-loop control, specifically through the pulsation of gas and liquid inlet lines, on instabilities within an effervescent atomizer has provided significant insights. Effervescent atomizers are critical in various industrial applications due to their ability to produce fine sprays from various liquids. However, the inherent instability within the nozzle can lead to inefficiencies in atomisation quality. This study aimed to address these challenges by exploring the potential of pulsation control to enhance flow stability. From existing research, it was evident that the instability mechanisms in effervescent atomisation are influenced by factors such as the gas-to-liquid mass flow ratio (GLR), injection pressure, and flow regimes. Previous studies highlighted that the primary and secondary atomisation processes are significantly affected by the presence of large gas bubbles, which disrupt the homogeneity of the spray. The literature also emphasized the importance of achieving a stable gas-liquid mixture to optimize atomisation performance.

In this context, the experimental results demonstrated that pulsation rates have a notable impact on the stability of the flow within the atomizer. Lower pulsing rates resulted in larger and more irregularly distributed gas bubbles, contributing to greater flow instability. Conversely, higher pulsing rates led to a more homogenized mixture and enhanced flow stability. This finding aligns with the observations from the literature, which suggested that reducing bubble size can mitigate instability. The analysis further revealed that the initial flow regime plays a crucial role in determining the effectiveness of pulsation. In bubbly flow regimes, characterized by small and evenly distributed gas bubbles, the stability improvements due to pulsation were limited. However, in flow regimes with larger gas bubbles, increased pulsing rates significantly reduced instabilities, as evidenced by the reduction in the amplitude of fluctuations within the nozzle. This supports the theoretical understanding that the gas volume fraction and bubble dynamics are key factors influencing spray stability.

Despite the promising findings, the study also identified challenges in the reproducibility of results, largely due to variations in ambient conditions and experimental setup inconsistencies. Addressing these issues will be critical for future research to ensure more reliable and consistent data. Improvements to the experimental method, such as enhanced control of environmental parameters and more precise measurement techniques, will be necessary to validate and extend the current findings.

In conclusion, the application of open-loop control has the potential to mitigate instabilities within effervescent atomizers, particularly in the slug flow regime. The study's results contribute to a deeper understanding of the interplay between pulsation rates and flow stability, building on the existing literature's insights into atomisation mechanisms and instability factors. Future work should focus on improving the reproducibility of results and further refining the pulsation techniques to optimize the stability of the atomisation process under various operating conditions. By addressing these challenges, the findings of this research can be effectively translated into practical applications, enhancing the efficiency and reliability of effervescent atomizers in industrial settings.

Bibliography

[1] A. H. Lefebvre and V. G. McDonell, *Atomization and Sprays*. Boca Raton: CRC Press, 2017. DOI: 10.1201/9781315120911.

[2] M. Lightfoot, "Fundamental classification of atomization processes," *Atomization and Sprays*, vol. 19, no. 11, 2009.

[3] N. Chigier and R. Reitz, "Regimes of jet breakup and breakup mechanisms (physical aspects)," *Recent Advances in Spray Combustion: Spray Atomization and Drop Burning Phenomena*, 1995. DOI: 10.2514/5.9781600866418.0109.0135.

[4] L. Rayleigh, "On the instability of jets," *Proceedings of the London Mathematical Society*, vol. s1-10, no. 1, pp. 4–13, 1878. DOI: https://doi.org/10.1112/plms/s1-10.1.4. eprint: https://londmathsoc.onlinelibrary.wiley.com/doi/pdf/10.1112/plms/s1-10.1.4. [Online]. Available: https://londmathsoc.onlinelibrary.wiley.com/doi/abs/10.1112/plms/s1-10.1.4.

[5] C. Weber, "Zum zerfall eines flüssigkeitsstrahles," *ZAMM - Journal of Applied Mathematics and Mechanics / Zeitschrift für Angewandte Mathematik und Mechanik*, vol. 11, no. 2, pp. 136–154, 1931. DOI: https://doi.org/10.1002/zamm.19310110207. eprint: https://onlinelibrary.wiley.com/doi/pdf/10.1002/zamm.19310110207. [Online]. Available: https://onlinelibrary.wiley.com/doi/abs/10.1002/zamm.19310110207.

[6] R. D. Reitz, R. D. Reitz, and F. V. Bracco, "Mechanism of atomization of a liquid jet," *Physics of Fluids*, 1982. DOI: 10.1063/1.863650.

[7] V. Lević, An, and V. S. Krylov, "Surface-tension-driven phenomena," *Annual Review of Fluid Mechanics*, vol. 1, pp. 293–316, 1969. [Online]. Available: https://api.semanticscholar.org/CorpusID:1824447.

[8] R. Castleman Jr, "The mechanism of atomization accompanying solid injection," Tech. Rep., 1933.

[9] P. J. Santangelo and P. E. Sojka, "A holographic investigation of the near-nozzle structure of an effervescent atomizer-produced spray," *Atomization and Sprays*, 1995. DOI: 10.1615/atomizspr.v5.i2.20.

[10] A. Tarnogrodzki, "Theoretical prediction of the critical weber number," *International Journal of Multiphase Flow*, vol. 19, no. 2, pp. 329–336, 1993, ISSN: 0301-9322. DOI: https://doi.org/10.1016/0301-9322(93)90006-G. [Online]. Available: https://www.sciencedirect.com/science/article/pii/030193229390006G.

[11] W. V. Ohnesorge, "Die bildung von tropfen an düsen und die auflösung flüssiger strahlen," *Zamm-zeitschrift Fur Angewandte Mathematik Und Mechanik*, 1936. DOI: 10.1002/zamm.19360160611.

[12] E. Rostami and H. M. Moghaddam, "The velocity and viscosity impact on the annular spray atomisation of different fuels," *Combustion Theory and Modelling*, vol. 25, no. 1, pp. 158–192, 2021. DOI: 10.1080/13647830.2020.1845399. eprint: https://doi.org/10.1080/13647830.2020.1845399. [Online]. Available: https://doi.org/10.1080/13647830.2020.1845399.

[13] O. Mc Callion and M. Patel, "Viscosity effects on nebulisation of aqueous solutions," *International journal of pharmaceutics*, vol. 130, no. 2, pp. 245–249, 1996.

[14] N. Brosius *et al.*, "Characterization of oscillation modes in levitated droplets using image and non-image based techniques," *npj Microgravity*, 2023. DOI: 10.1038/s41526-023-00254-7.

[15] S. Sovani, P. Sojka, and A. Lefebvre, "Effervescent atomization," *Progress in Energy and Combustion Science*, vol. 27, no. 4, pp. 483–521, 2001. DOI: 10.1016/s0360-1285(00)00029-0.

[16] A. H. Lefebvre, X. F. Wang, and C. A. Martin, "Spray characteristics of aerated-liquid pressure atomizers," *Journal of Propulsion and Power*, 1988. DOI: 10.2514/3.23066.

[17] J. S. Chin and A. H. Lefebvre, "A design procedure for effervescent atomizers," *Engineering for Gas Turbines and Power*, 1993. DOI: 10.1115/93-gt-337.

[18] R. Sikka, K. Vågsæther, D. Bjerketvedt, and J. Lundberg, "Experimental study of primary atomization characteristics of sonic air-assist atomizers," *Applied Sciences*, vol. 11, no. 21, 2021, ISSN: 2076-3417. [Online]. Available: https://www.mdpi.com/2076-3417/11/21/10444.

[19] C. Sun *et al.*, "Measurements of internal flow regime and bubble size in effervescent atomizer," *Experimental Thermal and Fluid Science*, 2018. DOI: 10.1016/j.expthermflusci.2018.07.002.

[20] K. Ramamurthi, K. Ramamurthi, U. Sarkar, U. K. Sarkar, B. N. Raghunandan, and B. N. Raghunandan, "Performance characteristics of effervescent atomizer in different flow regimes," *Atomization and Sprays*, 2009. DOI: 10.1615/atomizspr.v19.i1.30.

[21] C. Sun *et al.*, "Study on effervescent spray morphology based on internal gas-liquid two-phase flow patterns," *European Journal of Mechanics B-fluids*, 2019. DOI: 10.1016/j.euromechflu.2018.10.025.

[22] D. Konstantinov, R. Marsh, P. J. Bowen, and A. P. Crayford, "Effervescent atomisation for industrial energy - technology review," *Atomization and Sprays*, 2010. DOI: 10.1615/atomizspr.v20.i6.

[23] C. A. Catlin and J. Swithenbank, "Physical processes influencing effervescent atomizer performance in the slug and annular flow regimes," *Atomization and Sprays*, 2001. DOI: 10.1615/atomizspr.v11.i5.60.

[24] P. B. Kowalczuk and J. Drzymala, "Physical meaning of the sauter mean diameter of spherical particulate matter," *Particulate Science and Technology*, vol. 34, no. 6, pp. 645–647, 2016.

[25] H. Gadgil, H. Gadgil, H. P. Gadgil, B. N. Raghunandan, and B. N. Raghunandan, "Some features of spray breakup in effervescent atomizers," *Experiments in Fluids*, 2011. DOI: 10.1007/s00348-010-0929-6.

[26] A. H. Lefebvre and S. K. Chen, "Spray cone angles of effervescent atomizers," *Atomization and Sprays*, 1994. DOI: 10.1615/atomizspr.v4.i3.40.

[27] M. Hong, B. A. Fleck, and D. S. Nobes, "Unsteadiness of the internal flow in an effervescent atomizer nozzle," *Experiments in Fluids*, 2014. DOI: 10.1007/s00348-014-1855-9.

[28] M. Liu, Y. Duan, T. Zhang, and Y. Xu, "Evaluation of unsteadiness in effervescent sprays by analysis of droplet arrival statistics – the influence of fluids properties and atomizer internal design," *Experimental Thermal and Fluid Science*, 2011. DOI: 10.1016/j.expthermflusci.2010.09.001.

[29] M. Jicha and J. Jedelsky, "Unsteadiness in effervescent sprays: A new evaluation method and the influence of operational conditions," *Atomization and Sprays*, 2008. DOI: 10.1615/atomizspr.v18.i1.20.

[30] J. Middleton, "Gas-liquid dispersion and mixing," *Mixing in the process industries*, vol. 2, pp. 349–352, 1992.

[31] L. Albright, *Albright's chemical engineering handbook*. CRC Press, 2008.

[32] J. C. Middleton and J. M. Smith, "Gas–liquid mixing in turbulent systems," *Handbook of Industrial Mixing: Science and Practice*, pp. 585–638, 2003.

[33] M. Rahman, "Scaling of effervescent atomization and industrial two-phase flow," 2011.

[34] E. Dickinson, "Emulsions," *Annual Reports Section" C"(Physical Chemistry)*, vol. 83, pp. 31–58, 1986.

[35] D. Elliott and E. Weinberg, "Acceleration of liquids in two phase nozzles," Tech. Rep., 1968.

[36] T. D. Fansler and S. E. Parrish, "Spray measurement technology: A review," *Measurement Science and Technology*, vol. 26, no. 1, p. 012 002, 2014.

[37] J. Desantes, R. Payri, J. Pastor, and J. Gimeno, "Experimental characterization of internal nozzle flow and diesel spray behavior. part i: Nonevaporative conditions," *Atomization and Sprays - ATOMIZATION SPRAYS*, vol. 15, pp. 489–516, Sep. 2005. DOI: 10.1615/AtomizSpr.v15.i5.20.

[38] D. Duke, A. Kastengren, F. Tilocco, and C. Powell, "Synchrotron x-ray measurements of cavitation," May 2013.

[39] M. Linne, "Imaging in the optically dense regions of a spray: A review of developing techniques," *Progress in Energy and Combustion Science*, vol. 39, no. 5, pp. 403–440, 2013.

[40] V. Bodoc, C. Laurent, Y. Biscos, and G. Lavergne, "Advanced measurement techniques for spray investigations," *Aerospace Lab*, no. 1, p–1, 2009.

[41] A. Braeuer, "Shadowgraph and schlieren techniques," in *Supercritical Fluid Science and Technology*, vol. 7, Elsevier, 2015, pp. 283–312.

[42] C. Willert and J. Kompenhans, *Piv analysis of ludwig prandtl's historic flow visualization films*, 2010. arXiv: 1010.3149 [physics.flu-dyn].

[43] J. Westerweel, G. E. Elsinga, and R. J. Adrian, "Particle image velocimetry for complex and turbulent flows," *Annual Review of Fluid Mechanics*, vol. 45, no. 1, pp. 409–436, 2013. DOI: 10.1146/annurev-fluid-120710-101204. eprint: https://doi.org/10.1146/annurev-fluid-120710-101204. [Online]. Available: https://doi.org/10.1146/annurev-fluid-120710-101204.

[44] M. Raffel, C. E. Willert, F. Scarano, C. J. Kähler, S. T. Wereley, and J. Kompenhans, *Particle image velocimetry: a practical guide*. Springer, 2018.

[45] W. D. Bachalo, "Spray diagnostics for the twenty-first century," *Atomization and Sprays*, vol. 10, no. 3-5, 2000.

[46] B. Ofner, "Phase doppler anemometry (pda)," in *Optical Measurements: Techniques and Applications*, Springer, 2001, pp. 139–152.

[47] C. Tropea, "The development of the phase doppler technique," in *Applied optical measurements*, Springer, 1999, pp. 279–292.

[48] M. Versluis, "High-speed imaging in fluids," *Experiments in fluids*, vol. 54, pp. 1–35, 2013.

[49] A. Bellofiore, R. Ragucci, P. Di Martino, and A. Cavaliere, "Taylored binarization of spray shadowgrams for morphology investigation," in *2007 Annual Meeting of the Italian Section of the Combustion Institute*, 2007, pp. 20–22.

[50] N. La Forgia, E. H. Herø, and H. A. Jakobsen, "High-speed image processing of fluid particle breakage in turbulent flow," *Chemical Engineering Science: X*, vol. 12, p. 100 117, 2021.

[51] J. Blaisot and J. Yon, "Droplet size and morphology characterization for dense sprays by image processing: Application to the diesel spray," *Experiments in fluids*, vol. 39, no. 6, pp. 977–994, 2005.

[52] Y. Zhou, W. Qi, Z. Wei, and Y. Zhang, "An image segmentation algorithm for fuel spray schlieren images with noisy backgrounds under engine-like conditions," *Experiments in Fluids*, vol. 63, no. 5, p. 89, 2022.

[53] G. Berkooz, P. Holmes, and J. L. Lumley, "The proper orthogonal decomposition in the analysis of turbulent flows," *Annual review of fluid mechanics*, vol. 25, no. 1, pp. 539–575, 1993.

[54] G. F. Franklin, J. D. Powell, A. Emami-Naeini, and J. D. Powell, *Feedback control of dynamic systems*. Prentice hall Upper Saddle River, 2002, vol. 4.

[55] R. Osuna-Orozco, N. Machicoane, P. D. Huck, and A. Aliseda, "Feedback control of coaxial atomization based on the spray liquid distribution," *Atomization and Sprays*, vol. 29, no. 6, 2019.

[56] J. K. Bothell, T. B. Morgan, and T. J. Heindel, "Image-based feedback control for a coaxial spray," *Journal of Fluids Engineering*, vol. 142, no. 11, p. 114 501, 2020.

[57] H. Kim and M.-C. Lai, "Effect of pressure pulsation on performance of airblast atomizer and micro-machined fuel injectors," in *38th AIAA/ASME/SAE/ASEE Joint Propulsion Conference & Exhibit*, 2002, p. 4227.

[58] H. Chang, D. Nelson, C. Sipperley, and C. Edwards, "Development of a temporally modulated fuel injector with controlled spray dynamics," eng, *Journal of engineering for gas turbines and power*, vol. 125, no. 1, pp. 284–291, 2003, ISSN: 0742-4795.

[59] M. Mlkvik, P. Stähle, H. P. Schuchmann, V. Gaukel, J. Jedelsky, and M. Jicha, "Twin-fluid atomization of viscous liquids: The effect of atomizer construction on breakup process, spray stability and droplet size," *International Journal of Multiphase Flow*, 2015. DOI: 10.1016/j.ijmultiphaseflow.2015.06.010.

[60] M. Zaremba *et al.*, "An experimental analysis of the spraying processes in improved design of effervescent atomizer," *International Journal of Multiphase Flow*, 2018. DOI: 10.1016/j.ijmultiphaseflow.2018.01.012.

[61] A. Kourmatzis, A. Lowe, and A. R. Masri, "Combined effervescent and airblast atomization of a liquid jet," *Experimental Thermal and Fluid Science*, 2016. DOI: 10.1016/j.expthermflusci.2016.02.002.

[62] H. Zhao *et al.*, "Breakup morphology of annular liquid sheet with an inner round air stream," *Chemical Engineering Science*, 2015. DOI: 10.1016/j.ces.2015.06.062.

[63] S. W. Stein and C. G. Thiel, "The history of therapeutic aerosols: A chronological review," *Journal of Aerosol Medicine and Pulmonary Drug Delivery*, vol. 30, no. 1, pp. 20–41, 2017. DOI: 10.1089/jamp.2016.1297.

[64] B. Barker, J. B. Bell, and A. L. Garcia, "Fluctuating hydrodynamics and the rayleigh–plateau instability," *Proceedings of the National Academy of Sciences of the United States of America*, 2023. DOI: 10.1073/pnas.2306088120.

[65] C. E. do Amaral *et al.*, "Image processing techniques for high-speed videometry in horizontal two-phase slug flows," *Flow Measurement and Instrumentation*, vol. 33, pp. 257–264, 2013.

Appendix A

Rayleigh Instability Derivation

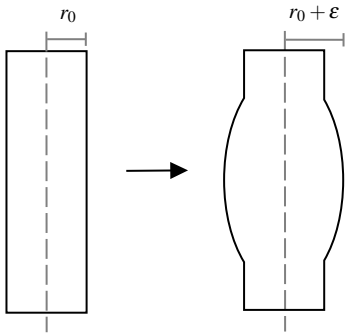

Figure A.1: Stable vs perturbed state for a liquid jet

As shown by the figure above, let the radius of some unperturbed jet be defined as r_0. Then, the radius at any point of the jet can be described in terms of the time, as well as the distance from the exit, shown by [4].

Approximating the perturbation sinusoidally, and assuming that $\varepsilon << r_0$, gives the following expression for radius:

$$\tilde{R}(z,t) = r_0 + \varepsilon(\exp^{\omega t + ikz}) \tag{A.0.0.1}$$

To simplify typography, let the oscillating component of the function above be denoted as follows:

$$\xi = (\exp^{\omega t + ikz}) \tag{A.0.0.2}$$

Here, k is the wave-number of the disturbance (the number of wavelengths per unit length), and ω is the angular frequency (a measure of the growth rate of the disturbance). Assume now also that the velocity and pressure fluctuations have a similar form to this, i.e.:

$$\begin{aligned} u_R &= R(r)\xi \\ u_Z &= Z(r)\xi \\ \tilde{p} &= P(r)\xi \end{aligned} \tag{A.0.0.3}$$

Here, u_R is the radial velocity, u_Z is the stream-wise velocity, and P is pressure. Assuming axisymmetry, and linearity due to the small magnitude of ε, a cylindrical version of the Navier-Stokes Equations can be formulated as follows:

$$\begin{aligned} \frac{\partial u_R}{\partial t} &= -\frac{1}{\rho}\frac{\partial \tilde{p}}{\partial r} \\ \frac{\partial u_Z}{\partial t} &= -\frac{1}{\rho}\frac{\partial \tilde{p}}{\partial z} \\ \frac{\partial u_R}{\partial r} + \frac{u_R}{r} + u_Z &= 0 \end{aligned} \tag{A.0.0.4}$$

Now, substituting the expressions given in Eq A.0.0.3 into the above differentials gives the following relations:

$$\begin{aligned} \omega R &= -\frac{1}{\rho}\frac{\partial P}{\partial r} \\ \omega Z &= -\frac{ik}{\rho}P \end{aligned} \tag{A.0.0.5}$$

These can be combined with the continuity relation to form a single partial differential equation for R, the jet radius, shown here [4]:

$$r^2\frac{\partial^2 R}{\partial r^2} + r\frac{\partial R}{\partial r} - (1+(kR)^2)R = 0 \tag{A.0.0.6}$$

This differential is a Bessel function of order 1 ($\alpha = 1$) [64]. Bessel functions are a family of functions that describe decaying vibrations in cylindrical or spherical coordinates. Canonically used to find separable solutions to the Laplace equation, they are solutions to equations of the following form:

$$x^2\frac{d^2y}{dx^2} + x\frac{dy}{dx} + \left(x^2-\alpha^2\right)y = 0 \tag{A.0.0.7}$$

The solutions are combinations of 2 linearly independent functions (I_α & K_α), with constants determined by the boundary conditions, as shown here:

$$R(r) = CI_1(kr) + C_2K_1(kr) \tag{A.0.0.8}$$

However, as the velocity profile should be smooth throughout the jet, specifically $R(0) = 0$, the second function cannot appear in the combination. To find the constant C, first consider the kinematic relation: i.e that the rate of change of the cylinder radius ($\frac{d\tilde{R}}{dt}$) must equal the radial velocity (u_R) at the jet surface:

$$\begin{aligned} \frac{d\tilde{R}}{dt} = u_R \implies \varepsilon\omega\xi = R(R_0)\xi = CI_1(kR_0)\xi \\ \implies C = \frac{\varepsilon\omega}{I_1(kR_0)} \end{aligned} \tag{A.0.0.9}$$

The next relation is built from the Young-Laplace equation. This equation describes the effect of surface tension on a curved surface, as shown here:

$$\Delta p = -\gamma\left(\frac{1}{R_1}+\frac{1}{R_2}\right) \tag{A.0.0.10}$$

Here, γ is the coefficient of surface tension, and R_1 and R_2 are the principal radii of curvature of the surface. Thus, assuming some equilibrium pressure (p_0) within the jet without perturbation, the pressures at the surface of the jet can thus be equated as:

$$p_0+\tilde{p} = \left(\frac{1}{R_1}+\frac{1}{R_2}\right) \tag{A.0.0.11}$$

Here, let the radial curvature (R_1) be the perturbed radius, i.e:

$$R_1 = R_0+\varepsilon\xi \tag{A.0.0.12}$$

Then, using the initial assumption that $\varepsilon << R_0$, this can further be simplified as:

$$\frac{1}{R_1} \approx \frac{1}{R_0}\left(1-\frac{\varepsilon}{R_0}\xi\right) \tag{A.0.0.13}$$

To find the tangential curvature (R_2), use the second derivative definition of curvature for space curves [64], i.e:

$$\frac{1}{R_2} = \frac{|\tilde{R}''(z)|}{(1+\tilde{R}'(z)^2)^{3/2}} \tag{A.0.0.14}$$

Using again the assumption that the perturbation is very small compared to the initial diameter (i.e. both $R''(z)$ and $R'(z)$ go to zero), this can further be simplified to:

$$\frac{1}{R_2} \approx \frac{\partial^2\tilde{R}}{\partial z^2} = \varepsilon k^2\xi \tag{A.0.0.15}$$

Finally, the equilibrium pressure can also be calculated for the special case of no perturbation. Here, the principle radii simplify, as $R_1 = R_0$ and $R_2 = \infty$. Thus:

$$p_0 = \frac{\gamma}{R_0} \tag{A.0.0.16}$$

Combining all of the expressions above back into the Young-Laplace equation gives the following:

$$\begin{aligned}\frac{\gamma}{R_0}+\tilde{p} &= \gamma\left(\frac{1}{R_0}-\frac{\varepsilon}{R_0^2}\xi+\varepsilon k^2\xi\right)\\ \implies \tilde{p} &= \frac{\gamma\varepsilon}{R_0^2}(k^2R_0^2-1)\xi\end{aligned} \tag{A.0.0.17}$$

Another method of calculating this perturbed pressure is using the relations given in Eq A.0.0.5. A recurrance relation of the Bessel function, i.e $I_1(kx) = \frac{1}{k}I_0'(kx)$ is also useful. In particular:

$$
\begin{aligned}
P(r) &= -\rho\omega \int_0^r R(x)dx \\
&= -\frac{\rho\varepsilon\omega^2}{I_1(kR_0)} \int_0^r I_1(x)dx \\
&= -\frac{\rho\varepsilon\omega^2}{kI_1(kR_0)} I_0(kr) \\
\implies \tilde{p} &= -\frac{\rho\varepsilon\omega^2}{kI_1(kR_0)} I_0(kr)\xi
\end{aligned}
\tag{A.0.0.18}
$$